Statistical Analysis of Wind- and Rain-generated Ocean Ambient Noise in the Northeast Pacific Continental Margin

Felix Schwock

A thesis
submitted in partial fulfillment of the
requirements for the degree of

Master of Science

University of Washington

2021

Committee:

Shima Abadi

Les Atlas

Program Authorized to Offer Degree:
Electrical Engineering

University of Washington

Abstract

Statistical Analysis of Wind- and Rain-generated Ocean Ambient Noise in the Northeast Pacific Continental Margin

Felix Schwock

Chair of the Supervisory Committee:
Dr. Shima Abadi
Electrical and Computer Engineering

Large scale studies of underwater ambient noise during wind and rain are important for assessing the ocean environment and enabling remote sensing of wind speeds and rain rates over the open ocean. In this work, approximately 3.5 years of acoustical and meteorological data recorded at the northeast Pacific continental margin are evaluated. The acoustic data are recorded at a sampling rate of 64 kHz and depths of 81 m and 581 m at the continental shelf and slope, respectively. Rain rates and wind speeds are provided by surface buoys located in the vicinity of each hydrophone. Acoustic and meteorological data are used to compute power spectral density (PSD) estimates for various wind speeds and rain rates. Since the acoustic data are compromised by outliers, a robust spectral estimator that uses sample percentiles is introduced and its statistical properties are derived. The resulting PSD estimates are used to analyze and model the frequency, wind speed, and rain rate dependency of ambient noise spectral levels in greater detail. Furthermore, the results are compared with findings from previous studies.

TABLE OF CONTENTS

LIST OF FIGURES

LIST OF TABLES

GLOSSARY

ADCP: Acoustic Doppler Current Profiler

CTD: Conductivity, Temperature, and Depth

OOI: Ocean Observatories Initiative

PDF: Probability Density Function

PSD: Power Spectral Density

VLA: Vertical Line Array

WOSA: Welch's Overlapped Segment Averaging

WP: Welch Percentile

a, b: Intercepts of linear models

f: Acoustic frequency (Hz)

n: Slope factor of linear model

R^2: Coefficient of determination

r: Rain rate (mm/h)

s: Slope of linear model

SPL: Sound spectral level (dB re $1\frac{\mu\text{Pa}^2}{\text{Hz}}$)

v: Wind speed (m/s)

ACKNOWLEDGMENTS

First and foremost I would like to thank my advisor, Professor Shima Abadi for welcoming me in her lab and being a great advisor throughout my master's studies. Without Professor Abadi's valuable feedback and commitment for high quality mentoring this thesis would not have been possible. I am incredible grateful that she showed so much support for my goals and was always open to new projects and research ideas. I also want to acknowledge my other exam committee member, Professor Les Atlas, not only for serving on this committee, but also for being very welcoming when I started my graduate studies at the University of Washington. Furthermore, it was a pleasure to be around so many other great students and team mates, most notably Cuinn, Ellory, Jordan, Eldridge, Matthew, and John, who always sparked my curiosity for other research fields.

None of this would have been possible without the financial support of the sponsors I had during my master's studies. Most importantly, I want to thank the Fulbright program, not only for financially enabling my dream of studying abroad, but also for proving so many opportunities of meeting remarkable people from all round the world. A special thanks also goes to the Office of Naval Research for funding my projects.

Finally, I want to thank all the people in my life who have supported me during my time in Seattle and before. Most notably my parents and my brother who supported me in so many ways and always had an open ear when I needed someone to talk to. I also want to express my greatest gratitude to my friend Chia-Lin, who is the main reason I made it through a time shook by a global pandemic. 你是最棒的。 Moreover, I want to thank all the friends who showed me that there is a life outside the university and who have accompanied me on my countless hikes and adventures in the US.

Chapter 1

INTRODUCTION

Ocean ambient noise reveals important information about marine life, natural phenomena, and the human footprint in the ocean. Sources of ocean ambient noise can be of natural origin such as bubbles, surface waves, turbulences, precipitation, seismic activity, biological activity and, sea-ice movements, or man-made such as explosions, industrial activity, and oceanic traffic [72]. The statistical characterization of the ocean ambient soundscape started after World War II with a paper published by Knudsen et al. [29] laying the baseline for future ocean ambient noise analyses. Another highly influential early paper was published in 1962 by Wenz [72] describing the general spectrum characteristics of the ocean soundscape for a variety of sources. Since then, many studies have analyzed ocean ambient noise from anthropocentric and natural sources at various locations all over the globe. However, as the ocean environment is subject to strong temporal and spatial variations, more field measurements over long time scales and yet poorly characterized locations are still needed. Furthermore, the vast amount of acoustic data that will likely be collected in the next years calls for new processing techniques that are not only computationally efficient, but also robust against interfering signals. The motivation behind this thesis is to contribute to the analysis of ocean ambient noise by providing new insights of the behavior of wind and rain generated noise as well as describing an efficient and robust processing technique for computing ocean noise spectra.

Wind and rain are among the natural sources of underwater sound and, in the absence of other noise sources such as shipping or marine mammal vocalizations, are the dominant contributor of ambient noise in the ocean for frequencies above 100 Hz [72]. Therefore, characterizing wind and rain noise is crucial for gaining a better understanding of the acoustical

environment in the ocean. Furthermore, other acoustic signals have to be discriminated from the general ocean ambient noise due to wind and rain, which requires profound knowledge of its spectral characteristic. Wind and rain noise measurements also lay the foundation for acoustic remote sensing of wind speeds and rain rates over the open ocean. Those acoustic based measurement techniques can outperform satellite measurements in terms of spatial and temporal resolution and also have advantages over buoy or ship-born systems. Successful estimations of wind and rain parameters using ambient noise measurements can be found for example in [62, 66, 67, 56, 12, 33] and are crucial for an accurate modeling of air-sea fluxes and the ocean gas exchange, thus, providing important knowledge in understanding the global climate system [70].

The goal of this thesis is to add to the characterization of wind and rain generated ocean noise by evaluating acoustic and meteorological data at the northeast Pacific continental margin between 2015 and 2019 provided by the Ocean Observatories Initiative (OOI). Compared to many studies conducted in the past, this data set allows for a more detailed analysis of the spectral and temporal characteristics of wind and rain noise. The size of the data set also requires computationally efficient and robust signal processing algorithms, which will be described as well.

The remainder of the thesis is outlined as follows: Chapter 2 reviews and summarizes results from previous studies about wind and rain noise and highlights main characteristics of their spectral behavior. In Chapter 3 and 4 the measurement setup and processing framework for collecting and analyzing the acoustic data are described. In Chapter 5 and 6 the results of the wind and rain noise analysis are presented and comparisons with findings from past studies are made. Finally, Chapter 7 summarizes this research effort and states the conclusions drawn from it.

Chapter 2

PRIOR WORK ON AMBIENT NOISE DUE TO WIND AND RAIN

2.1 Wind

Wind generated underwater noise in the frequency range between 0.1 - 30 kHz is the result of a multitude of mechanisms [27]. The main contributors are noise from breaking waves and whitecaps, flow noise, cavitation noise, and noise from wave generating actions [64]. However, different sound mechanisms dominate different frequency bands [65] and, as a result, the spectral behavior of wind noise varies over frequencies. Especially for frequencies below 1 kHz a variety of spectral trajectories were found in numerous experiments and field measurements. For example, Knudsen at al. reported that the spectral level of wind noise decreases with a rate of approximately -17 dB/decade (dB/dec) over frequency [29]. On the other hand, the authors in [72] and [53] have found a broad spectral peak between 0.1 - 1 kHz. To improve the interpretability of wind noise measurements, many subsequent studies have used hydrophone vertical line array (VLA) measurements to discriminate between the noise component from local winds and distant sound sources. Using this method, the authors in [13] found a similar decrease in spectral level to the Kundsen curves of about -20 dB/dec for wind speeds above 5 m/s. On the other hand, the authors of [11] have found that while the omnidirectional noise shows an overall decrease in spectral level with increasing frequency, local wind noise spectral levels are essentially flat for frequencies between 100 - 800 Hz. Those results are consistent with VLA measurements in [28] where wind noise measurements from the southern and northern hemisphere for wind speeds above 10 m/s were combined. For wind speeds below 5 m/s however, the study reported a significant decrease in spectral level for frequencies between 40 - 1000 Hz.

Above 1 kHz, the sound spectral level decreases linearly over the logarithm of the frequency and, thus, can be described by the relation

$$SPL(f) = s \log_{10}(f) + a, \tag{2.1}$$

where SPL is the sound spectral level, and s and a are slope and intercept, respectively. The slope s obtained from various measurements is shown in Table 2.1. Most studies reported an average slope between -17 dB/oct and -20 dB/oct. Only the values obtained in [34] and [10] (Atlantic) are significantly outside this range. The variations between studies are likely the result of a multitude of factors such as measurement location and depth, measurement time and duration, methodology for obtaining wind speed estimates, and processing techniques for computing noise spectral levels. However, to draw better conclusions about the influence of each of those factors more measurements are necessary.

Another relation that has been studied extensively in the past is the effect of the wind speed on the noise level. Many studies have shown that this relation is best modeled using a two regime model [20, 16, 13, 28]. For wind speeds lower than approximately 5 m/s the spectral level is either constant or only slowly increasing with increasing wind speed. For wind speeds above 5 m/s a linear relation between spectral level and the logarithm of the wind speed can be observed. This relation is typically expressed as

$$SPL(v) = 20\, n\, \log_{10}(v) + b, \tag{2.2}$$

where v is the wind speed in m/s and n and b are the slope factor and intercept, respectively. A value of $n = 1$ indicates that the spectral level increases with a rate of 20 dB/dec. The widely accepted explanation for the occurrence of two wind speed regimes is that breaking waves and whitecaps are not emerging for low wind speeds and, thus, the influence of wind generated noise on the underwater soundscape is only marginal in this case [40, 41].

Several values for the slope factor n from previous studies are shown in Table 2.2. For frequencies between 0.1 - 1 kHz, n ranges between 0.5 - 1.7, whereby the variations are of-

ten large within a study. In general, the value of n highly depends on frequency, location, and measurement depth. This is very well demonstrated in [20], where data from two hydrophones deployed in the North Pacific during the SPICEX experiment are evaluated. The hydrophones where deployed at depth of 375 m and 4218 m, respectively, and values for n are reported for frequencies between 50 - 450 Hz. While n for the shallower hydrophone monotonically increases from approximately 0.5 at 100 Hz to 1.15 at 300 - 450 Hz, the deeper hydrophone shows first an increase in n from 1.2 at 100 Hz to 1.5 at 150 Hz, before n decreases again to a value of 1.2 at 450 Hz. Similar strong frequency dependencies, however often with a different trajectory, can also be found in other studies for frequencies below 1 kHz. In general, no clear relation between the values of n and the measurement location, depth, or considered frequency was found.

For frequencies above 1 kHz, the variability is significantly smaller with values of n ranging between 0.9 - 1.54 and usually staying in a range of 1 - 1.2. However, it is noted that many studies only considered a single wind speed regime, which could possibly result in an underestimation of n.

A different behavior can be observed for very high wind speeds, approximately above 14 - 15 m/s, where the spectral level can actually decrease with increasing wind speed at high frequencies [19, 8]. While this behavior can be observed for frequencies around 8 kHz, it is more distinct for frequencies well above 10 kHz. The high wind speed and the corresponding strong surface agitation can create a layer of bubbles below the water surface, which predominantly attenuates high frequency surface sounds. It is noted that many studies considered in Table 2.2 only used frequencies up to a few kilohertz, so that this phenomenon does not have a significant effect on their estimated slope.

2.2 Rain

Early studies in water tanks [21, 43] have identified two important sound generating mechanisms when droplets strike the water surface: (1) the impact of the droplet on the surface generating a broadband white noise spectrum, where the spectral level is highly dependent

Table 2.1: Slope s of linear model $SPL(f) = s\log_{10}(f)+a$ from various studies for frequencies above 1 kHz. Most studies reported an average slope between -17 dB/oct and -20 dB/oct.

reference	s (dB/dec)	frequency range (kHz)	location
[66]	-19	3 - 20	tropical Atlantic
[10] – Pacific	-18.9	4.3 - 14.5	equatorial Pacific
[10] – Atlantic	-21.9	4.3 - 14.5	north Atlantic
[32]	-17 ± 2	4.3 - 14.5	Queen Charlotte Sound
[34]	-15.7	1 - 50	tropical Pacific
[72]	-20	1 - 20	various
[29]	-16.7 ± 3.3	0.1 - 25	various
[67]	-18.8 ± 1.3	3 - 25	off DelMarVa Peninsula
[18]	-17 ± 2	4.3 - 14.5	equatorial Pacific

on drop radius and impact velocity, and (2) an oscillating air bubble emerging during the drop impact and radiating acoustic energy between 1 - 20 kHz. The sound from the oscillating air bubble is particularly significant during light rain and drizzle, where a broad spectral peak around 15 kHz can be observed. Several measurements conducted in lakes have shown that the underwater noise spectrum generated by actual rain is in good agreement with these laboratory studies and especially the broadband peak around 15 kHz was confirmed [9, 43, 60, 31].

The dependence of impact and bubble sound on the drop diameter D was further analyzed in a series of papers and can be summarized as follows: (1) Small raindrops ($0.8\,\text{mm} \leq D < 1.1\,\text{mm}$) produce a broadband impact sound followed by a much louder sound resulting from the damped oscillation of microbubbles, called *type I* microbubbles, at frequencies centered around 15 kHz [38]. The emergence of *type I* microbubbles, however, is highly wind dependent [37] and quickly decreases if the incident angle of the rain drop deviates from

Table 2.2: Slope factor n of linear model $SPL(v) = 20\,n \log_{10}(v) + b$ from various studies. For frequencies between 0.1 - 1 kHz, n ranges between 0.5 - 1.7, whereas for frequencies above 1 kHz, n only ranges from 0.9 - 1.54 and usually stays between 1 - 1.2.

reference	n	wind speed range (m/s)	location
frequencies between 0.1 - 1 kHz			
[15]	0.81 - 1.39	5 - 25	near Bermuda
[11]	0.46 - 0.72	1 - 15	east off Australia
[20]	0.5 - 1.5	5 - 12	northeast Pacific
[53]	1.29 - 1.7	1.5 - 18	Scotian shelf
[13]	1.09 - 1.49	6 - 15	northeast Pacific
[63]	1.01 - 1.57	9 - 14	Parece-Vela basin
frequencies $>$ 1 kHz			
[66]	1.38	4 - 15	tropical Atlantic
[10] – Pacific	1.1 - 1.54	0 - 10	equatorial Pacific
[10] – Atlantic	0.9 - 0.95	0 - 20	north Atlantic
[32]	1.08 - 1.52	0 - 12	Queen Charlotte Sound
[15]	0.93 - 1.03	5 - 25	near Bermuda
[62]	0.99	4 - 20	tropical Atlantic
[53]	1.2 - 1.24	1.5 - 18	Scotian shelf
[18]	1.15 - 1.2	5.5 - 10	equatorial Pacific

normal. (2) Medium size raindrops (1.1 mm $\leq D <$ 2.2 mm) are particularly quiet and do not create bubbles, thus, only contributing a little to the underwater soundscape [46]. (3) Large raindrops ($D >$ 2.2 mm) produce a loud impact sound [55, 38]. Furthermore, two types of bubbles, which radiate similar acoustic sound energy, can be observed. The first type (*type II* microbubbles) is a direct result of the drop impact and largely contributes to the sound spectrum below 10 kHz [38]. The second type (*type III* microbubbles) is caused by drop aerosols generated during the initial impact and oscillates with frequencies typically between 3 - 25 kHz [48].

These studies were complemented by open ocean measurements during light rain [61] and heavy rain [47]. The latter showed that heavy rain results in an increase of the noise level over a frequency range of 4 - 21 kHz and no spectral peak at 15 kHz can be observed. For very heavy rain with rain rates of 150 mm/h or higher a decrease of the spectral level above 10 kHz was observed [47]. This phenomenon is similar to the behavior during very high wind speeds and, thus, can also be explained by a layer of bubbles forming below the water surface and attenuating sound in the high frequency range.

A very detailed analysis of the spectral shape of rain noise for different rain rates and wind speeds evaluating about 90 buoy months of data from several hydrophones located at the Western Pacific Warm Pool and the Inter-tropical Convergence Zone was conducted by the authors in [34]. The amount of acoustic data collected in this study allows for the computation of average rainfall spectra for several discrete rain rate bins. The average spectra show a linear trajectory over a logarithmic frequency range for frequencies between 1 - 10 kHz. The slopes of the linear regression depend on the rainfall rate and follow the relation

$$s_{\text{rain}} = 8.33 \log_{10}(r) - 14.3, \tag{2.3}$$

where r is the rainfall rate in mm/h. That is, for rain rates below 30 mm/h, the spectral level decreases with increasing frequency, whereas an increase in spectral level for rain rates above 70 mm/h can be observed. The spectral level in this frequency range also increases

with increasing rain rate. For example at 5 kHz the spectral level ranges from about 50 dB[1] at 2 - 5 mm/h to 75 dB at 100 - 200 mm/h rain rate. Above 10 kHz rain noise spectral levels decrease with increasing frequency, except for rain rates below 10 mm/h, where a peak around 15 kHz can be observed. Another important finding of this study is that the sound spectral levels between 3 - 10 kHz for different rain rates are almost independent of the wind speed.

While in all of the field studies discussed above, the hydrophones were deployed close to the surface (maximum depth of about 100 m), the authors in [3] and [6] showed that the typical rain noise pattern can also be detected at greater depths.

[1]Spectral levels in dB are relative to $1\,\frac{\mu\mathrm{Pa}^2}{\mathrm{Hz}}$.

Chapter 3

INSTRUMENTATION AND DATA PROCESSING

In this chapter the measurement setup, acoustic environment, and algorithms for processing acoustic and meteorological data are presented. First, the measurement location and instruments for the data acquisition are described. Afterwards, the acoustic environment is sketched by illustrating typical sound speed profiles for different seasons. The effect of the sound speed profile on the effective surface listening area is discussed. In the last two parts of the chapter algorithms for processing the acoustic data and detecting rain events using the meteorological data are described.

3.1 Measurement Setup

The acoustic and meteorological data utilized in this paper are recorded between December 2015 and June 2019 by the Coastal Endurance Array which is maintained by the Ocean Observatories Initiative (OOI). The instruments are located at two sites as shown in Figure 3.1a. The first site is located at the continental slope at 44°22′8.4″ N and 124°57′14.4″ W. The instruments in this site are part of the Oregon Offshore Cabled Benthic Experiment Package[1] and Oregon Offshore Surface Mooring[2] of the OOI Coastal Endurance Array. The hydrophone is deployed on the sea floor at a depth of 581 m. This hydrophone is referred to as the *deep hydrophone* throughout this thesis. The second site is located at the continental shelf at 44°38′13.2″ N and 124°18′21.6″ W. The instruments in this site are part of the

[1]NFS Ocean Observatories Initiative Data Portal, `https://ooinet.oceanobservatories.org` Broadband Acoustic Receiver (CE04OSBP-LJ01C-11-HYDBBA105) data from 01 December 2015 to 30 June 2019. Downloaded on 06 June 2020

[2]NFS Ocean Observatories Initiative Data Portal, `https://ooinet.oceanobservatories.org` Bulk Meteorology Instrument Package (CE04OSSM-SBD11-06-METBKA000) data from 01 December 2015 to 30 June 2019. Downloaded on 06 June 2020

Oregon Shelf Cabled Benthic Experiment Package[3] and Oregon Shelf Surface Mooring[4] of the OOI Coastal Endurance Array. The hydrophone is deployed on the sea floor at a depth of 81 m. This hydrophone is referred to as the *shallow hydrophone* throughout this thesis. The deep and shallow site are 59 km apart from each other. At each site, there is a surface buoy deployed close to the hydrophone measuring rain accumulation and wind speed. The position of the surface buoys relative to the hydrophones are shown in Figure 3.1b.

3.1.1 Acoustic Data Collection

Acoustic data are recorded by broadband icListen HF hydrophones manufactured by Ocean Sonics with sensitivity $-169\,\mathrm{dB\,V}$ re $1\,\mu\mathrm{Pa}$. The raw acoustic data is accessible on the data server of the OOI. Calibration data is available by Ocean Sonics for the icListen HF instruments at a depth of 1 m, and frequency ranges of 0 - 200 kHz observed during the experiment in a water tank. The frequency range of the hydrophones is roughly 10 Hz - 200 kHz. The hydrophones record continuously at a sampling rate of 64 kHz and transmit the acoustic data to the shore via a fiber optic cable.

3.1.2 Meteorological Data Collection

Meteorological measurements are provided by surface buoys located in the vicinity of each hydrophone. The cumulative rain and wind speed samples are acquired every 30 - 65 s (on average every 60 s), transmitted to the shore via a satellite link, and accessible on the data server of the OOI.

The rain accumulations are measured by an *RM Young 50202* self-siphoning capacitance rain gauge with a cylindrical catchment area of $100\,\mathrm{cm}^2$ and a volume of 500 mL. Thus, the

[3]NFS Ocean Observatories Initiative Data Portal, `https://ooinet.oceanobservatories.org` Broadband Acoustic Receiver (CE02SHBP-LJ01D-11-HYDBBA106) data from 01 December 2015 to 30 June 2019. Downloaded on 06 June 2020

[4]NFS Ocean Observatories Initiative Data Portal, `https://ooinet.oceanobservatories.org` Bulk Meteorology Instrument Package (CE02SHSM-SBD11-06-METBKA000) data from 01 December 2015 to 30 June 2019. Downloaded on 07 June 2020

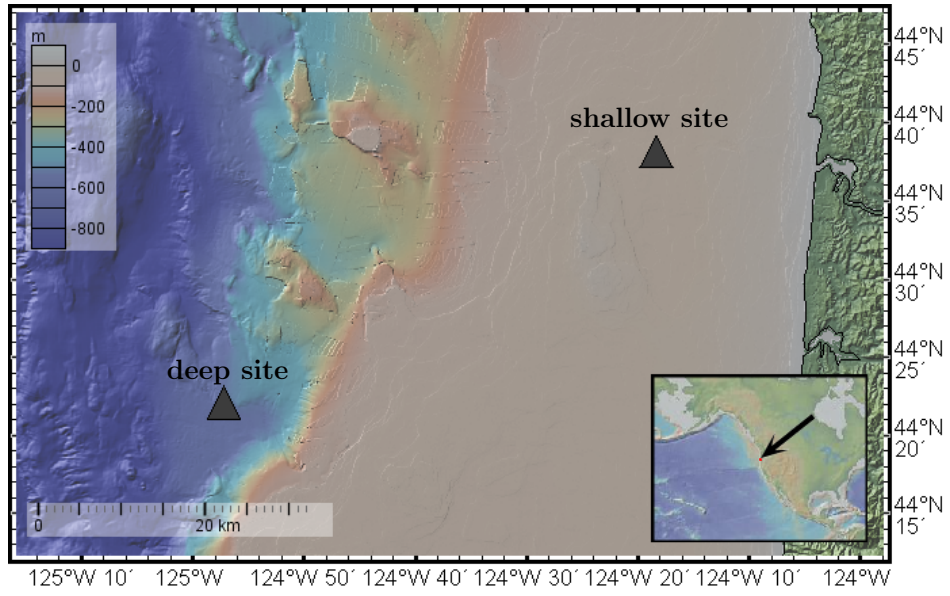

(a)

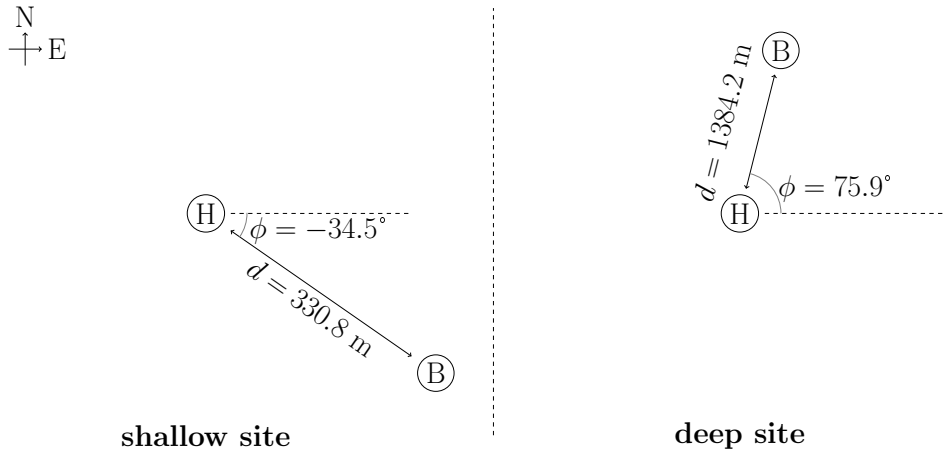

(b)

Figure 3.1: (a) Locations of the deep and shallow site in the northeast Pacific ocean (figure made with GeoMapApp (www.geomapapp.org) / CC BY / CC BY [57]) and (b) displacement of the hydrophone (H) and surface buoy (B) at both locations.

cumulative amount of rain is measured in a range of 0 - 50 mm with a nominal precision of 1 mm. When the catchment basin of the rain gauge is full, water is automatically released via a drain. These siphoning events usually last for about 30 s [44]. To compute the rain rates, the difference in rain amount between two consecutive samples is divided by the time difference between those samples. Due to the relative small catchment area of the rain gauge, one-minute rain rate measurements are prone to errors from isolated drips typically occurring during light rain [49, 45]. These drips can cause peaks in the rain rate, and thus, overestimating its actual value. The authors in [49] estimates that the mean relative error of one-minute rain rate samples of *RM Young* capacitance rain gauges is about ±38 - 40 % for rain rates below 5 mm/h and ±12 - 14 % for rain rates above 5 mm/h. Furthermore, the measurement precision decreases at high wind speeds (in [45], a wind speed of 4.1 m/s) due to heavier movement of the water in the catchment basin.

The wind speeds are measured by a *Gill Windobserver II* wind speed sensor, which measures the northward and eastward wind component in m/s with a nominal precision of 2 % and 1 deg.

3.2 Acoustic Environment

Similar to electromagnetic waves, sound waves are refracted at interfaces that mark a change in sound speed. In an ocean environment, the speed of sound is in general a function of temperature, salinity, and depth. That is, changes in sound speed can occur continuously over the water column, resulting in a complex refraction pattern of sound waves. The sound speed profile, which describes the speed of sound as a function of depth, can therefore be used to characterize an ocean environment in terms of its acoustic propagation properties. In the following, typical sound speed profiles for the deep and shallow location are presented and the implications about how well sound generated at the surface reaches the bottomed hydrophones are stated.

3.2.1 Sound Speed Profiles

Conductivity, temperature, and depth (CTD) sensors collocated with the hydrophones are used to compute sound speed profiles for the deep and shallow location according to Equation 3 to 5 in [14]. Multiple CTDs are operating at different depth at each location and the data are combined to obtain sound speed profiles over the entire water column. Both locations have a CTD connected to the surface buoy (7 m depth), a shallow profiler CTD moving up and down the water column (between 20 - 200 m for the deep and 0 - 80 m for the shallow location), and a bottomed CTD at the hydrophone. Additionally, the deep location has a deep profiler CTD (175 - 500 m; was only operating a few times during the measurement period) and a CTD at a 200 m platform. The CTD data can also be downloaded from the OOI servers[5]

The data were used to compute sound speed profiles for various months and years between 2015 and 2019. Typical summer and winter profiles for both locations are shown in Figure 3.2. Except for the December profile at the shallow location, the sound speed generally deceases with increasing depth. According to Snell's law, sound waves always bend toward regions with minimum sound speed [30]. Therefore, a profile where the sound speed decreases with depth, i.e., a downward refracting sound speed profile, allows most surface generated sound waves to reach the ocean floor and therefore the bottom mounted hydrophone. Furthermore, a sound speed minimum can serve as a duct trapping acoustic waves and allowing them to travel over long distances without any surface or bottom interaction. Such a sound speed minimum can be observed at the deep location between 0 - 100 m during August.

In contrast to the summer profiles (July and August), the sound speed in winter (December and February) shows less variability over the water column. Especially at the shallow

[5]NFS Ocean Observatories Initiative Data Portal, `https://ooinet.oceanobservatories.org` CTD (shallow location: surface buoy CTD – CE02SHSM-RID27-03-CTDBPC000, shallow profiler – CE02SHSP-SP001-08-CTDPFJ000, hydrophone CTD – CE02SHBP-LJ01D-06-CTDBPN106; deep location: surface buoy CTD – CE04OSSM-RID27-03-CTDBPC000 , shallow profiler – CE04OSPS-SF01B-2A-CTDPFA107 , 200 m platform – CE04OSPS-PC01B-4A-CTDPFA109 , deep profiler – CE04OSPD-DP01B-01-CTDPFL105 , hydrophone CTD – CE04OSBP-LJ01C-06-CTDBPO108) data from 01 September 2015 to 31 December 2019. Downloaded on 26 January 2021

location the speed of sound is almost constant during December. The variations in sound speed between summer and winter months indicate that the propagation pattern varies seasonally. The effects of variations in sound speed on the acoustic propagation and, thus, on the noise levels measured at the hydrophones are, however, complex and go beyond the scope of this work. Instead, the next section will focus on how the sound speed profiles generally impact the ability of the hydrophones to measure sound emitted near the surface.

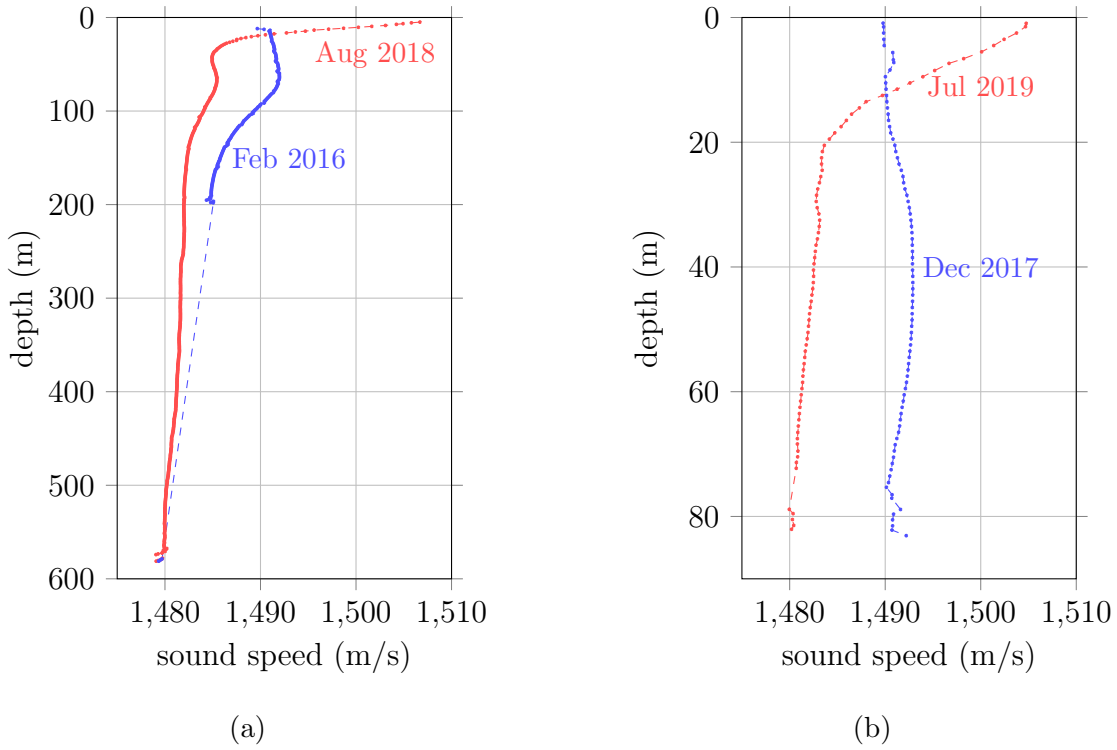

Figure 3.2: Typical summer and winter sound speed profiles for (a) deep and (b) shallow location. Note that the dashed line in the February profile of the deep location indicates that the deep profiler was not operating and, thus, no CTD data between 200 - 580 m are available.

3.2.2 Surface Listening Area

The effective surface listening area of a hydrophone can be defined as the surface area that emits 90 % of the energy received by the hydrophone. The authors in [3] have shown that this area is a function of hydrophone depth and acoustic frequency. Estimating the surface listening area is not trivial, especially in environments with highly depth dependent sound speed profiles. Therefore, ray simulations in the modeling software Bellhop [54] have been used together with the sound speed profiles in Figure 3.2 to estimate the surface listening areas for both locations at three different frequencies. To do so, a point source was placed at 1 m depth and the sound energy at the bottom was computed over a range of 0 - 5 km in 1 m increments. The water depth was set to be constant over the 5 km range and a sand-silt-clay bottom with constant sound speed of 1579 m/s, density of 1596 kg/m^3, and absorption coefficient of 0.27 dB/wavelength [23, 24] was assumed. The simulations return an array of sound energy values at the bottom as a function of range $E_\mathrm{b}(r)$. This can be used to compute the fraction of received energy as a function of range:

$$e(r) = \frac{\sum_{l=0}^{r} E_\mathrm{b}(l)}{\sum_{l=0}^{5000} E_\mathrm{b}(l)}. \tag{3.1}$$

Thereby it is assumed that no significant energy is received beyond 5 km. For each frequency and location, $e(r)$ is computed for both sound speed profile in Figure 3.2. The results are shown in Figure 3.3. The range over which 90 % of the energy is received – in the following called effective listening radius – is also marked. Horizontal bars and annotated numbers indicate the differences in effective listening radius between summer and winter months and the average listening radii, respectively. At the deep location, the effective listening radius is larger in summer than in winter for the 5 and 15 kHz frequencies, but larger in winter for a frequency of 500 Hz and takes on values roughly between 2.5 and 5 times the hydrophone depth (581 m), with a maximum radius at 5 kHz. At the shallow location the effective listening radius is always smaller during summer and takes on values between 3 and 13 times the hydrophone depth (81 m), where the maximum occurs again at 5 kHz.

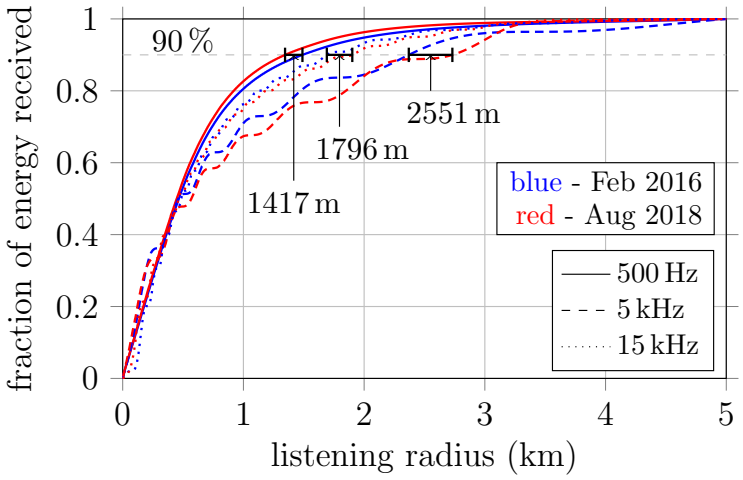

(a) deep hydrophone

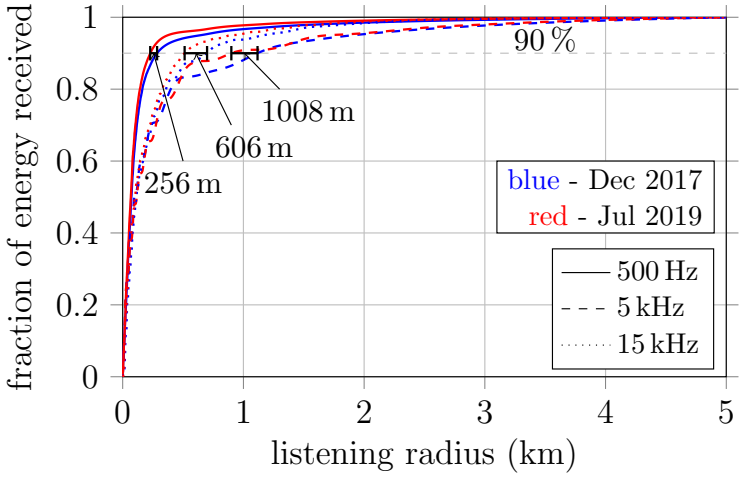

(b) shallow hydrophone

Figure 3.3: Faction of sound energy received by the hydrophones for different listening radii and acoustic frequencies for the (a) deep and (b) shallow location. The effective listening radius is defined as the range over which 90 % of the total energy is received.

The effective surface listening radius effects the spatial averaging of noise. That is, a larger listening radius means that, for example, the noise from more wave breaking events

is averaged together, or as a rain shower passes over the measurement location, the onset of rain can be detected earlier in the acoustic signal. The authors in [3] have shown that rain noise measured by a deep hydrophone (in [3] a depth of 1 km and 2 km), and therefore averaged over a larger surface area, shows a better correlation with radar rain measurements averaged over a larger area than with rain measured and averaged over a small area above the hydrophone. Rain noise measured by a hydrophone deployed in 60 m depth on the other hand, shows better correlation to rainfall averaged over a small area. As the rain rate in this study is measured by a single surface buoy and so no spatial averaging is performed, the correlation between rain rate and underwater noise is therefore expected to be better at the shallow location.

3.3 Processing of Acoustic Data

Power Spectral Densities (PSDs) are calculated using a modified version of the Welch's overlapped segment averaging method [71], which is computationally efficient and, thus, suitable for handling large data sets. The Python package OOIPy [59] was developed and used for these calculations. A Hann window was applied to 64 ms (4096 samples) data blocks, with 32 ms overlaps (50 %), to minimize the spectral leakage at the corners. Afterwards, a frequency-wise median averaging was applied to the 4096-point fast Fourier transforms of 1875 data blocks to produce sequential 1-min power spectrum levels for all rain rate and wind speed samples. It is noted that the actual number of data blocks varies between 937 and 2031 as the surface buoy provides data in intervals between 30 - 65 s. A frequency dependent sensitivity correction using the calibration data of the hydrophones is applied to the PSD estimates. The interference from Acoustic Doppler Current Profilers (ADCPs) co-located with the hydrophones are removed by using a median averaging in the Welch's method instead of a mean averaging [50, 58]. This Welch-median approach is described in Chapter 4 in more detail.

To solely focus on rain and wind noise, the acoustic data contaminated by other noises, such as ship noise, are manually flagged and removed from the analysis. To do so, sequential

1 h spectrograms with a linear frequency scale from 0 - 32 kHz were first computed for the entire dataset and, afterwards, manually inspected for the following types of distortions:

- ship noise with a time-frequency pattern as described in [36]
- broadband stationary interfering signals with a spectral level significantly above the background noise
- temporal discontinuities in the spectrograms typically indicated by the sudden onset or offset of broadband interferers.
- strong bioacoustic signatures in the low frequency region.

The second and third type of distortion is thought to be caused by other oceanographic instruments and the motors of the water column profilers operating at each location. Example spectrograms for those types of distortions are shown in Figure 3.4. When analyzing pure wind noise, spectrograms with rapid changes in spectral level were also flagged as spurious, as it is assumed that wind is rather stationary or only changes slowly over time (example in Figure 3.4d). Finally, all PSD estimates that fall into a spectrogram flagged as spurious were rejected from the analysis.

3.4 Processing of Meteorological Data

3.4.1 Rain Event Detection

The main challenge in automatically detecting rain events from the *RM Young* rain rate signal is the high variance of one-minute rain rate samples. Following the approach described in [33], a 21-point Hann-window is used as a moving average filter to reduce the variance of the rain rates and mitigate the effect of spikes. This is illustrated in Figure 3.5a, where the one-minute rain rate samples and the averaged rain rates are shown for six consecutive rain events captured by the deep surface rain gauge on May 20, 2016 between about 12:39 am and 01:58 pm. The figure shows that the rain rate may fluctuate with values up to ± 5 mm/h. However, the averaged rain rate eliminates the fluctuations and only keeps the peaks due to

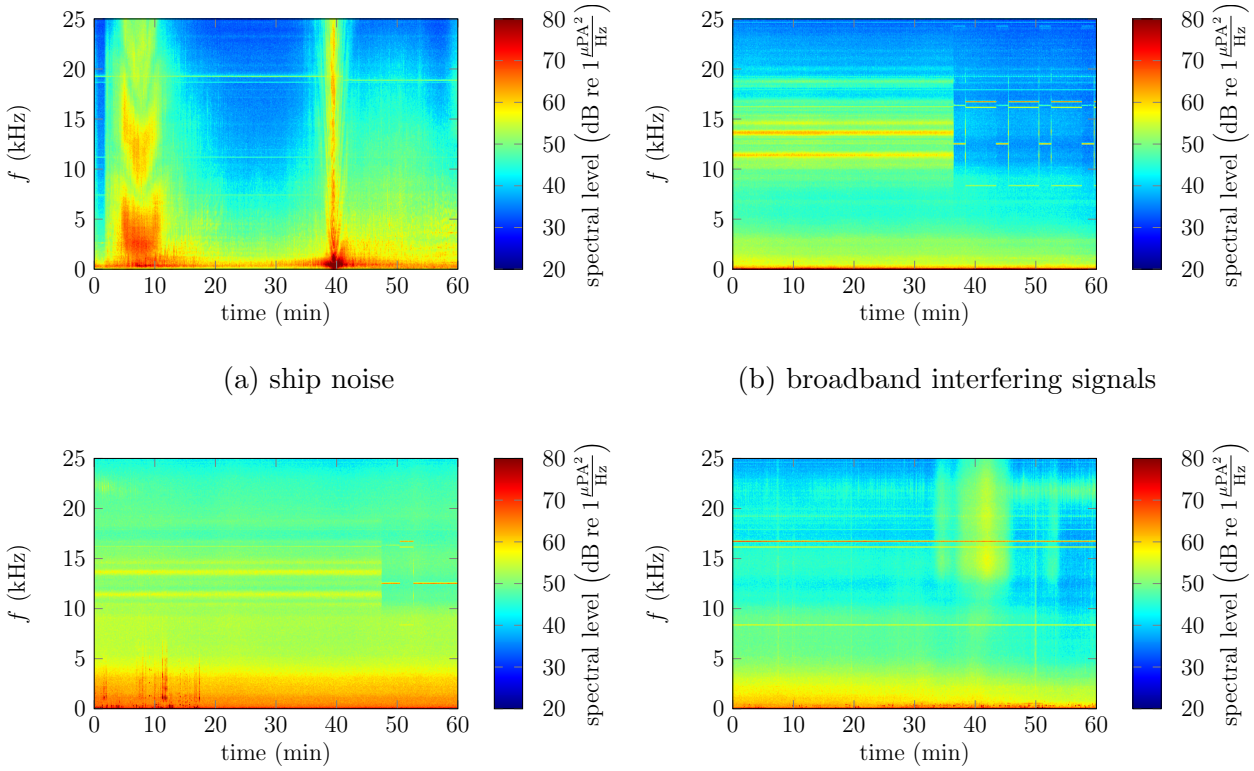

(a) ship noise

(b) broadband interfering signals

(c) bioacoustic noise

(d) sudden temporal changes in spectral level

Figure 3.4: Example spectrograms of different types of distortions that can be found in the acoustic data. (a) Two ship signatures. (b) Broadband interfering signal with sudden offset around minute 36. (c) Strong bioacoustic noise (minute 0 - 20), as well as broadband interfering signals. (d) Sudden temporal changes in spectral level at high frequencies (minute 35 - 45).

actual rain events. Each rain event consists of multiple rain rate samples that have values greater than a threshold, 1 mm/h in the context of this work. 10 samples are added before and after each rain event (not marked in Figure 3.5a) to ensure the beginning and ending of a rain event is captured accurately. Once the rain events are detected using the average rain rate, the original one-minute rain rate samples are assigned to the PSD estimates.

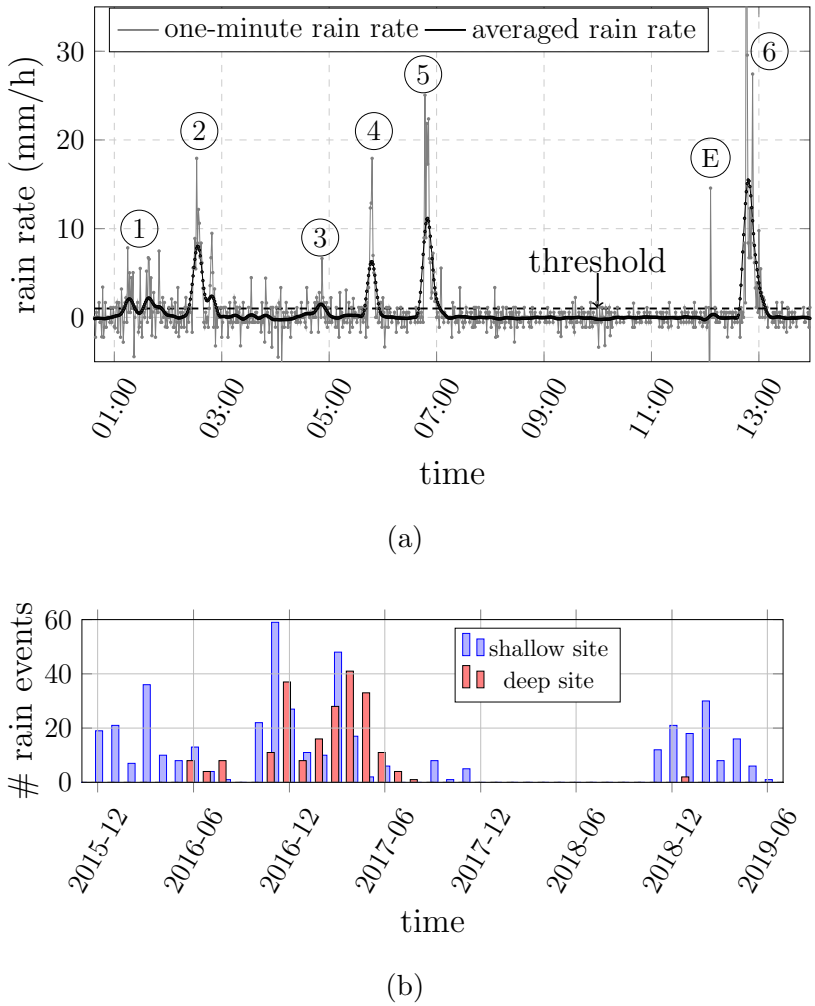

Figure 3.5: (a) Six rain events (circled numbers) during May 20, 2016 at the deep location. The gray and black lines show one-minute rain rate samples and the averaged rain rate using a 21-point Hann-window moving average filter, respectively. The averaged rain rate exhibits a significant reduction in measurement noise and faulty spikes such as point E are removed. A rain event is detected if the averaged rain rate exceeds 1 mm/h. (b) Distribution of rain events between December 2015 and June 2019 that have been evaluated at the deep and shallow location.

Using this method, 212 rain events at the deep location and 443 rain events at the shallow location have been detected. The distributions of those events throughout the entire measurement period are shown in Figure 3.5b.

3.4.2 Processing of Wind Data

The wind speed signal recorded at the surface buoy exhibits, similar to the rain rate, a large variance. As a result, the wind speed often rapidly changes from one sample to the next (see gray line in Figure 3.6a). However, as it is assumed that the average wind speed over a larger surface area does not change rapidly, but rather evolves slowly over time, the wind speed values are smoothed using a sliding 21-point symmetric Hann-window to reduce the measurement variance. The resulting smoothed wind speed signal is shown by the blue line in Figure 3.6a.

The distribution of wind-only data over the entire measurement period – after removing spectrograms that have been flagged as invalid – is shown in Figure 3.6b. Large gaps are usually due to times when hydrophones or surface buoys were not operating or when strong interfering signals were observed in the acoustic recordings over a long time period.

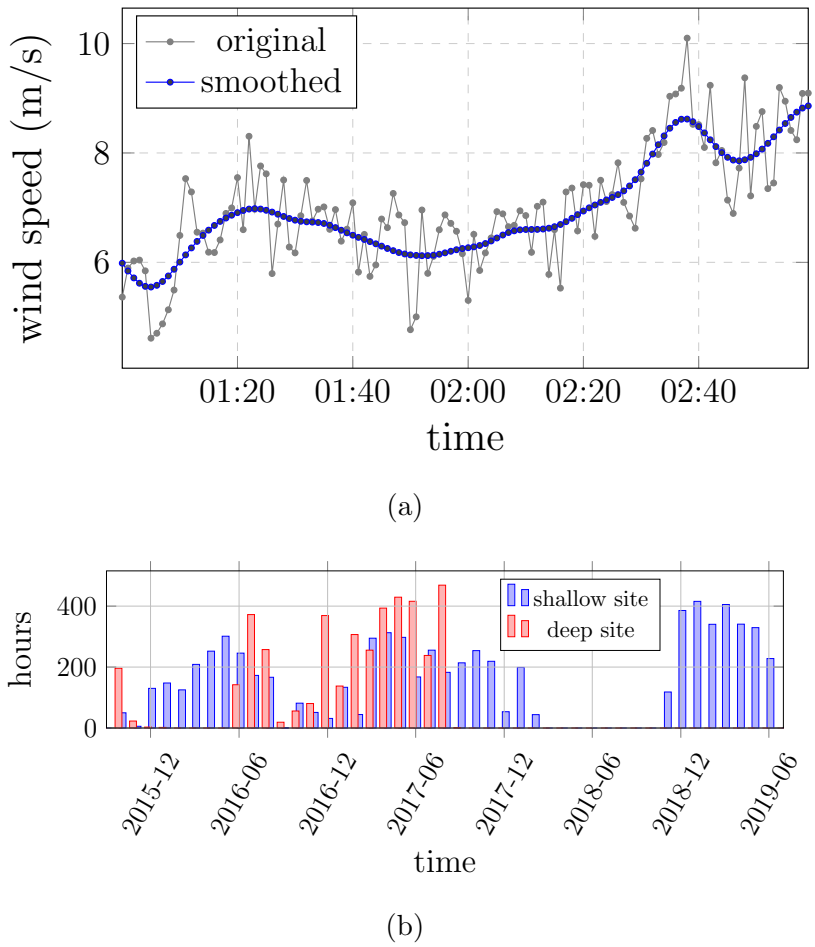

Figure 3.6: (a) Example of original and smoothed one-minute wind speed signal (data from January 1, 2017 at the deep location). The smoothing is performed using a 21-point sliding Hann-window. (b) Distribution of wind-only data over the measurement period after removing data corrupted by interfering signals as described in Section 3.3.

Chapter 4

WELCH PERCENTILE ESTIMATOR

In this chapter a spectral estimator for computing power spectral density (PSD) estimates of stationary signals that are compromised by outliers is presented [58]. The statistical properties of the estimator are derived and compared with simulations using white Gaussian noise. The performance of the method when a large percentage of outliers is present in the data is discussed as well.

4.1 Motivation

The Welch's overlapped segment averaging (WOSA) method, first introduced by Welch in 1967 [71], is a popular approach for estimating power spectral densities (PSDs) of stochastic signals due to its computational efficiency, its ability to scale estimation variance, and its potential to reduce spectral leakage. However, the method can suffer from strong outliers in the data caused by transients or other broadband interfering signals. Those outliers can prohibit an accurate estimation of the prevailing noise level, thus, limiting the scope of the WOSA estimator [35]. A possible solution, which has proven to be successful in several spectral estimation applications (see for example [2, 50, 39, 25]), is to take the median of the periodograms at each frequency bin instead of the arithmetic mean.

The main source of outliers in the ocean noise data at hand are pings from Acoustic Doppler Current Profilers (ADCPs). Those pings, which occur periodically, are transient broadband interfering signals with a duration of a few milliseconds. An example of 10 s of ocean noise compromised by ADCP pings is shown in Figure 4.1a. Figure 4.1b shows PSD estimates for the same 10 s of noise comparing mean (standard WOSA) and median averaging. As the ADCP pings behave like spectral outliers, many spikes can be observed in the

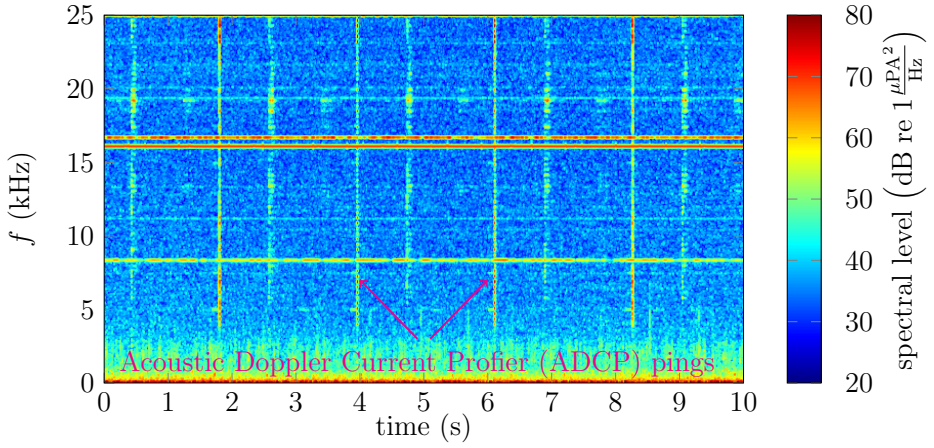

(a)

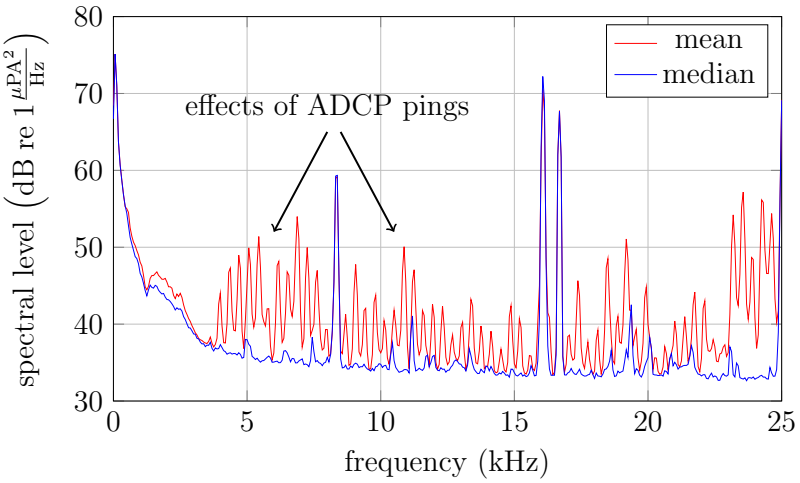

(b)

Figure 4.1: (a) Spectrogram with ADCP pings for 10 s of ocean noise during June 3, 2016 at the deep location. (b) PSD estimates for noise in (a) using the Welch method with standard mean averaging (red) and median averaging (blue). Only the median approach is robust against the ADCP pings and, thus, gives an accurate estimation of the underlying noise signal. The stationary spectral lines in (a) and (b) are probably caused by another instrument collocated with the hydrophone.

standard WOSA estimate. On the other hand, the Welch-median PSD gives a much cleaner estimate of the underlying noise with most spikes from the ADCP pings being removed.

The Welch median estimator can be regarded as a special case of a more general Welch estimator that uses sample percentiles, in the following referred to as Welch percentile (WP) estimator. While the statistical properties of the classical WOSA estimator have been analyzed thoroughly [71, 42, 52], respective results for the percentile estimator are less known. In the next two sections, I will formally define the WP estimator and provide its statistical properties. At the end of the chapter, the theoretical formulas will be compared to Monte Carlo simulations using data sampled from a white Gaussian noise process.

4.2 Welch Percentile Estimator

To compute PSD estimates using Welch's method, the time domain signal sampled from a stationary process with sampling frequency f_s is first divided into K potentially overlapping segments, each of which containing N_s samples. Each segment is then multiplied with a window function and the magnitude squared of their fast Fourier transform is computed. The result is a set of modified periodograms $\{\hat{P}_i(f_j)\}_{i=1}^{K}$. Therein, f_j refers to the j's Fourier frequency given by f_s/N_s and ˆindicates that each $\hat{P}_i(f_j)$ is an estimate of some true PSD $P(f_j)$. Finally, to obtain the standard WOSA estimate, the average of the modified periodograms is computed at each frequency f_j.

In contrast to the WOSA estimator, the WP estimator computes the q^{th} sample quantile of the set $\{\hat{P}_i(f_j)\}$ for each f_j (which is equivalent to the $p = q{\cdot}100$ percentile). To do so, first the order statistic $\{\hat{P}_{(1)}, \ldots, \hat{P}_{(K)}\}$ is determined at each frequency bin. (The dependence on f_j has been dropped for the sake of brevity.) Afterwards, the q^{th} sample quantile can be computed according to [51] as

$$\hat{Q}(q) = K\left(\frac{i}{K} - q\right)\hat{P}_{(i-1)} + K\left(q - \frac{i-1}{K}\right)\hat{P}_{(i)}$$
$$\text{for} \quad \frac{i-1}{K} \leq q \leq \frac{i}{K} \quad \text{and} \quad i = 1, \ldots, K. \quad (4.1)$$

That is, if the desired quantile falls between two samples $\hat{P}_{(i-1)}$ and $\hat{P}_{(i)}$, the sample quantile is estimated via linear interpolation. As I will show in Section 4.3, the sample quantile is, in general, biased compared to the true PSD, whereby the bias b depends on q and K. Hence, the final WP estimator can be defined as

$$\hat{P}_q^{(\mathrm{WP})} = \frac{\hat{Q}(q)}{b(q, K)}. \quad (4.2)$$

The procedure for computing PSD estimated using the WP and standard WOSA methods is illustrated in Figure 4.2.

4.3 Statistical Properties of the WP Estimator

The statistical properties of the WP estimator can be derived from the order statistics $\{\hat{P}_{(1)}, \ldots, \hat{P}_{(K)}\}$ of the modified periodograms. The derivations of bias, variance, and limiting distribution are given in Appendix A and the main results are summarized below.

4.3.1 Bias

As shown in [2] for $q = 0.5$ (i.e., the sample median) and for odd K the bias can be expressed as

$$b = \sum_{k=1}^{K} \frac{(-1)^{k+1}}{k}. \quad (4.3)$$

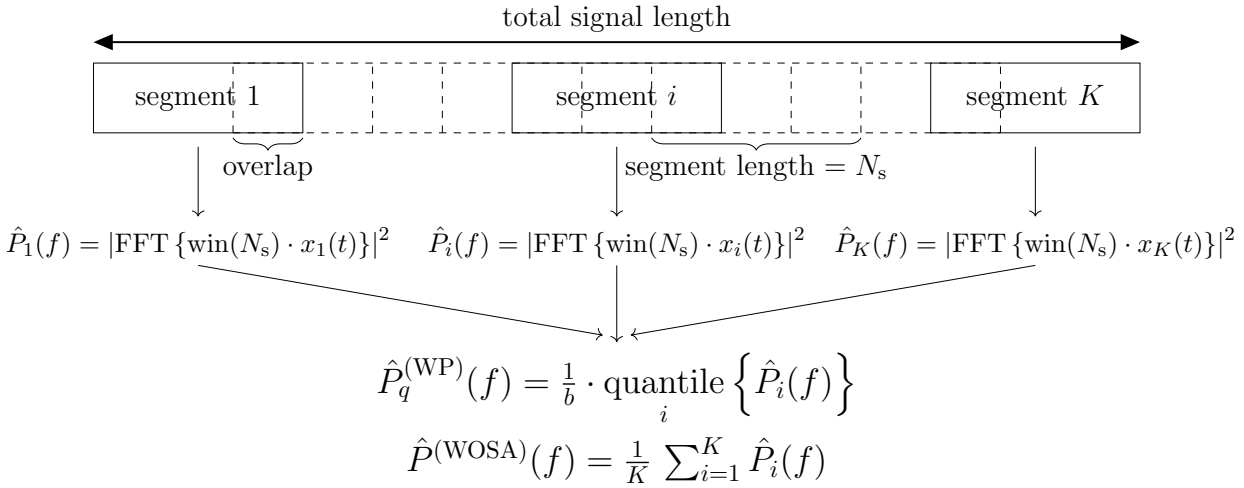

Figure 4.2: Procedure for computing PSD estimated using the Welch percentile (WP) and standard Welch (WOSA) methods. After the signal is divided into K segments, a modified periodgram $\hat{P}_i$ is computed for each segment. While the WOSA estimate is then the average over all periodograms, the WP estimate computes the q^{th} quantile for each frequency bin according to Equation (4.1).

For arbitrary quantiles and values of K, the bias can be computed by

$$b = \begin{cases} \sum\limits_{k=(K-1)(1-q)+1}^{K} \frac{1}{k}, & \hat{Q}(q) = \hat{P}_{(i)} \\ \sum\limits_{k=K(1-q)+1}^{K+1} \frac{1}{k}, & \hat{P}_{(i-1)} < \hat{Q}(q) < \hat{P}_{(i)} \end{cases} . \tag{4.4}$$

If $(K-1)(1-q)$ and $K(1-q)$ are not integers, the approximation of the digamma function

$$\psi(n) \approx \ln(n) - \frac{1}{2n} - \frac{1}{12n^2} + \frac{1}{120n^4} - \frac{1}{252n^6} \tag{4.5}$$

can be used to obtain the bias:

$$b = \psi(K+2) - \psi(K(1-q)+1). \tag{4.6}$$

In the limit, that is, for $K \longrightarrow \infty$ all bias formulas converge to $-\ln(1-q)$.

4.3.2 Variance

The WP estimator's variance can be computed by

$$\mathrm{var}\{\hat{P}_q^{(\mathrm{WP})}\} = \frac{P^2}{b^2}\left[\psi_1(K(1-q)+1) - \psi_1(K+2)\right], \tag{4.7}$$

where $\psi_1(n)$ is the derivative of the digamma function – also referred to as trigamma function – and can be approximated by means of Equation (4.5) as

$$\psi_1(n) = \frac{\mathrm{d}\psi(n)}{\mathrm{d}n} \approx \frac{1}{n} + \frac{1}{2n^2} + \frac{1}{6n^3} - \frac{1}{30n^5} + \frac{1}{42n^7}. \tag{4.8}$$

4.3.3 Limiting Distribution

For $K \to \infty$, the order statistic of the modified periodograms is normally distributed. Therefore, the bias corrected WP estimator has zero-mean and limiting variance

$$\mathrm{var}\{P_q^{(\mathrm{WP})}\} = \left(\frac{P}{b}\right)^2 \cdot \frac{q}{K(1-q)}. \tag{4.9}$$

4.3.4 Equivalent Degree of Freedom

So far, it is assumed that adjacent periodograms are approximately independent. This condition can be relaxed by introducing the concept of equivalent degree of freedom (EDOF) to get the number of independent random variables of the quantile estimation. According to [52, p. 429], the EDOF ν for the WOSA estimator is

$$\nu = \frac{2K}{1 + 2\sum\limits_{m=1}^{K-1}\left(1 - \frac{m}{K}\right)\left|\sum\limits_{t=0}^{N_\mathrm{s}-1} h_t h_{t+mN_\mathrm{o}}\right|}, \tag{4.10}$$

where h_t is the data taper and N_o is the number of overlapping samples. Since the same periodograms are used for the WOSA and WP estimator, Equation (4.10) also holds for the

latter one. That is, the WP estimator uses $\nu/2$ equivalent and independent periodograms to estimate the true PSD. Bias, variance, and limiting variance can now be computed for arbitrary overlaps and data taper when K is replaced by $\nu/2$. (Note that in Equation (4.4), $\nu/2$ and the product $\frac{\nu}{2}(1-q)$ would need to be rounded to the next nearest integers.)

4.4 Simulations

Here, I will compare the previously derived expressions for bias and variance with results from a simulated white Gaussian noise sequence. All data segments have a length of $N_\mathrm{s} = 1024$ and a Hann data taper with 50 % overlap is used. Subsequently, the WP estimate according to Equation (4.1) and (4.2) is computed for various q and $K \geq 3$, and sampling bias and variance are calculated. To reduce the variability in the estimate, 51 100 independent trials are averaged for each K and q. Furthermore, the EDOF instead of K is used in all formulas. It is noted that the goodness of fit between simulations and theoretical results is independent of the data taper if the EDOF is used. This has been tested using the Slepian, Parzen, and triangular window.

Figure 4.3 shows the the bias of the Welch 50^{th} percentile estimator after applying the bias correction using Equation (4.3), (4.4), and the limit $b = -\ln(0.5)$. If $\nu/2$ rounded to the next nearest integer is odd, Equation (4.3) and (4.4) give identical results with bias values smaller than 0.1 dB for $K \geq 7$. However, if $\nu/2$ is even, only Equation (4.4) is capable of accurately compensating the bias. Note that the rounded $\nu/2$ is in general not equal to K for the given window and overlap. When using the limit of the bias ($b = -\ln(0.5)$) equally good results for even and odd K are obtained, but the performance is worse compared to Equation (4.4). In general the truncated harmonic series is favorable as it gives the lowest bias over all K. However, for sufficiently large K, accurate results can be achieved for all three bias correction expressions.

The bias of the WP estimator for different percentiles is shown in Figure 4.4. Therein, the digamma approximation (Equation (4.5) and (4.6)) is used to compensate for the quantile bias. One can observe that, for small values of K, more extreme percentiles tend to over or

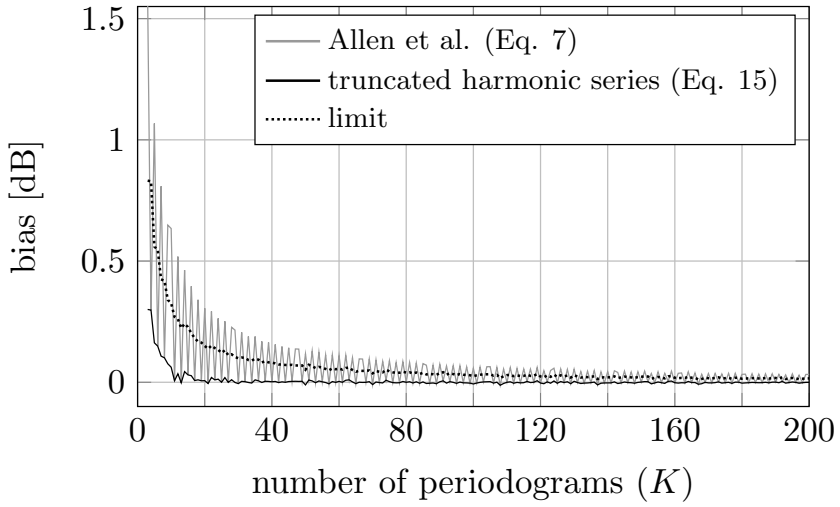

Figure 4.3: Bias of the Welch 50^{th} percentile estimator after correcting the quantile bias according to Equation (4.3), (4.4) (truncated harmonic series), and $b = -\ln(0.5)$ (limit). The lowest bias is achieved for the truncated harmonic series bias correction.

underestimate the true PSD, whereas percentiles around 63 % (unbiased estimator) exhibit only a small or no bias. Only for the 1^{st} and 99^{th} percentile a bias greater than 0.1 dB can still be observed for some $K \geq 30$. (This bias will also vanish as K further increases.)

Finally, variance and limiting variance according to Equation (4.7) and (4.9) are compared to the sampling variance of the WP estimator in Figure 4.5. The bias is corrected using the digamma approximation. The results show that Equation (4.7) deviates by less than 0.5 dB from the simulations for $K \geq 16$ and percentiles between 10 % and 90 %. The limiting variance (Equation (4.9)), on the other hand, requires values $K \geq 79$ to provide the same accuracy. For the 1^{st} and 99^{th} percentile, a greater deviation between theoretical expressions and simulations can be observed. In these cases, larger values of K would be necessary to achieve a better fit. Figure 4.5 also shows that the variance of the 50^{th} percentile estimator (median) is larger compared to the variance of the 90^{th} percentile estimator. Indeed one can compute a minimum variance WP estimator by plugging in the limiting bias $b = -\ln(1-q)$

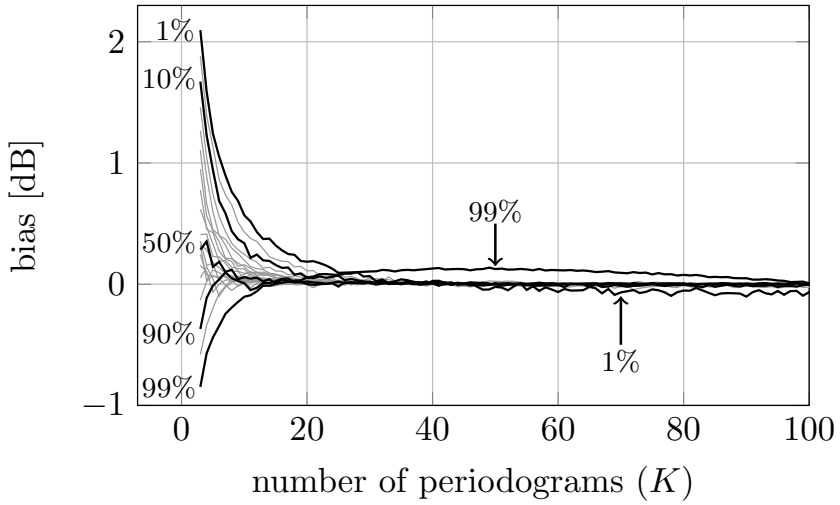

Figure 4.4: Bias of the WP estimator for percentiles between 1 % and 99 % in 5 % increments after correcting the quantile bias using the digamma approximation (Equation (4.5) and (4.6)). Except for the 1st and 99th percentile estimator, the bias quickly decreases to zero as the number of periodograms increases.

into the limiting variance (Equation (4.9)) and normalizing the result by P^2/K, which is the limiting variance of the standard WOSA estimator[1]. This yields the normalized variance

$$\tilde{\sigma} = \frac{\operatorname{var}\left\{\hat{P}_q^{(\mathrm{WP})}\right\}}{\operatorname{var}\left\{\hat{P}^{(\mathrm{WOSA})}\right\}} = \frac{q}{b^2(1-q)}. \tag{4.11}$$

Figure 4.6 shows $\tilde{\sigma}$ as a function of q. One can see that, in the limit, the 80th percentile estimator has the lowest variance – by a factor of approximately 1.3 dB compared to the median – among all WP estimators.

4.5 Outlier Correction

The WP estimator performs well if the percentage of outliers in the data is small (approximately less than 5 % of the periodograms are affected). However, if the number of outliers

[1] assuming all periodograms are statistically independent

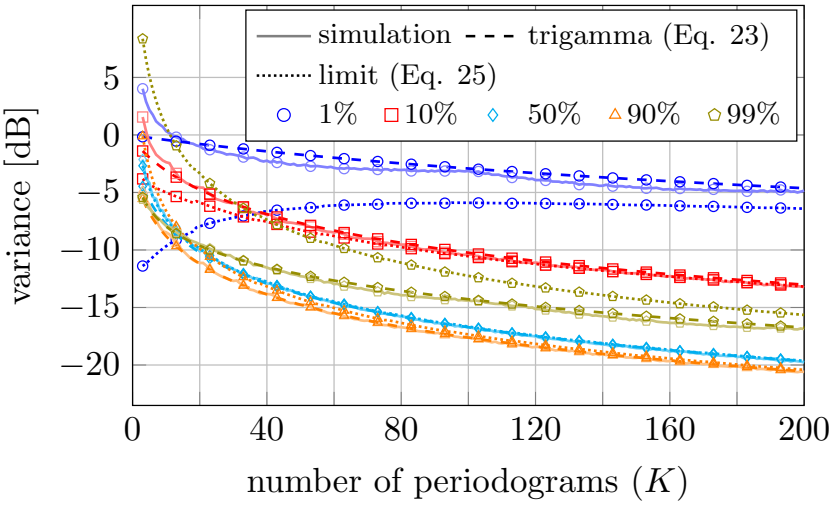

Figure 4.5: Simulated and theoretical variance according to Equation (4.7) (trigamma) and Equation (4.9) (limit) of the WP estimator. Especially the trigamma equation approximates the WP estimator's variance very accurately over a wide range of percentiles and values of K.

growth, the estimator becomes increasingly biased. This is illustrated in Figure 4.7a and 4.7b. The former one shows a white noise signal in time domain with many strong outliers at the beginning of the sequence. The outliers are placed in such a way that 30 % of the periodograms are affected, whereas the remaining 70 % are outlier-free. The corresponding 50^{th} percentile estimate is shown in Figure 4.7b (a 1024-point Hann window with 50 % overlap is used, so that the number of periodograms $K = 100$). One can clearly see that the spectral estimate has a bias of about 2.5 dB compared to the true PSD. This phenomenon can be explained by a significant change in distribution of the periodograms when many outliers are present. This is illustrated in Figure 4.7d. The left hand side shows the probability density function (PDF) of the periodograms in the absence of outliers, which, according to Equation (A.1), is proportional to a chi-square distribution with two degrees of freedom. In this case, when computing a Welch-50^{th} percentile estimate, the bias correction factor b has to account for the difference between the 50^{th} percentile and the unbiased 63^{rd} percentile

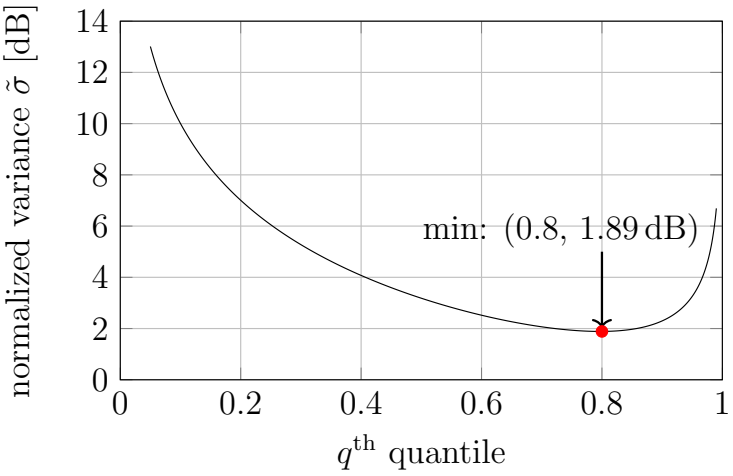

Figure 4.6: Normalized variance according to Equation (4.11) for various quantiles. The graph sows that the 80^{th} percentile estimator has the lowest variance among all WP estimators.

in order to estimate the true PDS. The right hand side of Figure 4.7d illustrated how the PDF changes if a large amount of outliers (here 30 %) are introduced in the data. Now, the unbiased estimator corresponds to the 44^{th} percentile and the bias correction would need to account for the difference between the 50^{th} percentile and the unbiased 44^{th} percentile. However, if instead the same bias correction as in the outlier-free case is applied, a significant bias occurs in the final PSD estimate.

A strong bias in the presence of outliers can be avoided if an additional bias correction factor e is introduced during the spectral estimation. To do so, the original values for q (corresponding to the q^{th} quantile) and K (corresponding to the number of periodograms) have to be replace in the equations for the bias (Equation (4.4) to (4.6)) by

$$q \longrightarrow \frac{q}{1-e} \tag{4.12a}$$

$$K \longrightarrow K(1-e), \tag{4.12b}$$

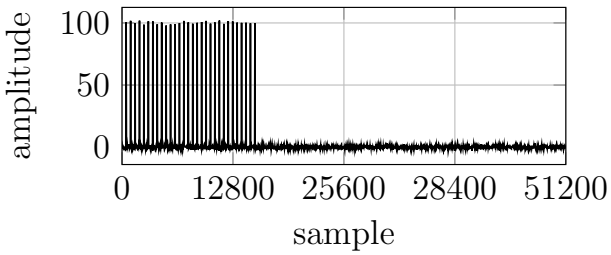

(a) White noise sequence in time domain

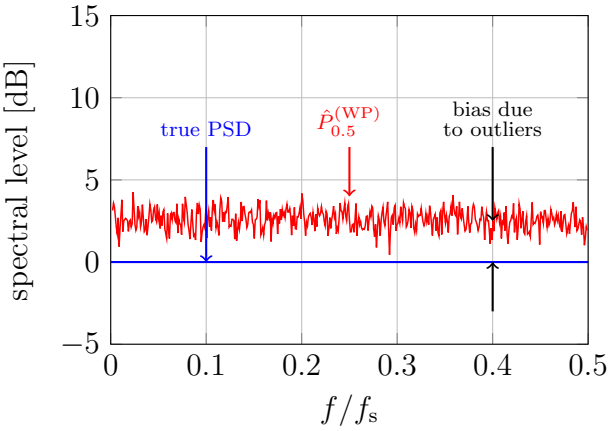

(b) WP estimate without outlier correction

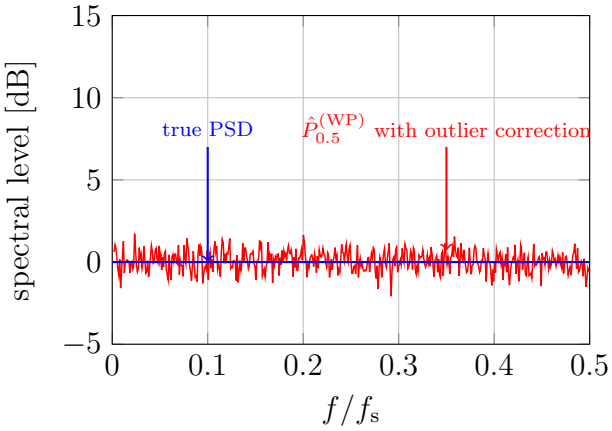

(c) WP estimate with outlier correction

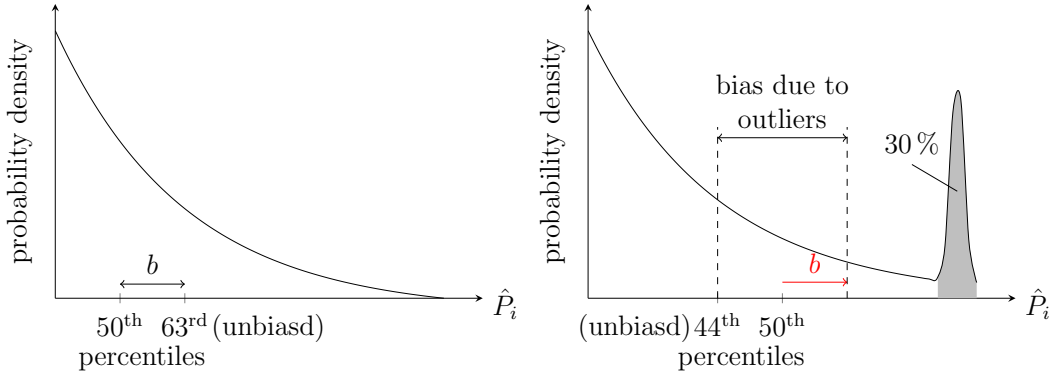

(d) PDF of periodograms without outliers (left) and with outliers (right)

Figure 4.7: Welch percentile estimate if the percentage of outliers in the data is large. (a) White noise sequence with outliers in time domain. The outliers are placed such that 30 % of the periodograms are effected. (b) Welch-50$^{\mathrm{th}}$ percentile estimate without outlier correction. (c) Welch-50$^{\mathrm{th}}$ percentile estimate with outlier correction using Equation (4.12). (d) Illustrations of a PDF of outlier-free periodograms (left) and of a PDF where 30 % of the periodograms are affected by outliers (right).

where e is the fraction of outliers in the data. This outlier correction factor applied to the white noise sequence in Figure 4.7a yields the spectral estimate in Figure 4.7c, which is unbiased compared to the true PSD. To obtain accurate estimates of the variance and liming distribution of the final estimate, the updated values for q and K also have to be used in Equation (4.7) and (4.9).

4.6 Conclusion

The WP estimator is a robust approach for computing PSD estimates. Equations for the bias of the underlying quantile estimate have been derived. The presented bias correction approach outperforms the existing method for the Welch 50^{th} percentile estimator and also performs excellent for other percentiles. Furthermore, simple expressions for the estimator's variance have been derived and comparisons with simulated data have shown great agreement for most percentiles and a wide range of sample sizes. It has been shown that the estimator can also be applied in scenarios where the percentage of outliers is large by incorporating an additional outlier correction factor.

Chapter 5

CHARACTERIZING WIND-GENERATED OCEAN AMBIENT NOISE

In this chapter the spectral characteristic of wind noise for various wind speed categories is analyzed by evaluating one-minute power spectral density (PSD) estimates as described in Section 3.3. To focus solely on noise generated by wind, PSD estimates coinciding with spectrograms flagged as spurious (see Section 3.3) or corresponding to rain events (see Section 3.4.1) are excluded form this analysis. First, the spectral trajectory, that is, the dependence of wind noise spectral levels on the acoustic frequency, is described and comparisons between the deep and shallow location, as well as with results from past studies, are made. Afterwards, the relation between sound spectral level and wind speed is modeled and its dependence on the acoustic frequency is analyzed.

5.1 Frequency Dependency

Wind noise spectral levels for wind speeds between 0 - 14 m/s have been grouped into seven wind speed categories, where each category covers an interval of 2 m/s. An eighth category for wind speeds above 14 m/s is also included. Average PSD estimates for each wind speed category are shown in Figure 5.1 for both locations. The frequency dependent standard deviation is illustrated by the shaded area around each average PSD. (For a better representation, only one quarter of the standard deviation is plotted.) It is noted that multiple narrow band tones, presumably caused by the measurement apparatus, can be detected in the acoustic signal[1]. Those tones have been removed in Figure 5.1 by linearly interpolating

[1]At the deep location, six strong tones approximately at 6.27 kHz, 8.34 kHz, 12.53 kHz, 14.03 kHz, 16.09 kHz, and 16.7 kHz were identified. At the shallow location, five tones approximately at 7.45 kHz, 11.17 kHz, 13.28 kHz, 15.31 kHz and 19.38 kHz were identified.

the spectral level over a range of approximately 190 Hz (12 samples) around each tone.

The OOI data set allows for the analysis of wind noise over a broad frequency range from 30 Hz up to 25 kHz. Figure 5.1 indicates that the wind noise spectra can be divided into three frequency ranges: (1) very low frequencies from 30 - 200 Hz, (2) low frequencies from 0.2 - 3 kHz and (3) high frequencies from 3 - 25 kHz. Frequencies below 30 Hz and above 25 kHz are filtered out and, thus, excluded from the analysis. The characteristic spectral shape of each frequency range will be discussed in the following.

5.1.1 30 - 200 Hz *Frequency Range*

For frequencies between 30 - 200 Hz, the spectral levels at the deep location are significantly higher compared to the shallow location. A similar phenomenon was also reported in other studies, such as in [7] and [20], and is likely caused by noise from distant ships [69, 4, 72] and high latitude winds [5] that propagate in the deep sound channel over long distances. As the acoustic environment at the shallow location is dominated by steep bottom and surface reflections, the influence of distant sources is negligible and no increased spectral levels at very low frequencies can be observed.

5.1.2 0.2 - 25 kHz *Frequency Range*

For both, the low frequency range (0.2 - 3 kHz) and the high frequency range (3 - 25 kHz), linear models of the form

$$SPL(f) = s \log_{10}(f) + a, \tag{5.1}$$

where SPL is the spectral level, and s and a are the linear regression coefficients, were fitted to the data. The regression curves are shown as dashed lines in Figure 5.1. To equally weight each frequency, the PSDs were first mapped into one-third octave bands for the low frequency range and one-sixth octave bands for the high frequency range, respectively (median averaging was used to mitigate the effect of outliers). The linear regression slopes for

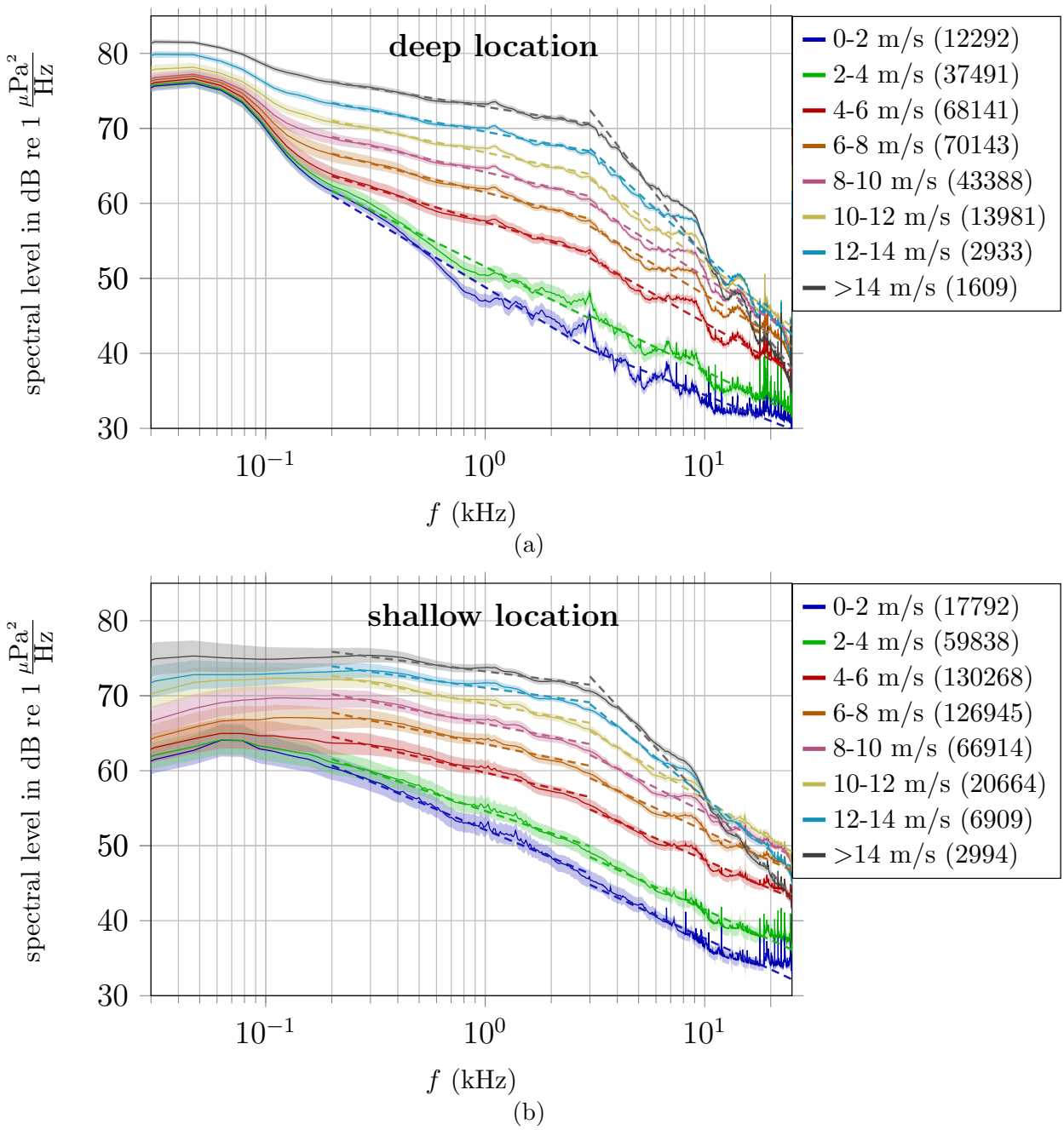

Figure 5.1: Average power spectral densities for (a) deep and (b) shallow location for various wind speed categories. The shaded areas around the solid lines indicate one quarter of the standard deviation. The dashed lines are obtained by linear regression of the spectra mapped into one-third octave bands (0.2 - 3 kHz frequency range) and one-sixth octave bands (3 - 25 kHz frequency range) using a median averaging. The number of one-minute PSD estimates within each wind speed category is given in parenthesis.

both locations are shown in Table 5.1. Furthermore, the coefficient of determination, denoted by R^2, has been computed as a metric for evaluating the performance of the regression model as it shows how much of the variability in the data can be explained by the linear model [22]. An R^2 score close to 1 indicates that the linear model explains most of the variability in the data and, thus, the linear model is a good fit. On the other hand, a low R^2 value indicates that the linear model is not a good fit. R^2 scores are computed using the average spectral levels, therefore neglecting the variance of the noise and resulting in values closer to 1.

Choosing a corner frequency of 3 kHz is based on the observation that the spectral levels shown in Figure 5.1 decrease more rapidly beyond 3 kHz especially for higher wind speeds. This suggests that wave breaking events have a different effect on the noise level in different frequency bands. Indeed for wind speeds below 4 m/s, where wave breaking events are assumed to be not significant [40, 41], the figure indicates that a single linear model would seem sufficient to describe the spectral behavior. Nevertheless, separate linear models for the 0.2 - 3 kHz and 3 - 25 kHz range are used in the following for all wind speed categories.

0.2 - 3 kHz range:

In the frequency range between 0.2 - 3 kHz the linear regression slope for both locations increases with increasing wind speed. However, the change in slope is not uniform. That is, for wind speeds below 6 m/s the slope increases rapidly with increasing wind speed, whereas above 6 m/s the increase in slope is much more gradual. Table 5.1 also shows that the slope at the deep location is steeper for all wind speed categories compared to the shallow location. This is likely a result of the greater measurement depth at the deep location and therefore a higher volume attenuation of sounds at high frequencies.

R^2 scores for the low frequency linear regression at the deep location are very close to one for wind speeds above 4 m/s. The slightly lower R^2 scores for wind speeds below 4 m/s can be attributed to the larger variability in the spectral level, probably caused by other noise sources that become dominant in the absence of wind. On the other hand, the R^2 scores for the shallow site tend to decrease as the wind speed increases. Figure 5.1b indicates that this

Table 5.1: Slope s in dB/dec according to Equation (5.1) and R^2 scores of linear regression performed on the average spectra in Figure 5.1 for the 0.2 - 3 kHz and 3 - 25 kHz range.

Wind speed (m/s)	$s_{0.2-3\,\mathrm{kHz}}$	$s_{3-25\,\mathrm{kHz}}$	$R^2_{0.2-3\,\mathrm{kHz}}$	$R^2_{3-25\,\mathrm{kHz}}$
		Deep location		
0-2	−17.53	−11.55	0.968	0.891
2-4	−14.51	−14.07	0.970	0.953
4-6	−8.77	−16.47	0.993	0.964
6-8	−7.39	−17.46	0.990	0.966
8-10	−6.72	−18.73	0.984	0.967
10-12	−6.04	−21.38	0.980	0.968
12-14	−5.47	−26.95	0.982	0.972
>14	−4.73	−37.50	0.983	0.975
		Shallow location		
0-2	−12.28	−13.70	0.996	0.958
2-4	−9.89	−13.42	0.993	0.974
4-6	−6.84	−12.86	0.967	0.981
6-8	−6.05	−13.39	0.960	0.982
8-10	−5.67	−14.63	0.968	0.984
10-12	−5.36	−17.51	0.971	0.988
12-14	−4.09	−23.76	0.931	0.991
>14	−3.74	−31.65	0.936	0.985

can be attributed to an increasingly non-linear trajectory of the wind noise spectral levels for higher wind speeds.

3 - 25 kHz range:

Spectral levels in the 3 - 25 kHz range decrease faster compared to the 0.2 - 3 kHz range. At

the shallow location and for wind speeds below 10 m/s the slopes for all wind speed categories are nearly identical with an average value of −13.6 dB/dec. This is in agreement with results from previous studies showing that wind noise spectral levels decrease over frequency with a rate independent of the prevailing wind speed [10, 18, 29, 32, 34, 66, 67, 72]. At the deep location on the other hand, the slope is not independent of the wind speed as it decreases from −11.6 dB/dec at 0 - 2 m/s to −18.7 dB/dec at 8 - 10 m/s. For wind speeds above 10 m/s, the slope significantly decreases with increasing wind speed at both locations. This last phenomenon follows the pattern reported in [8] and [19] during strong winds and can be explained by a layer of bubbles forming underneath the water surface and attenuating high frequency sound. The 3 - 25 kHz linear regression slopes are, except for the 0 - 2 m/s wind speed category, always smaller at the deep location than at the shallow location, which can likely be attributed to the greater measurement depth and, thus, increased volume attenuation at the deep location.

R^2 scores are in general very high for wind speeds above 2 m/s, supporting the use of a linear model. Below 2 m/s, a larger variability in sound level for the deep locations, probably caused by other noise sources, and a plateauing spectral level at frequencies above 20 kHz for the shallow location cause the R^2 scores to decrease.

5.1.3 Comparison with Literature

The wind noise spectra for the 4 - 6 m/s wind speed category are compared with spectra from previous studies in Figure 5.2. The literature results are taken from Ma et al. [34] who analyzed ambient noise in the tropical Pacific, Wenz [72] who combined results from various open ocean and coastal environments, Lemon et al. [32] who focused on continental shelf data from the Queen Charlotte Sound off the coast of Canada, and Knudsen et al. [29] who evaluated data from multiple near-shore locations around the world collected during World War II. Note that all studies reported a uniform slope for frequencies above 1 kHz (Knudsen even reported a uniform slope above 100 Hz). The data in this study show the greatest similarity with the results reported by Lemon and Knudsen. The similarity with the Lemon

data is less surprising as their measurements where conducted in a similar environment. He reported a slope around $-17\,\mathrm{dB/dec}$, which is very close to $s_{3-25\,\mathrm{kHz}} = -16.47\,\mathrm{dB/dec}$ at the deep location. Lemon used hydrophones deployed at the bottom in a depth of approximately 250 m, which can explain why their noise levels are in between the ones of the shallow location (81 m) and deep location (581 m). The comparison with the Lemon data supports the claim that wind noise spectral levels behave similar in absolute value and trajectory at comparable environments. The strong similarity of the deep hydrophone spectral levels with the Knudsen data is more surprising as their measurements where not obtained from an environment similar to the northeast Pacific continental margin.

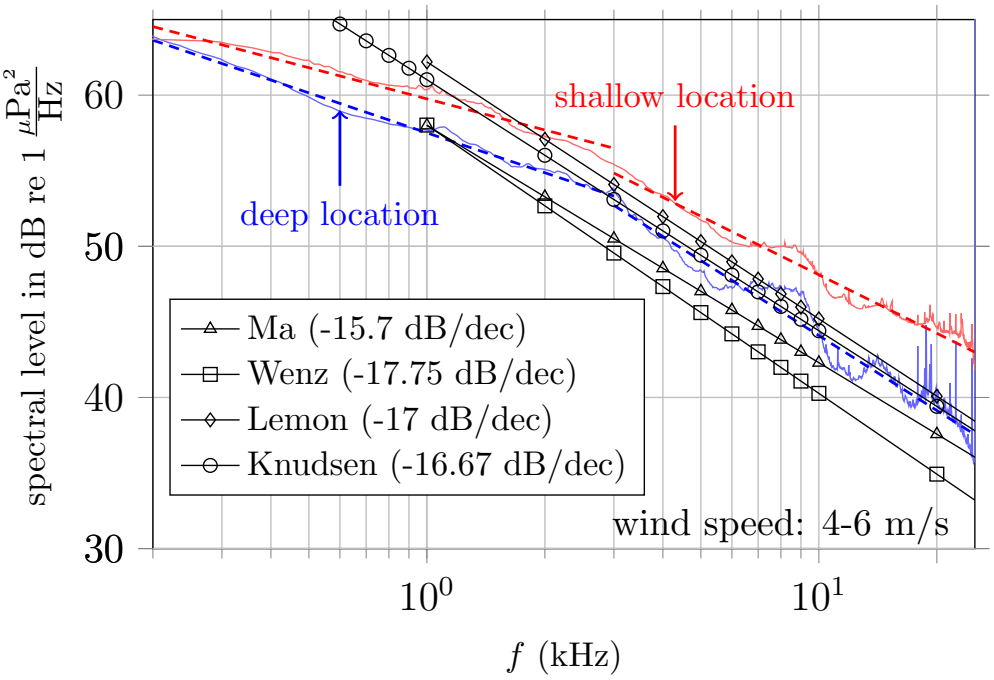

Figure 5.2: Wind noise spectral levels for the 4 - 6 m/s wind speed category compared with results from Ma et al. [34], Wenz [72], Lemon et al. [32], and Knudsen et al [29]. Deep and shallow spectral levels show good agreement in terms of absolute value and slope with the study by Lemon, which was conducted in a similar oceanic environment.

The studies by Wenz and Ma show lower spectral levels compared to the results in this work. This is likely caused by the difference in measurement location and depth (most of Ma's hydrophones were deployed in a depth of 38 m, whereas the exact measurement depth in Wenz's study is unknown). On the other hand, the spectral slopes obtained from those studies are similar to $s_{3-25\,\mathrm{kHz}}$ from the deep location. Further, it is interesting to note that the shallow location slope $s_{3-25\,\mathrm{kHz}} = -12.86\,\mathrm{dB/dec}$ is greater than any other previously reported slope listed in Table 2.1. This emphasizes the claim that wind noise levels cannot be easily generalized across different oceanic environments, bur rather distributed, large-scale measurements are necessary for an accurate characterization of wind noise at various locations.

5.2 Wind Speed Dependency

5.2.1 Pearson Correlation Coefficient

As discussed in Section 2.1 the relation between sound spectral level and wind speed is highly dependent on the acoustic frequency. One way to quantify this relation is using the Pearson correlation coefficient, which provides a measure of linear correlation between two random variables. That is, the correlation between sound spectral level SPL and wind speed v can be estimates by

$$r_{SPL,v}(f) = \frac{\sum_{i=1}^{N}(SPL_i(f) - \overline{SPL}(f))(v_i - \bar{v})}{\sqrt{\sum_{i=1}^{N}(SPL_i(f) - \overline{SPL}(f))^2}\sqrt{\sum_{i=1}^{N}(v_i - \bar{v})^2}}, \tag{5.2}$$

where SPL_i and v_i are the sound spectral level and wind speed of the i^{th} PSD estimate, $\overline{SPL}$ and $\bar{v}$ are their respective sample means, and N is the total number of one-minute PSD estimates. The resulting frequency dependent correlation coefficient is median-averaged into one-third octave bands and shown in Figure 5.3 (dashed lines). In past studies, the spectral level is usually related to the logarithm of the wind speed. Thus, the solid lines in Figure 5.3 show the Pearson coefficient with v being replaced by $\log(v)$. One can see that the correlation coefficient has a similar trajectory for both locations, with low values below 100 Hz and a

correlation of at least 0.8 at the shallow and 0.9 at the deep location for frequencies between 1 - 10 kHz. For frequencies below 7 kHz, the correlation is always higher when using v instead of $\log(v)$. However, this difference is not very large, especially for frequencies between 1 - 10 kHz, which is where most algorithms that convert between spectral level and wind speed operate. Nevertheless, the Pearson coefficient does not favor the logarithmic over the linear wind speed variable.

It is interesting to note that the correlation at the deep location is almost always higher compared to the shallow location. The lower correlation for the shallow location is likely a result of the smaller effective surface listening area and therefore lesser spatial averaging of wind noise (see Section 3.2 for a discussion about the effective surface listening area at both locations). That is, single wave breaking events have a stronger effect on the sound levels received by the shallow hydrophone resulting in a larger variability of the sound spectral levels for a given wind speed. This also reflects in the variance of the PSD estimates in Figure 5.1. Therein, spectral levels at the shallow location consistently show a larger variance than at the deep location, especially for frequencies below 1 kHz.

5.2.2 Two Wind Speed Regime Model

Since the Pearson correlation coefficients is a measure of linear correlation between wind speed and spectral level, the possibility of a two wind speed regime model as suggested by the literature is ignored. To check whether the data follow such a two regime model, the piecewise linear function

$$SPL(v) = \begin{cases} 20\,n_1\,\log_{10}(v) + SPL(v_\mathrm{c}) - 20\,n_1\,\log_{10}(v_\mathrm{c}), & v < v_\mathrm{c} \\ 20\,n_2\,\log_{10}(v) + SPL(v_\mathrm{c}) - 20\,n_2\,\log_{10}(v_\mathrm{c}), & v \geq v_\mathrm{c} \end{cases}, \tag{5.3}$$

where v_c is the critical wind wind speed and n_1 and n_2 are the slope coefficients, has been fitted to the data using the SciPy function *scipy.optimize.curve_fit* [68]. Note that the model is chosen such that the linear regression lines below and above v_c intersect at v_c. The model coefficients are computed for all 2049 frequency bin and median-averaged into one-third

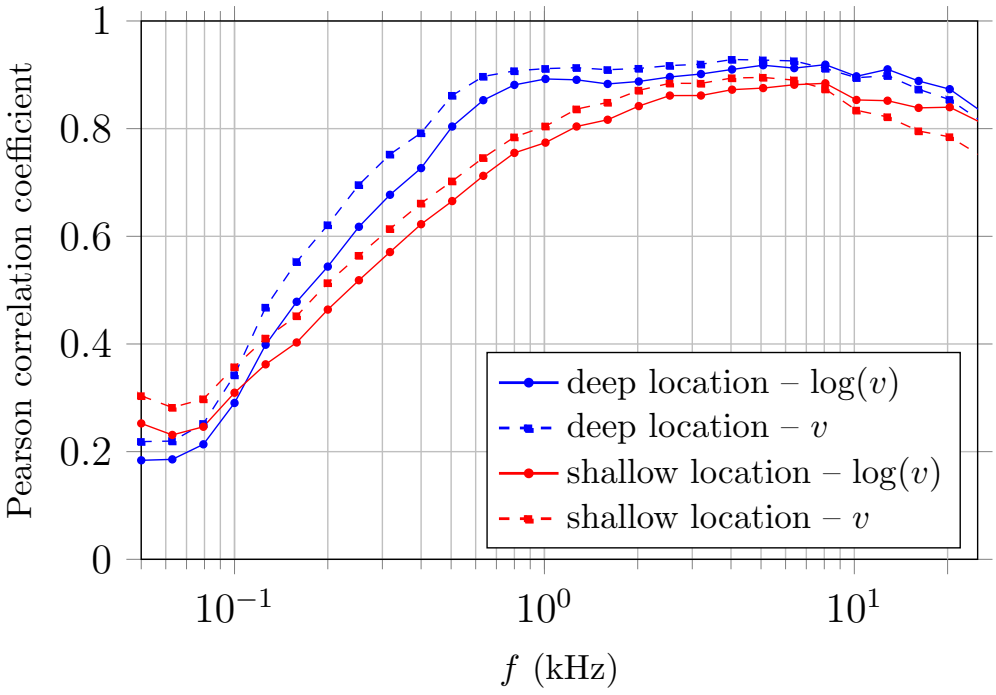

Figure 5.3: Pearson correlation coefficient according to Equation (5.2) between spectral level and wind speed v. For the solid curve, v in Equation (5.2) is replaced by $\log(v)$. The correlation is computed for all 2049 frequency bins between 0 - 32 kHz before being median-averaged into one-third octave bands.

octave bands. The resulting v_c, n_1, n_2, and R^2 score for the high wind speed regime (i.e., for the linear model when $v \geq v_c$)[2] are shown in Figure 5.4 for both locations.

The R^2 score shows the same pattern as the Pearson correlation coefficient in Figure 5.3. The critical wind speed v_c steadily decreases between 50 Hz and 1 kHz. Above 1 kHz, v_c remains almost constant with values between 2 - 3 m/s. This behavior is consistent with observations made in the past (for example, see Figure 6 in [53]), but, as of this point, has not been quantitatively analyzed over a wide frequency range. Note that for the deep

[2]As the spectral level below v_c is approximately constant, R^2 scores of the regression in the low wind speed regime assume values around zero. Therefore, a combined R^2 score for both regimes becomes hard to interpret, which is why only the R^2 score for the high wind speed regime is shown.

location and frequencies below approximately 150 Hz, the spectral level is mainly determined by distant sources rather than local winds. Therefore, the two-regime model cannot be fitted to the data in a meaningful way, which explains the strong fluctuations in v_c that can be observed below 150 Hz. The slope coefficients n_1 and n_2 also behave similar among both locations. n_1 assumes values around 0.1 over the entire frequency range, indicating that the spectral level is almost independent of the wind speed below v_c. On the other hand, n_2 assumes values between 1 - 1.6 with a broad maximum between 1 - 10 kHz. Those values are at the upper end of the range found in previous studies (see Table 2.2). As mentioned in Section 2.1 this could be due to the fact that many studies in the past used a single wind speed regime model, thus, potentially underestimating the slope above v_c.

An example of the two regime model fitted to the spectral level at 5 kHz is shown in Figure 5.5. For the deep location, the critical wind speed is $v_c = 2.33$ m/s, and n_1 and n_2 are 0.089 and 1.55, respectively. For the shallow location, $v_c = 2.55$ m/s, and n_1 and n_2 are 0.099 and 1.47, respectively. The average spectral level within each 2 m/s wind speed category is shown by the square markers. One can observe that the two regime model coincides very well with the average spectral levels. Only for very high wind speeds (above approximately 15 m/s) the model seems to underestimate the prevailing wind speed, but more data for very high wind speeds is necessary to confirm this trend and extend the model to higher wind speeds.

The results are also compared to data taken from studies by Lemon et al. [32] and Vagle et al. [66], who both used a single wind speed regime model. The Lemon and Vagle data are shown for frequencies of 4.3 kHz and 5 kHz, respectively. Vagle evaluated wind noise measurement from the tropical Atlantic Ocean with hydrophones deployed in a depth of approximately 150 m. Additionally, he normalized the spectral levels to a depth of 1 m and used a quadratic model to describe the spectral level versus log wind speed relation. The results from both studies agree very well in absolute spectral level with the data at the shallow location. At the deep location on the other hand, the data from this study show consistently lower spectral levels than the Lemon and Vagle data, which is likely a result of the greater

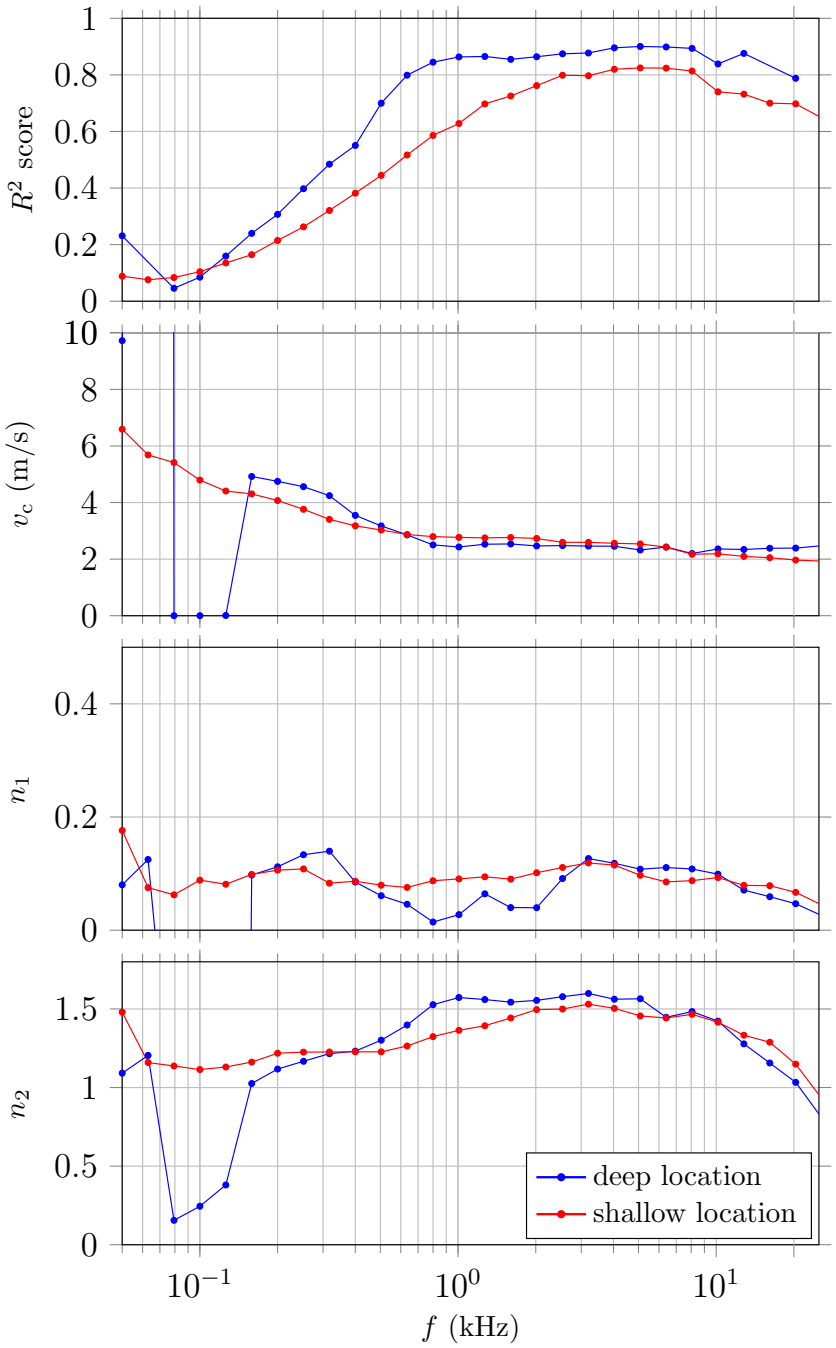

Figure 5.4: R^2 score of the high wind speed regime, critical wind speed v_c, and slope coefficients n_1 and n_2 of the two wind speed regime linear model according to Equation (5.3). Each parameter is computed for all 2049 frequency bins between 0 - 32 kHz before being median-averaged into into one-third octave bands. Very low frequencies at the deep location are not related to the local wind speed, which explains the strong fluctuations in v_c, n_1, and n_2 below 150 Hz.

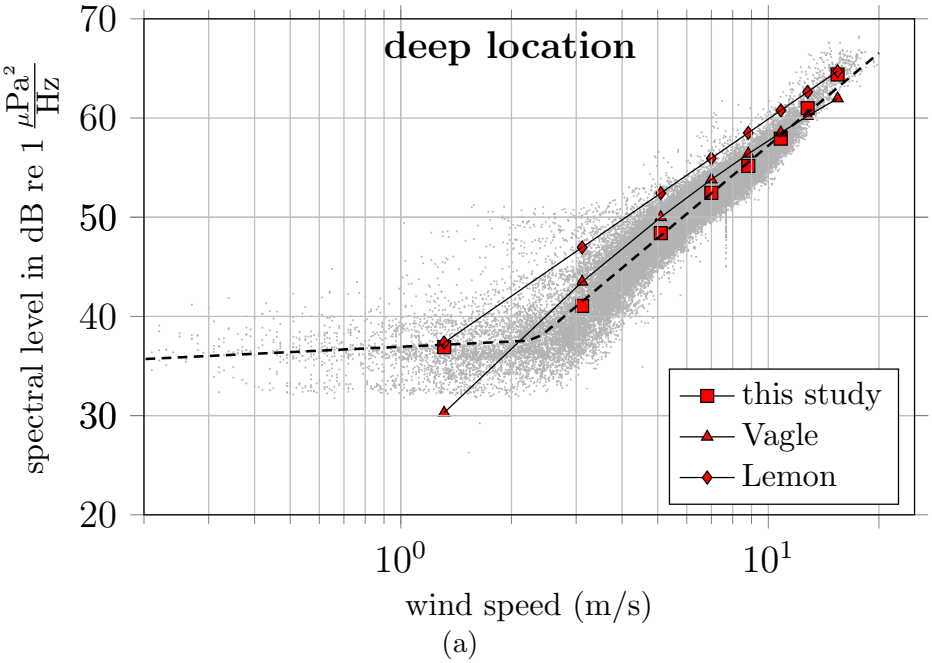

(a)

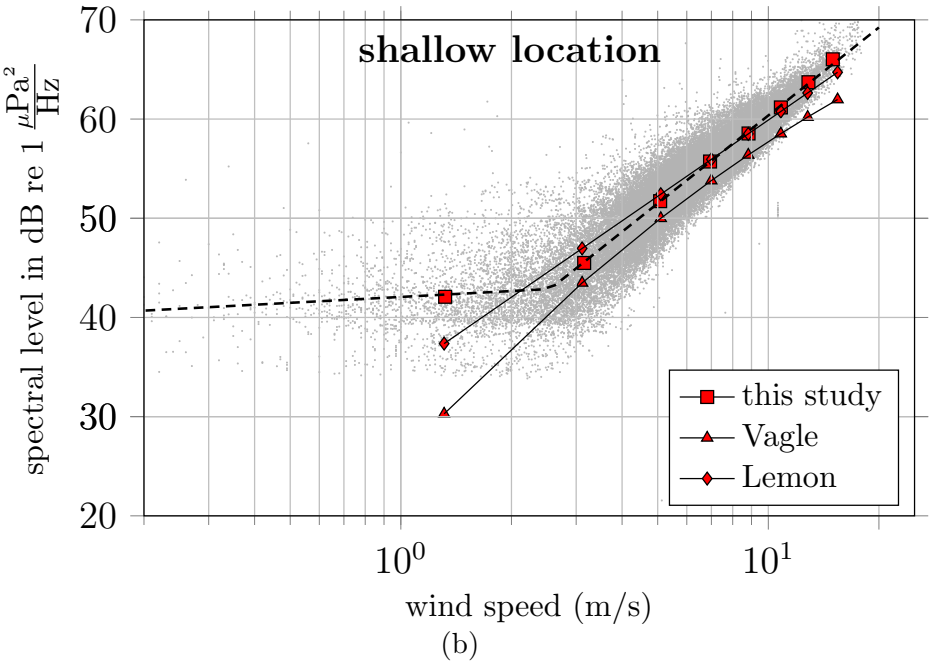

(b)

Figure 5.5: Spectral level at 5 kHz over the logarithmic wind speed for (a) deep and (b) shallow location. The dashed lines are the two regime linear models according to Equation (5.3). The squares show the average spectral level within each wind speed category, and triangles and diamonds are the spectral levels found in Lemon et al. [32] and Vagle et al. [66] for a frequency of 4.3 kHz and 5 kHz, respectively.

measurement depth and, therefore, an increased volume attenuation of the acoustic signals. However despite the good agreement in absolute spectral level, the presented data clearly show that a single linear model is not sufficient to accurately model the relation between spectral level and wind speed over a wide wind speed range.

Chapter 6

CHARACTERIZING OCEAN AMBIENT NOISE DURING RAIN

In this chapter, ocean ambient noise during rain is analyzed for various rain rates and wind speeds. The detection of rain events using data from the surface rain gauges was described in Section 3.4.1. Only one-minute power spectral density (PSD) estimates corresponding to rain rates of at least 2 mm/h are considered in the analysis[1]. Before evaluating average PSD estimates for various rain rate and wind speed categories (Section 6.2) and describing the dependence of the spectral level on the rain rate and wind speed (Section 6.3), the rain events detected at the surface buoys have to be matched to their corresponding acoustic signature. A respective algorithm will be presented in Section 6.1.

6.1 Offset Correction

During the early stages of the analysis it was discovered that rain events detected at the surface buoys do not exactly match the acoustic pattern measured by the hydrophones, but rather an offset between surface buoy and hydrophone rain events occurs. An example of this is illustrated in the top and middle panel (dashed line) of Figure 6.1. One can see that both the rain rate signal and the acoustic pattern show two distinct peaks, which are, however, not aligned in time. This offset between rain rate and acoustic pattern is thought to be a result of the horizontal displacement between surface buoys and hydrophones (see Figure 3.1b) and the effective surface listening areas of the hydrophones (see Section 3.2). To get an accurate estimation of the sound spectral level associated with different rain rates, the offset is to be estimated and, subsequently, eliminated. To do so, the following algorithm

[1]This avoids the use of PSDs corresponding to negative rain rate samples, which occur especially at the onset and offset of rain events due to inaccuracies in the rain accumulation measurements.

is proposed:

1. Spectrograms for each rain event[2] are computed by dividing the entire noise signal during a rain event into K one-second intervals, computing the spectral estimate $\hat{P}_{0.5}^{\mathrm{WP,1s}}(f,k)$ for the k^{th} interval using the Welch's median method as described in Section 3.3, and then concatenating all $\hat{P}_{0.5}^{\mathrm{WP,1s}}(f,k)$, where k ranges from $-\left\lfloor\frac{K-1}{2}\right\rfloor$ to $\left\lfloor\frac{K-1}{2}\right\rfloor$.

2. The noise power for each spectrogram is computed by

$$P_{\mathrm{noise}}(k) = \sum_{f} 10\,\log_{10}\left(\hat{P}_{0.5}^{\mathrm{WP,1s}}(f,k)\right). \tag{6.1}$$

3. The rain rate signal containing one-minute rain rate samples is interpolated using a univariate spline with a degree of smoothing of three in order to obtain a rain rate signal $\tilde{R}$ that is defined for the same time steps k as P_{noise}.

4. The cross-correlation $(\tilde{R} \star P_{\mathrm{noise}})(k)$ between interpolated rain rate and noise power is computed.

5. The offset between rain rate and associated noise signals in seconds is defined as

$$\mathrm{offset} = \underset{k}{\mathrm{argmax}}\ (\tilde{R} \star P_{\mathrm{noise}})(k). \tag{6.2}$$

Figure 6.1 shows spectrograms, P_{noise}, $\tilde{R}$, and $\tilde{R} \star P_{\mathrm{noise}}$ for rain event 2 from Figure 3.5a. One can observe that as P_{noise} and $\tilde{R}$ have distinct peaks, the cross-correlation function exhibits a distinct maximum with a high correlation value. As the entire noise power is expected to increase with increasing rain rate, rain events with a high maximum rain rate are expected to achieve higher correlation values compared to events exhibiting a lower maximum rain rate, thus, giving more reliable estimates of the offsets. For rain events with lower rain rates

[2] 10 minutes are added before and after each rain event to accurately capture the onset and offset of the event.

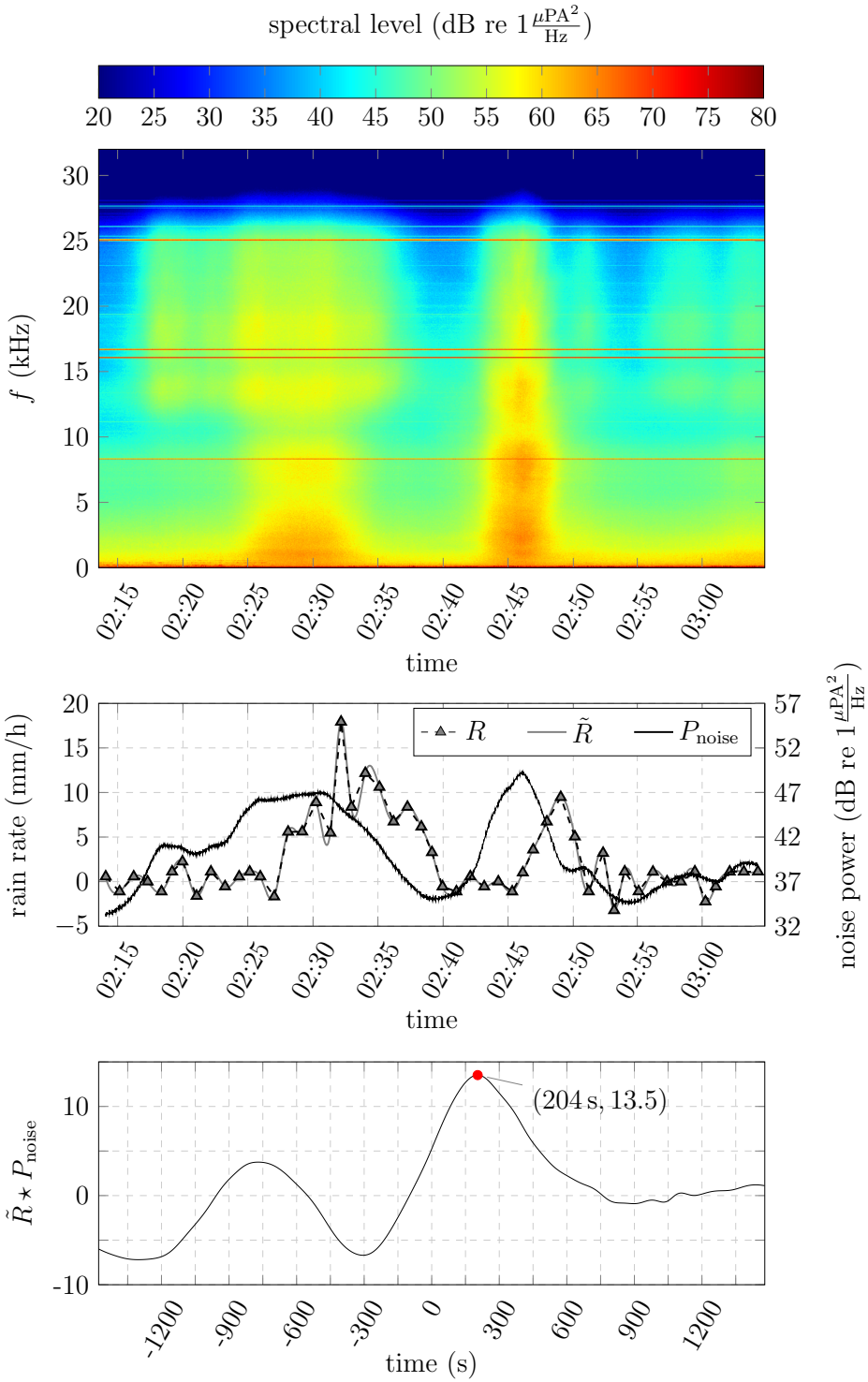

Figure 6.1: Specrogram along with noise power P_{noise}, one-minute rain signal R, interpolated rain signal $\tilde{R}$, and cross-correlation function $\tilde{R} \star P_{\text{noise}}$ for Event 2 shown in Figure 3.5a. The offset is determined according to Equation (6.2). If $\tilde{R}$ and P_{noise} exhibit distinct peaks with high values, $\tilde{R} \star P_{\text{noise}}$ shows also a distinct maximum.

and less structure in terms of $\tilde{R}$ and P_{noise}, the maximum correlation is often low, suggesting that the estimated offset is less likely to represent an actual shift between the rain rate and P_{noise}.

The observed average offset is 195 s (standard deviation 290 s) at the shallow location and 235 s (standard deviation 513 s) at the deep location. This means that most rain events (approximately 62 % at both locations) are first recorded at the hydrophone and afterwards at the surface buoy. Attempts to correlate the offset with wind direction have not revealed any significant relation.

6.2 Frequency Dependency

After determining the offset between rain events detected at the surface buoy and hydrophone, the acoustic signal is shifted by this offset and one-minute PSD estimates for each rain rate and wind speed sample are recomputed. Besides rain events that have been flagged as invalid (see Section 3.3), rain events that have an offset greater than 10 min or that last less than 3 min are also removed from the analysis. Events with offsets greater than 10 min are removed because such large offsets are not considered reasonable and could potentially introduce additional errors in the subsequent analysis. Rain events that last less than 3 min are less likely to be fully developed over the entire surface listening area and are therefore also removed. Afterwards, the PSD estimates are grouped into different rain rate and wind speed categories, whereby the wind speed categories are the same as in Chapter 5 and the rain rate categories are adopted from [34]. The numbers of one-minute PSDs in each category are listed in Table 6.1. Since there are only a few PSD samples available for rain rates above 20 mm/h, the results in those categories should be regarded with greater caution.

Figure 6.2 shows the average PSDs for different rain rates and wind speeds. Furthermore, one quarter of the standard deviation is illustrated by the shaded area around each line. It is noted that multiple narrow band tones, presumably caused by the measurement apparatus,

can be detected in the acoustic signal[3]. Those tones have been removed in Figure 6.2 by linearly interpolating the spectral level over a range of approximately 190 Hz (12 samples) around each tone. The figure shows that the power spectra for each rain rate category significantly depend on the wind speed, particularly at frequencies above 100 Hz. The difference in spectral level between the lowest and highest wind speed usually exceeds 15 dB between 0.5 - 5 kHz at both locations, which is in contrast to the results reported by Ma et al. [34], who found that rain noise spectral levels in the tropical Pacific ocean are almost independent of the prevailing wind speed for frequencies between 1 - 10 kHz. This can likely be attributed to the different measurement locations and depths (Ma's hydrophones were deployed in the tropical Pacific in a depth of 38 m), and implies that rain noise spectral levels cannot be generalized across different locations.

To further analyze the spectral characteristic of rain noise, the spectra are divided into four frequency ranges: 30 - 200 Hz (very low frequency range), 0.2 - 1 kHz (low frequency range), 1 - 10 kHz (medium frequency range), and 10 - 25 kHz (high frequency range). Frequencies below 30 Hz and above 25 kHz are filtered out and, thus, excluded from the analysis.

*6.2.1 Very Low Frequency Range (*30 - 200 Hz*)*

As discussed in Section 5.1, spectral levels below 200 Hz are dominated by noise from distant sources rather than local surface processes such as wind or rain. Therefore, this frequency range is not further regarded in the characterization of noise during rain.

It shall be noted that an anomalous, sharp peak can be observed for the deep hydrophone in the 20 - 30 mm/h rain rate and 0 - 2 m/s wind speed category. It is assumed that malfunctioning devices in the experimental package were responsible for this distortion.

---

[3]At the deep location, six strong tones approximately at 6.27 kHz, 8.34 kHz, 12.53 kHz, 14.03 kHz, 16.09 kHz, and 16.7 kHz were identified. At the shallow location, five tones approximately at 7.45 kHz, 11.17 kHz, 13.28 kHz, 15.31 kHz and 19.38 kHz were identified.

Table 6.1: Number of PSD samples for average spectra shown in Figure 6.2.

	Rain rate (mm/h)				
Wind speed (m/s)	2-5	5-10	10-20	20-30	30-50
	Deep location				
0-2	58	37	8	3	-
2-4	133	68	15	-	-
4-6	378	179	29	2	1
6-8	340	160	42	5	6
8-10	332	132	19	-	3
10-12	209	75	18	1	2
12-14	72	35	5	-	-
>14	138	44	6	1	-
	Shallow location				
0-2	86	47	13	-	2
2-4	342	154	38	9	3
4-6	822	328	109	31	13
6-8	1032	411	115	11	13
8-10	714	322	59	10	5
10-12	467	170	34	2	5
12-14	171	82	21	2	1
>14	109	49	7	1	-

*6.2.2 Low Frequency Range (*0.2 - 1 kHz*)*

In the frequency range between 0.2 - 1 kHz, noise during rain significantly depends on the wind speed. Especially for rain rates below 10 mm/s, the spectral level monotonically increases, typically 1 - 3 dB, with increasing wind speeds at both locations. For rain rates

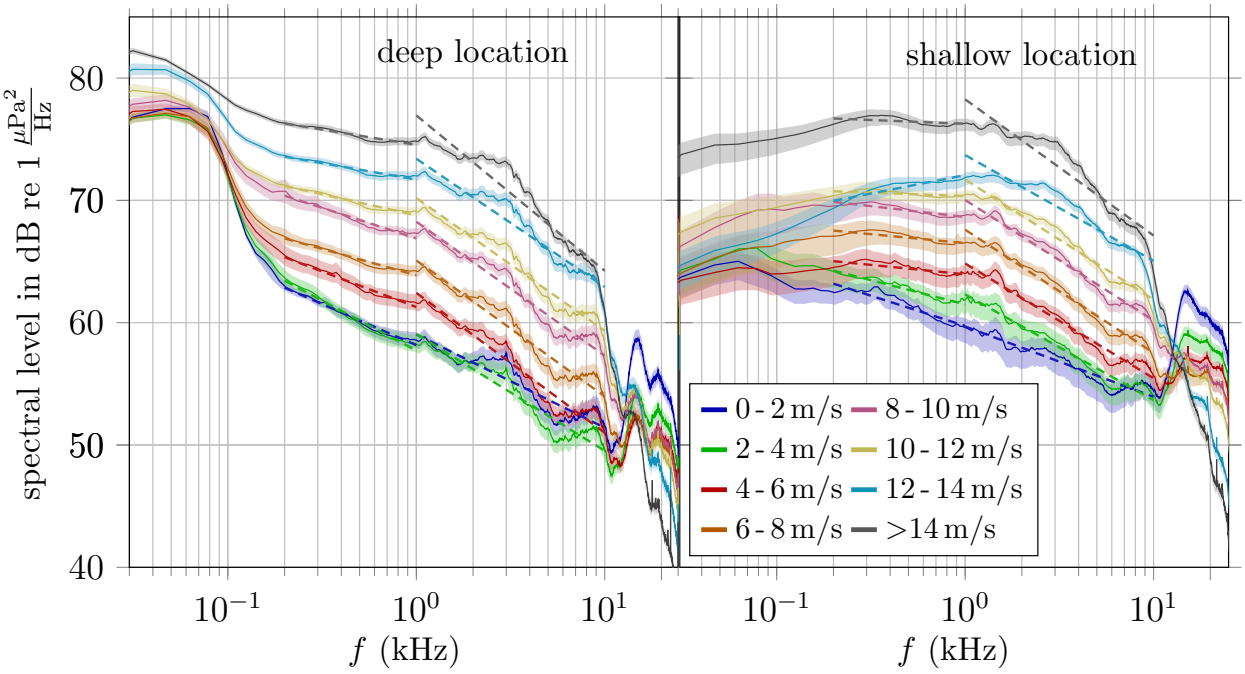

(a) 2 - 5 mm/h rain rate

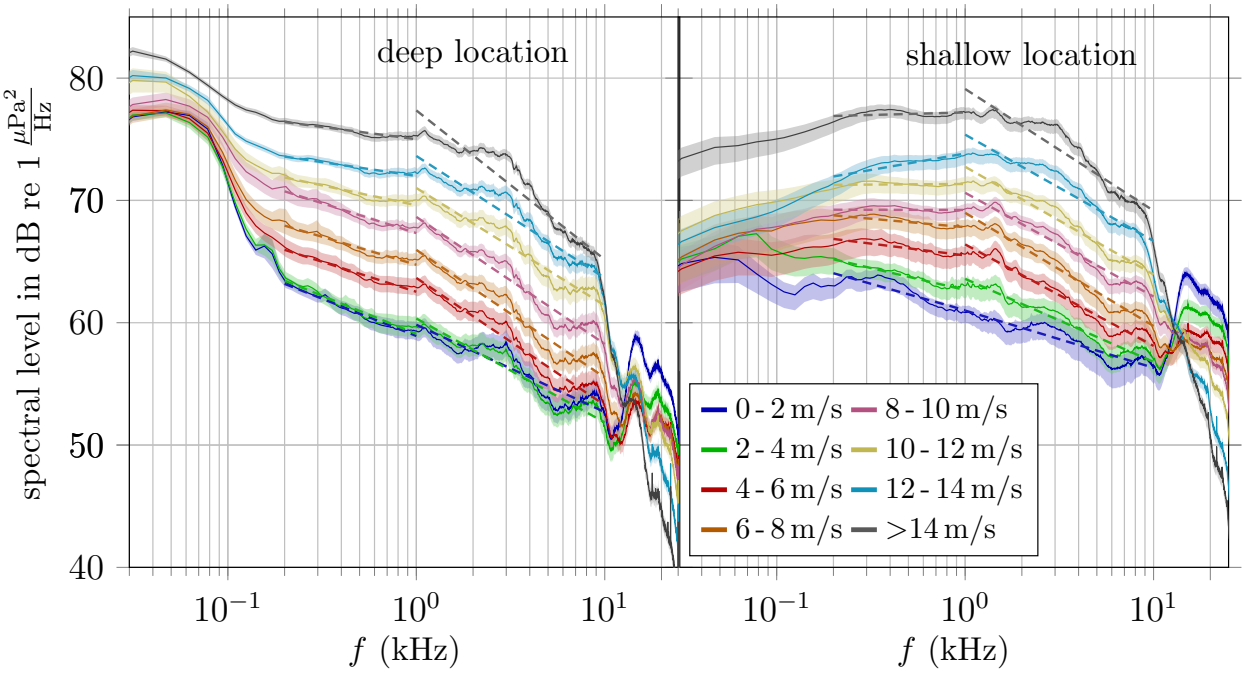

(b) 5 - 10 mm/h rain rate

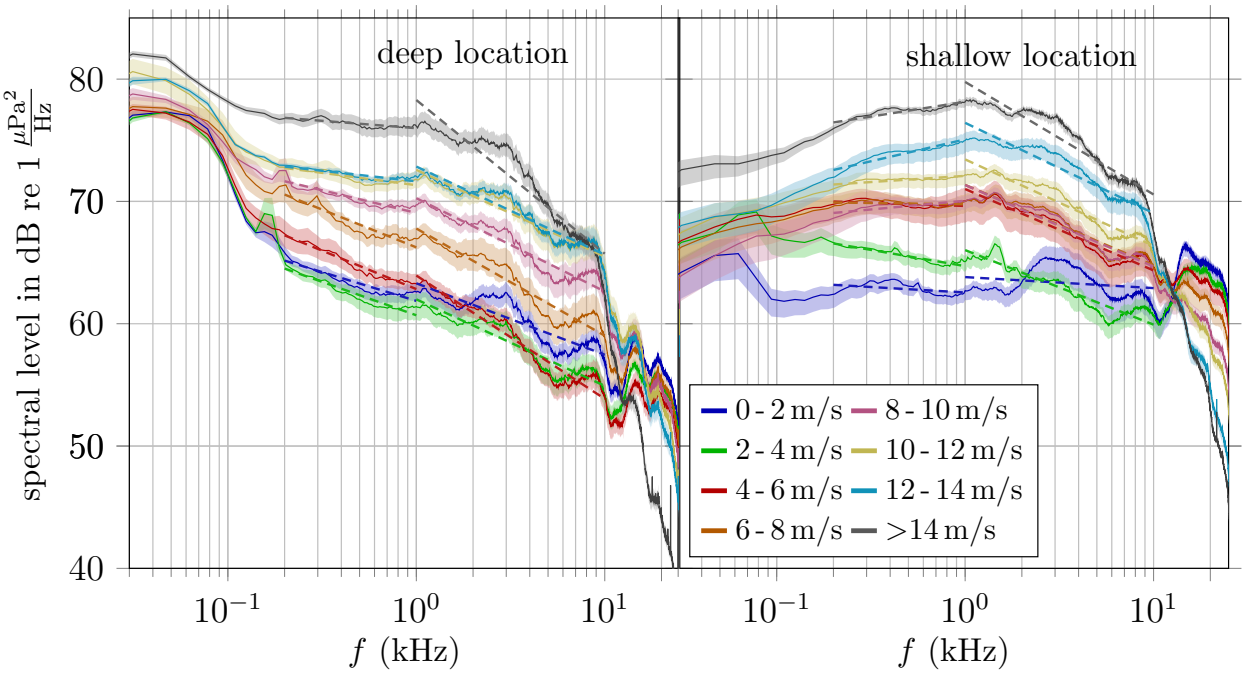

(c) 10 - 20 mm/h rain rate

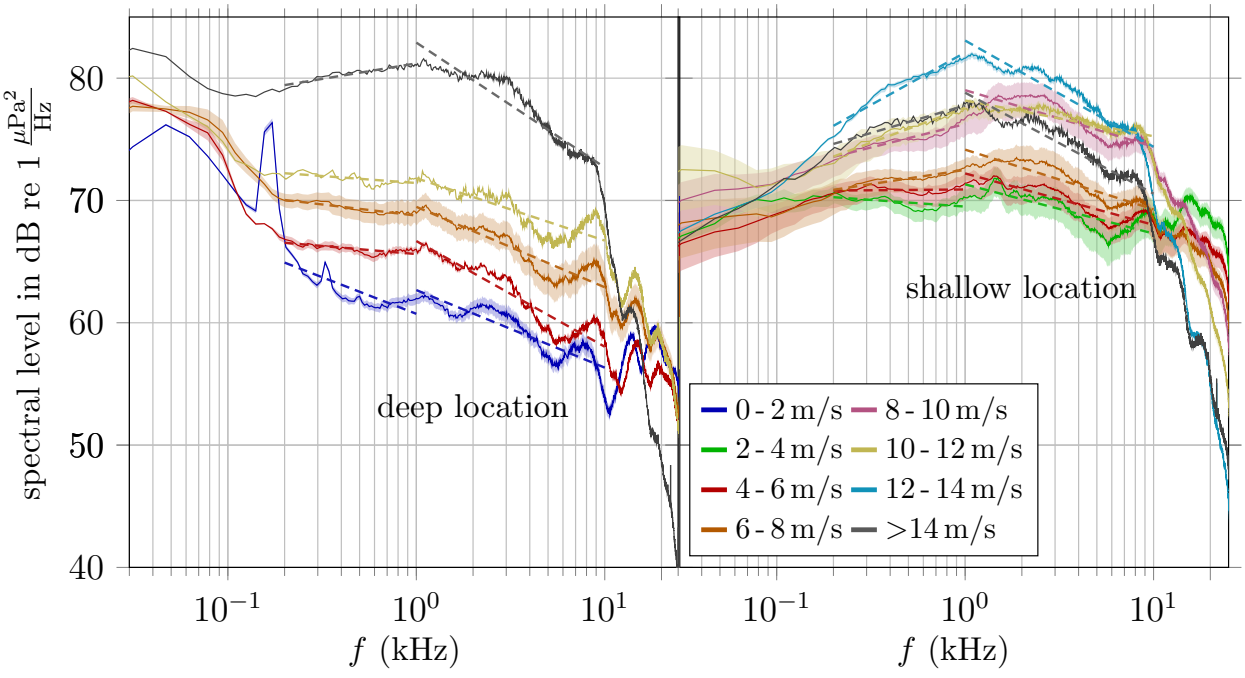

(d) 20 - 30 mm/h rain rate

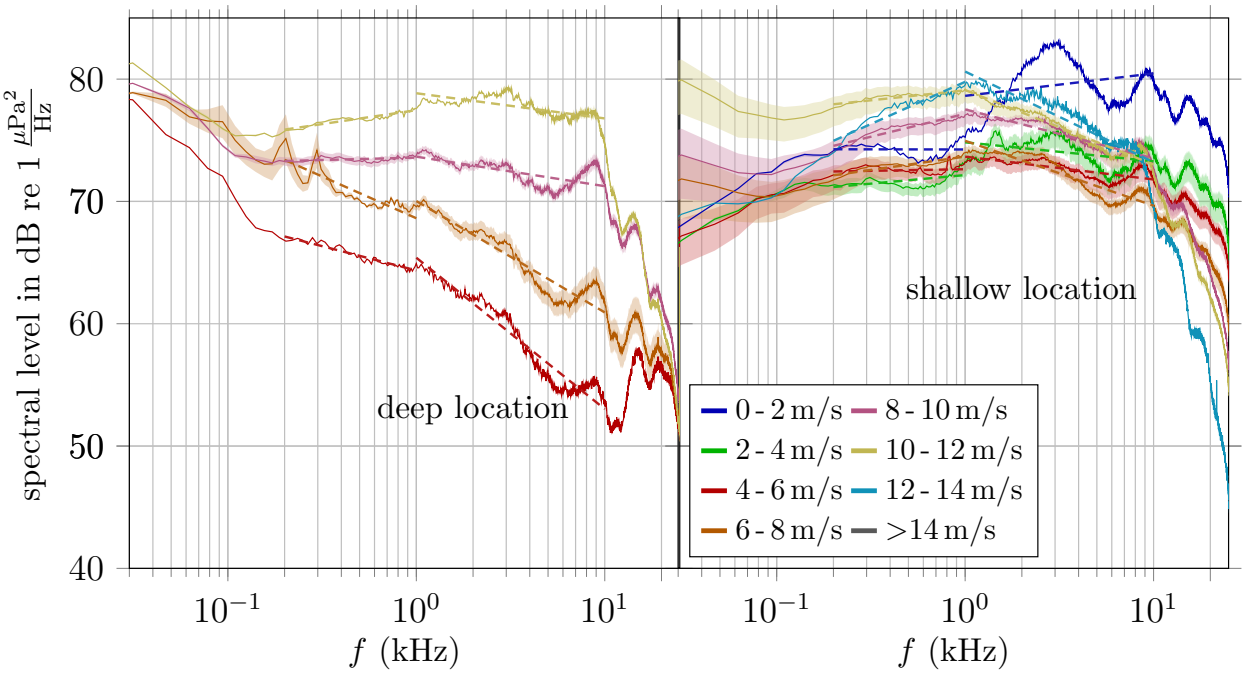

(e) 30 - 50 mm/h rain rate

Figure 6.2: Average power spectral density (PSD) estimates of noise during rain for various rain rates. The shaded areas around each average PSD mark one quarter of the standard deviation. Linear regression results in the low and medium frequency range are shown as dashed lines. The number of PSD samples for each rain rate and wind speed category is given in Table 6.1. Slopes and R^2 scores of the linear regression are provided in Figure 6.3 and 6.4.

above 10 mm/h, this pattern can still be observed, although it is less distinct as average PSDs are usually comprised of fewer PSD samples and, thus, are less likely to represent the true spectral levels for these categories.

The trajectory of the spectral level in the 0.2 - 1 kHz range is modeled by a linear relation

in a logarithmic frequency scale (dashed lines in Figure 6.2)

$$SPL(f) = s \log_{10}(f) + a, \tag{6.3}$$

where SPL is the spectral level in dB re $1\,\mu\text{Pa}^2/\text{Hz}$ averaged over one-third octave bands (median averaging is used to remove outliers), and s and a are the model coefficients. The slopes in dB/oct for all rain rate and wind speed categories are listed in Figure 6.3a. Values that are computed from less than ten PSD samples are marked by an asterisk and should be treated with greater caution as they might not accurately represent the behavior of noise in those categories. For rain rates below 10 mm/h and wind speeds below 4 m/s slopes are between -2.4 and -1.8 dB/octave for the deep, and -1.5 and -1.1 dB/oct for the shallow location, respectively. As rain rate or wind speed increase, the slope becomes more gradual at both locations.

For the deep location, slopes as high as -0.6 dB/oct are observed (rain rate 10 - 20 mm/h and wind speed 10 - 12 m/s; or rain rate 5 - 10 mm/h and wind speed >14 m/s). Although there is a strong indication that the slope further increases with increasing rain rate or increasing wind speed, more samples in those categories are needed to draw such a conclusion. For the shallow location, s becomes positive as the rain rate or wind speed increases. The transition from negative to positive slopes is shown by a diagonal line in Figure 6.3a. All the slopes above this line are negative, whereas the majority of slopes below this line are positive. This pattern is only violated in the >14 m/s wind speed category where the slopes show somewhat smaller values than expected.

Similar to the analysis of wind-only noise in Chapter 5, R^2 scores are used as a metric for evaluating the performance of the regression model. Figure 6.3b shows the R^2 scores of the low frequency linear regression for both shallow and deep location. (R^2 scores are computed using the average spectral levels, often resulting in values closer to 1.) The deep location shows high R^2 scores for rain rates below 10 mm/h, thus, favoring a linear model for those rain rate categories. Lower R^2 scores for rain rates above 10 mm/h are mainly due to a smaller number of PSD samples and, thus, a larger variability in the average PSDs. The

greatest model mismatch can be observed at frequencies around 1 kHz where the spectral levels seem to plateau, as seen in the left plots of Figure 6.2. Overall, a linear model seems to be a good fit to the average PSDs at the low frequency range for the data recorded by the deep hydrophone. The shallow location generally shows lower R^2 scores than the deep location. In the categories where the slope is close to 0, R^2 values are low because the mean predicts the spectral levels well and hence, the linear regression model does not improve the prediction. In the categories where the slope significantly deviates from 0, R^2 values closer to 1 are observed.

6.2.3 Medium Frequency Range (1 - 10 kHz)

Similar to the low frequency range, the spectral level for frequencies between 1 - 10 kHz highly depends on the prevailing wind speed. For rain rates below 10 mm/h, the spectral level at adjacent wind speed bins typically differs by 2 - 3.5 dB at the deep and 1.5 - 3.5 dB at the shallow location, respectively. Like for the low frequency range, the spectral trajectory of the medium frequency range is modeled using the linear relation in Equation (6.3). In this frequency range however, the spectral levels are averaged over one-sixth octave bands instead of one-third octave bands to ensure that there are a sufficient number of bands for the regression. The slopes s and R^2 scores for the 1 - 10 kHz regression model are listed in Figure 6.4.

The spectral levels in this frequency range decrease faster compared to the low frequency range at both locations. The largest decrease is at low rain rates and high wind speeds. The slope becomes more gradual as the rain rate increases or the wind speed decreases. In general, both hydrophones show a similar pattern. However, the absolute values of the slopes at the deep location tend to be slightly larger for most rain rates and wind speeds.

The high R^2 values indicate a strong linear relation for wind speeds below 12 m/s and rain rates below 20 mm/h. Slightly higher R^2 values are observed at the shallow location. Comparing the trajectories of the spectral levels in the 1 - 10 kHz range between the deep and shallow location in Figure 6.2 shows that the deep location exhibits ripples with small

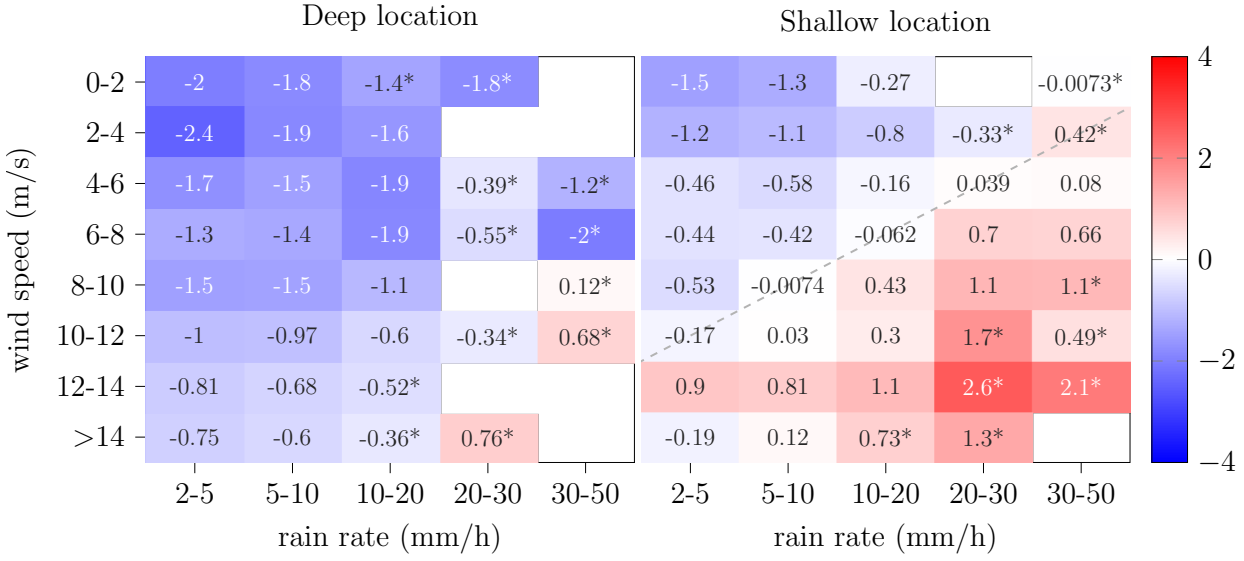

(a) Slope

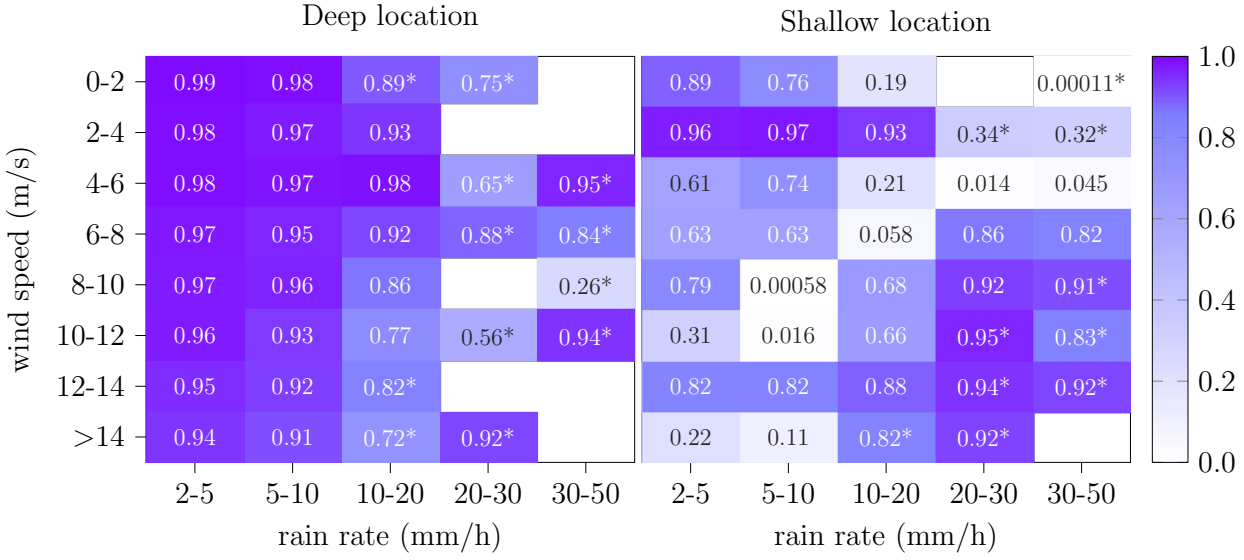

(b) R^2 score

Figure 6.3: (a) Slopes s and (b) R^2 scores of the low frequency (0.2 - 1 kHz) linear regression. Whereas the deep location shows mainly negative slopes, a transition from negative to positive slopes can be observed for the shallow location. The dashed line on the right hand side of (a) marks where the sign of the shallow location slope changes. R^2 scores indicate a strong linear relation for the deep and a slightly weaker linear relation for the shallow location.

local maxima at 3 kHz and 9 kHz, which likely cause a slight drop in the R^2 scores. While those ripples are also observed in some PSDs at the shallow hydrophone, their shape is less pronounced. At wind speeds greater than 12 m/s and rain rates above 20 mm/h, the relation between spectral levels and frequency becomes more non-linear and, hence, the R^2 scores decrease.

It is noted that some unusual behavior can be observed in this frequency range at the shallow location: (1) Small humps between 1 - 2 kHz can be observed in most spectra, especially for rain rates below 20 mm/h. One explanation of their origin are interfering signals from the instrumentation package, but the exact cause is unknown. (2) At the shallow location, there is a very high spectral level around 3 kHz in the 30 - 50 mm/h rain rate and 0 - 2 m/s wind speed category. This behavior might be explained by a hailstorm as the spectral shape matches the pattern of hail reported in [60].

*6.2.4 High Frequency Range (*10 - 25 kHz*)*

The spectral levels for frequencies between 10 - 25 kHz are shown in Figure 6.5. Note that each plot shows the spectral level for a fixed wind speed and various rain rates. At wind speeds below 4 m/s, the spectral levels for light rain and drizzle (rain rates below 20 mm/h) are dominated by a peak around 15 kHz caused by the damped oscillations of microbubbles. These peaks were previously reported in [9, 31, 43, 60, 34]. At higher wind speeds, the spectral levels at all frequencies are increased and cover the peaks. An apparent difference between the deep and shallow location is the smoothness of the spectral level. While the deep location shows many local maxima and minima, the curves for the shallow location are much smoother.

The main challenge in modeling the high frequency range is to find a model that is flexible enough to show the highly non-linear relation of the power spectra, but still allows for some interpretability. Therefore, the following non-linear equation which is inspired by the five

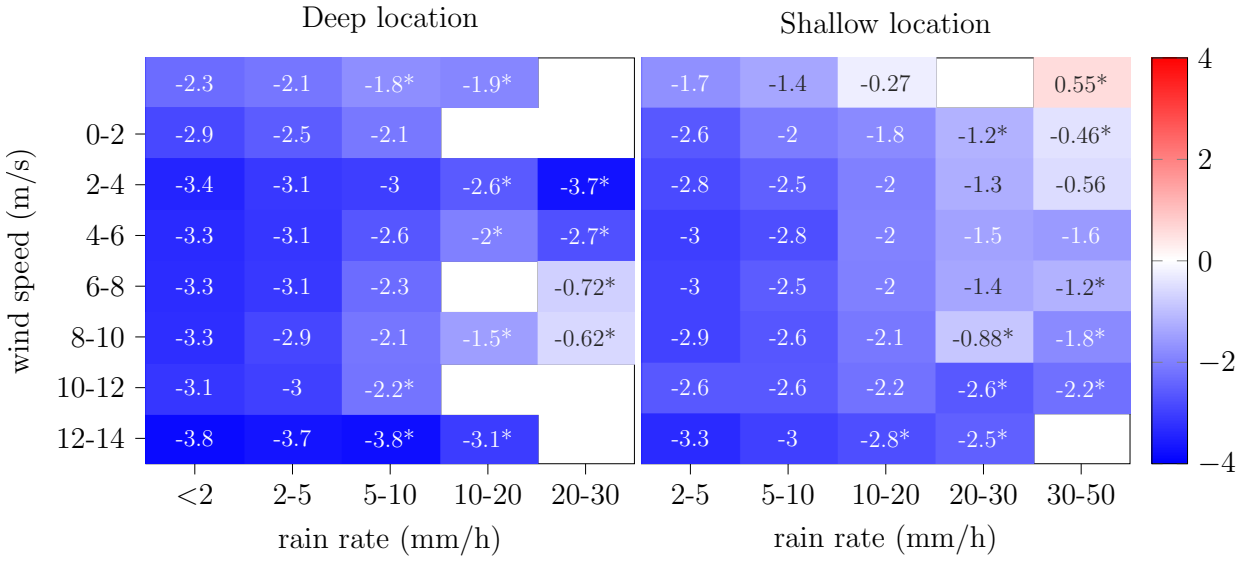

(a) Slope

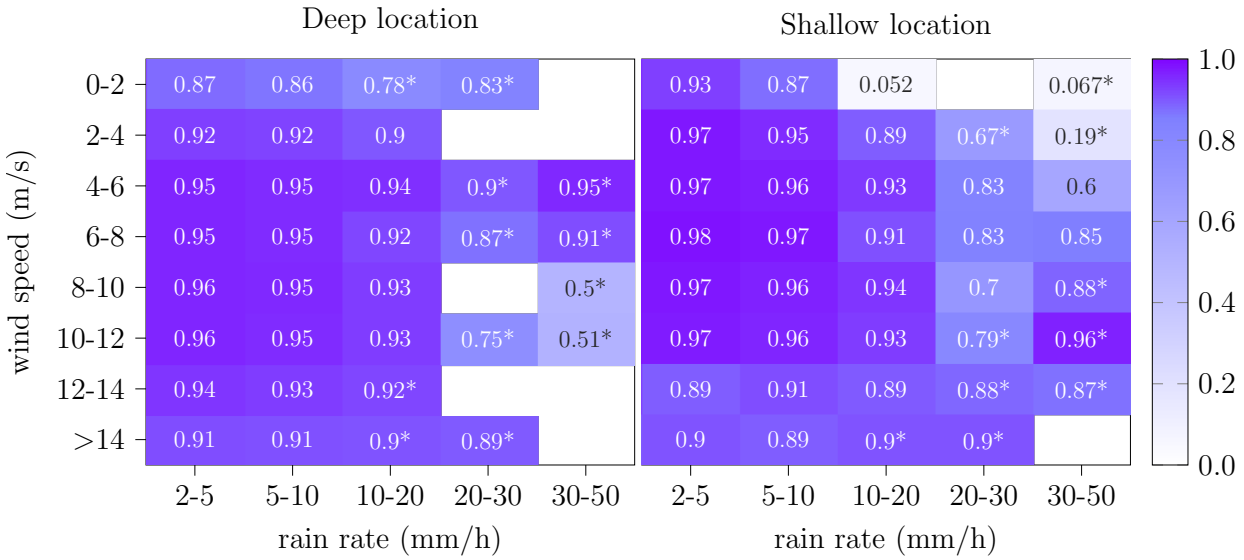

(b) R^2 score

Figure 6.4: (a) Slopes s and (b) R^2 scores of the medium frequency (1 - 10 kHz) linear regression. Steeper slopes compared to the low frequency range can be observed for both locations. The R^2 scores indicate a strong linear relation for wind speeds below 12 m/s.

coefficient model in [34] is proposed:

$$SPL = \frac{A}{\left(1 + \left(\frac{f}{f_{\mathrm{c},h}}\right)^{s_\mathrm{h}}\right) \cdot \left(1 + \left(\frac{f_{\mathrm{c},l}}{f}\right)^{s_\mathrm{l}}\right)}, \tag{6.4}$$

where SPL is the spectral level between 10 - 25 kHz median averaged over one-twelfth octave bands, A is the amplitude, $f_{\mathrm{c},h}$ is the high cutoff frequency, $f_{\mathrm{c},l}$ is the low cutoff frequency, s_h is the high frequency slope, and s_l is the low frequency slope. This model can be viewed as the concatenation of a Butterworth low pass filter with cutoff frequency $f_{\mathrm{c},h}$ and slope s_h and a Butterworth high pass filter with cutoff frequency $f_{\mathrm{c},l}$ and slope s_l. To ensure numerical stability during the optimization procedure, A is first set to 1 and the remaining model coefficients are determined using normalized spectral levels. Afterwards, A is determined using linear least squares. The SciPy function *scipy.optimize.curve_fit* [68] was used to perform the optimization. The model coefficients are given in Table B.1 for both locations and the regression curves are shown as dashed lines in Figure 6.5.

Based on the values in Table B.1 and the plots in Figure 6.5, a few general statements about how the the model coefficients reflect the spectral behavior of the high frequency noise can be made. (1) The amplitude A increases as the spectral level increases. (2) The high cutoff frequency $f_{\mathrm{c},h}$ is larger for the shallow location, whereas the high frequency slope s_h shows similar values for both locations. This causes the spectral level above 20 kHz to decrease more slowly for the shallow location compared to the deep location – a pattern that can also be observed in Figure 6.5. (3) If a strong band pass behavior can be observed in Figure 6.5, the low cutoff frequency $f_{\mathrm{c},l}$ takes values around 7 kHz and slopes s_l of the order of 4 - 6. If no low frequency cutoff can be observed, $f_{\mathrm{c},l}$ assumes smaller values and the slope is around 0 for most wind speeds between 6 - 10 m/s or well above 10 for most wind speeds above 10 m/s.

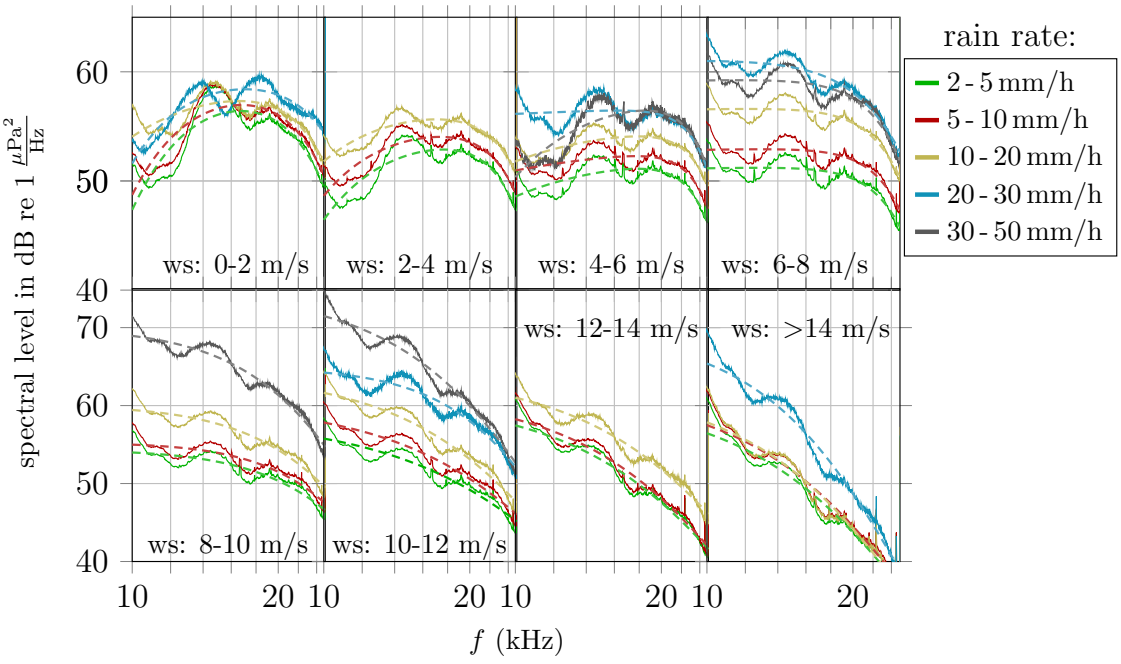

(a) Deep location

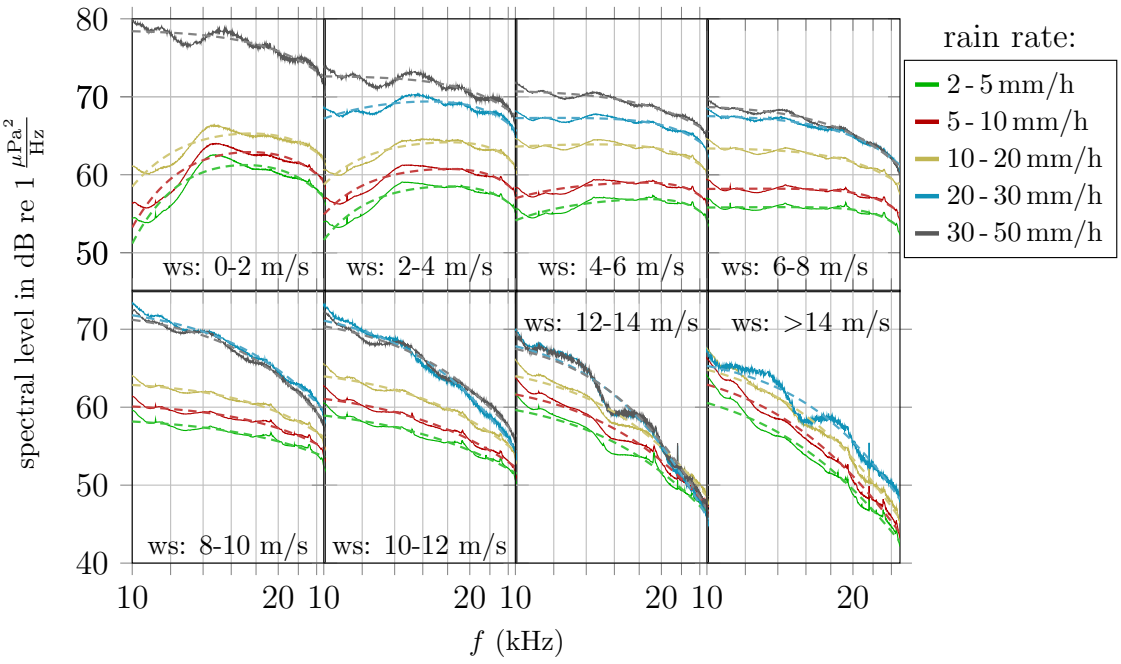

(b) Shallow location

Figure 6.5: Average PSD estimates of noise during rain for (a) deep and (b) shallow location for frequencies between 10 - 25 kHz. The dashed lines show the regression curves according to Equation (6.4). The high frequency range is dominated by a spectral peak around 15 kHz for wind speeds below 4 m/s. For high wind speeds, a steeply decreasing spectral level over frequencies can be observed.

6.2.5 Summary Spectra

To highlight the rain rate dependency of the PSD estimates in Figure 6.2, summary spectra for each location were computed. The results, along with linear regression lines (dashed) are shown in Figure 6.6. The spectra are obtained by averaging over all wind speed categories for a specific rain rate bin. Furthermore, the regression results from Ma et al. [34] (triangle lines) in the 1 - 10 kHz range are plotted for comparison. The main observation is that the spectral level increases with increasing rain rate in both the 0.2 - 1 kHz and 1 - 10 kHz frequency ranges and at both locations. Furthermore, the difference in spectral level between lowest and highest rain rate category increases with increasing frequency.

For frequencies between 0.2 - 1 kHz spectral levels are slowly decreasing for increasing frequencies at the deep location. The slope becomes more gradual as the rain rate increases. Spectral levels at the shallow location are almost constant in this frequency range for rain rates below 20 mm/h. For the two largest rain rate categories however, a slight increase in spectral level over frequencies can be observed. In the 1 - 10 kHz range, both deep and shallow location show a decrease in spectral level over frequencies. In this frequency range, the trajectory of the power spectra is very similar between both locations for rain rates below 20 mm/h. However, the average spectral levels are typically around 1 - 2 dB higher for the shallow location.

Compared to Ma's results, the slopes in this study are steeper for all rain rates at both locations. This can be explained by the different deployment depth of the hydrophone in both studies. Ma used hydrophones in a depth of 20 - 98 m with the majority deployed at 38 m, in contrast to the 581 m (deep) and 81 m (shallow) deployment in this study. The smaller depth causes less volume attenuation especially for higher frequencies, possibly resulting in a more gradual decrease of the spectral level over frequencies. However, Ma also reported significantly lower absolute spectral levels. This can probably be attributed to the different measurement locations, but further research is necessary to confirm that.

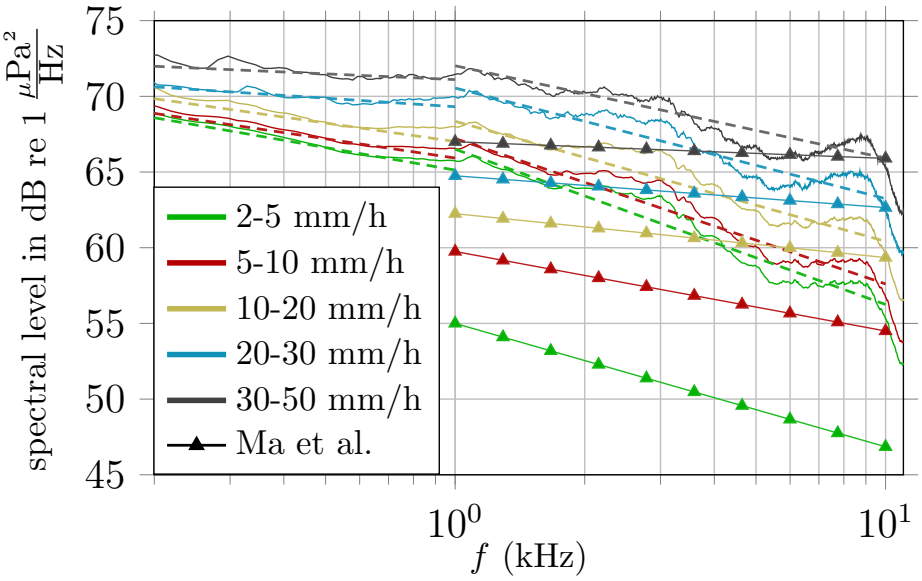

(a) Deep location

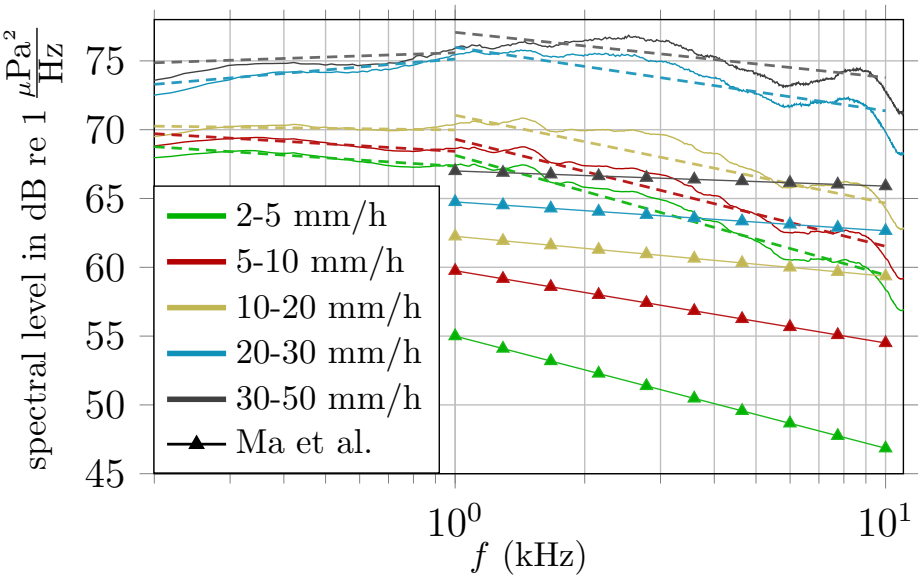

(b) Shallow location

Figure 6.6: Summary spectra for (a) deep and (b) shallow location. The dashed lines are obtained by linear regression of the summary spectra mapped into one-third octave bands (0.2 - 1 kHz frequency range) and one-sixth octave bands (1 - 10 kHz frequency range). The triangle lines are the linear regression results reported by Ma et al. [34]. The spectra from this study differ significantly in level and trajectory from the results reported by Ma.

6.3 Rain Rate and Wind Speed Dependency

6.3.1 Pearson Correlation Coefficient

Equivalently to the analysis in Section 5.2, the spectral levels during rain can be related to the rain rate and wind speed for various frequencies using the Pearson correlation coefficient:

$$r_{SPL,r}(f) = \frac{\sum_{i=1}^{N}(SPL_i(f) - \overline{SPL}(f))(r_i - \bar{r})}{\sqrt{\sum_{i=1}^{N}(SPL_i(f) - \overline{SPL}(f))^2}\sqrt{\sum_{i=1}^{N}(r_i - \bar{r})^2}} \tag{6.5a}$$

$$r_{SPL,v}(f) = \frac{\sum_{i=1}^{N}(SPL_i(f) - \overline{SPL}(f))(v_i - \bar{v})}{\sqrt{\sum_{i=1}^{N}(SPL_i(f) - \overline{SPL}(f))^2}\sqrt{\sum_{i=1}^{N}(v_i - \bar{v})^2}}. \tag{6.5b}$$

SPL_i, r_i, and v_i are the sound spectral level in dB, rain rate in mm/h, and wind speed in m/s of the i^{th} PSD estimate, $\overline{SPL}$, $\bar{r}$, and $\bar{v}$ are their respective sample means, and N is the total number of one-minute PSD estimates. The resulting frequency dependent correlation coefficients are median-averaged over one-third octave bands and shown in Figure 6.7 (dashed lines). In the absence of rain, the dependence on the wind speed is is often modeled using $\log(v)$ instead of v (see Section 2.1 and 5.2). Thus, the solid lines in Figure 6.7b show the Pearson coefficient with v being replaced by $\log(v)$. For the rain rate, the dependence on $\log(r)$ instead of r was also analyzed and the respective correlation is shown in Figure 6.7a.

Figure 6.7a shows that the correlation between spectral level and rain rate increases with frequency until it reaches a maximum of about 0.5 at the shallow and 0.4 at the deep location at 13 kHz. No significant difference between the $\log(r)$ and r model can be observed. The maximum correlation corresponds to the high frequency peak, which is located around 15 kHz and caused by the oscillation of microbubbles that are primarily generated by small rain drops [38]. This is less surprising as most of the data in this study where recorded for rain rates below 20 mm/h (i.e, during light rain and drizzle), where small rain drops are thought to be the main source of underwater noise.

The correlation between spectral level and wind speed shows a similar trajectory as for wind-only noise in Figure 5.3. The main differences to the wind-only data are: (1) During

rain, a steep decrease in correlation occurs for frequencies above 10 kHz. (2) The correlation between spectral level and wind speed is significantly higher at the deep location then at the shallow location. (3) A linear wind speed model is clearly favored over a logarithmic one if rain is present. Especially the first observation is important as it implies that at frequencies around 13 kHz the noise spectral level is essentially independent of the wind speed, but only depends on the rain rate. This has important implications for tasks such as remote sensing of rain rates based on underwater acoustic recordings. If a simple conversion algorithm that relates the sound spectral level at a particular frequency to the prevailing rain rate is to be designed, the sound spectral level is desired to to have a high correlation with the rain rate, but a low correlation with the wind speed. Such an algorithm was developed in [33] for data from the tropical Pacific. The authors used an acoustic frequency of 5 kHz as their spectral levels at this frequency were highly dependent on the rain rate, but approximately independent from the wind speed. For the northeast Pacific data in this study, a frequency of 13 kHz should be chosen instead. However, it is noted that the authors in [33] had more data for high rain rates (>20 mm/h), whereas most acoustic data in this study correspond to rain rates below 20 mm/h. Higher rain rates are associated to larger rain drops, whose impact and bubble sound can contribute significantly to frequencies below 10 kHz [38, 48, 55]. Therefore, spectral levels during heavy rain are likely to show a higher correlation for frequencies below 10 kHz.

An interesting phenomenon can be observed when comparing the correlation curves between both locations. On the one hand, the correlation between spectral level and rain rate is significantly higher at the shallow location. This is consistent with results reported in [3], where the authors have shown that rain rates averaged over a smaller surface area correlate better with acoustic measurement from shallow hydrophones (i.e., that have a smaller effective surface listening area). On the other hand, the correlation between spectral level and wind speed is higher at the deep location. This observation is consistent with the results of the wind-only noise analysis in Section 5.2 indicating that a larger surface listening area improves the correlation with the measured wind speed. Unfortunately it cannot be analyzed

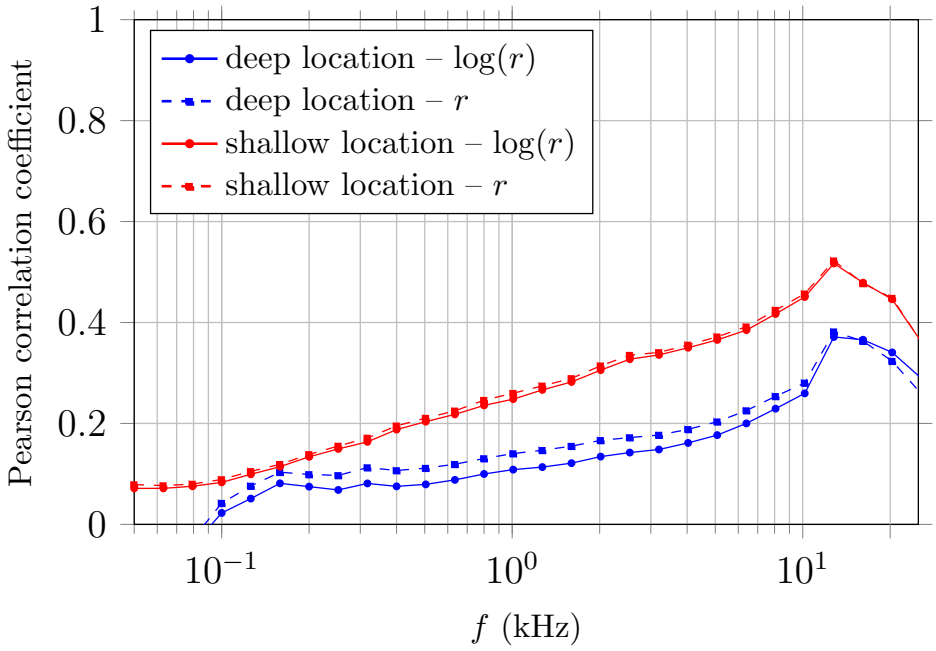

(a) Dependence on rain rate

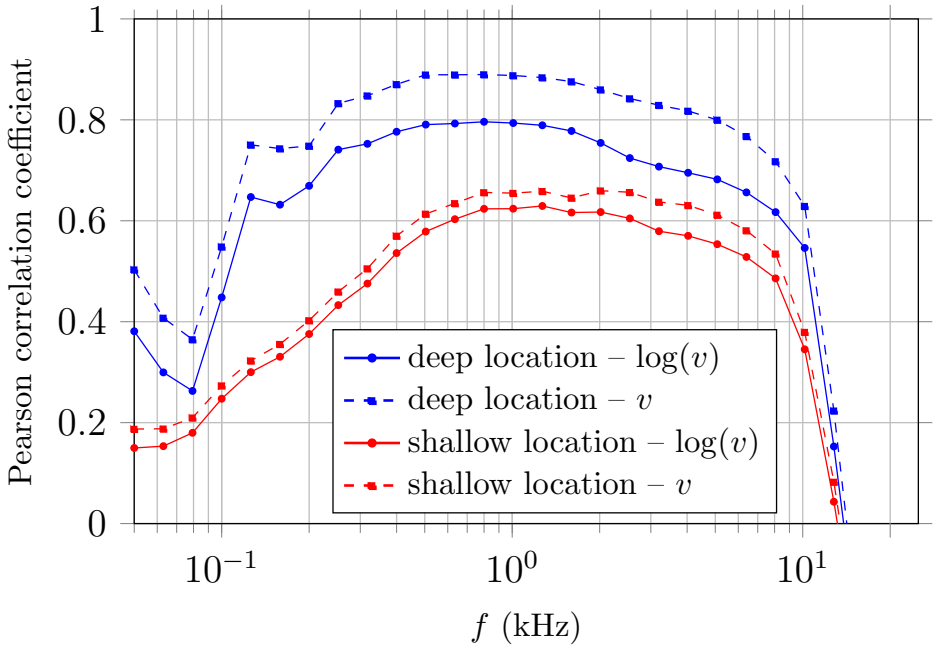

(b) Dependence on wind speed

Figure 6.7: Pearson correlation coefficient according to Equation (6.5) between (a) spectral level and rain rate r and (b) spectral level and wind speed v. For the solid curve, r and v in Equation (6.5) are replaced by $\log(r)$ and $\log(v)$. The correlation is computed for all 2049 frequency bins between 0 - 32 kHz before being median-averaged over one-third octave bands.

how the correlations would change if spatially distributed wind and rain measurements were available. The results in [3], however, indicate that this could improve at least the correlation between spectral level and rain rate.

6.3.2 Linear Model

Based on the observations in Section 6.3.1 the relations between spectral level and rain rate in mm/h as well as spectral level and wind speed in m/s are modeled by the linear equations

$$SPL(r) = s_\mathrm{r}\, r + a_\mathrm{r} \tag{6.6a}$$

$$SPL(v) = s_\mathrm{v}\, v + a_\mathrm{v}, \tag{6.6b}$$

where s_r, s_v, a_r, and a_v are slopes and intercepts of the model. Using two separate linear models, implicitly makes the assumption that rain rate and wind speed are independent of each other. The R^2 scores and slopes of the linear models fitted to the data for each frequency bin and afterwards median averaged over one-third octave bands are shown in Figure 6.8. The R^2 scores show a very similar trajectory to the Pearson coefficients in Figure 6.7, which is less surprising considering that the Pearson coefficient is a measure for linear relation between two random variables. The trajectories of the slopes follow in general the ones of the R^2 scores. At the shallow location, the spectral level versus rain rate slope s_r has a maximum of about 0.5 $\mathrm{dB/mm\,h^{-1}}$ at 10 kHz. At the deep location, s_r has a maximum slope of only 0.3 $\mathrm{dB/mm\,h^{-1}}$ at approximately 12 kHz. On the contrary, the spectral level versus wind speed slopes s_v are largest for frequencies between 2 - 5 kHz. The maximum slopes for the deep and shallow location are about 1.33 and 1.16 $\mathrm{dB/m\,s^{-1}}$, respectively. It is noted that a two wind speed regime model as given in Equation (5.3) has also been analyzed for the relation between spectral level and wind speed. However, the two regime model has shown no significant statistical improvement over the simple linear model, which is why it is not further regarded here.

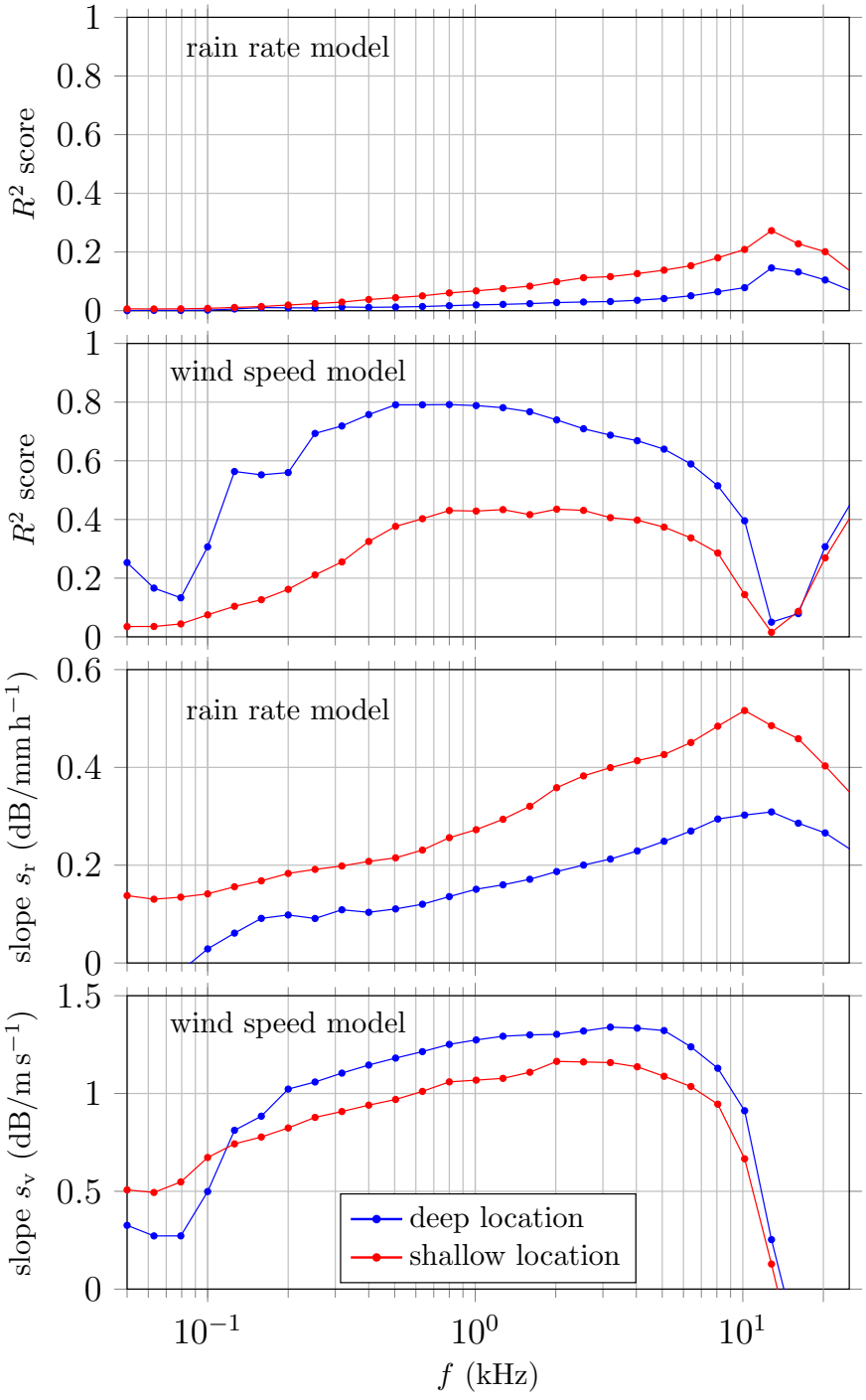

Figure 6.8: R^2 scores and slopes of linear models according to Equation (6.6). Both parameters are computed for all 2049 frequency bins between 0 - 32 kHz before being median-averaged over one-third octave bands.

Examples of the linear models fitted to the data at 13 kHz are shown in Figure 6.9 and 6.10. The average spectral levels of all rain rate and wind speed categories were also computed and are illustrated by triangles in each plot. For the spectral level versus rain rate plots in Figure 6.9, a large variability in the data can be observed. Especially for low rainfall rates, spectral levels likely vary within a 20 dB range at both locations. Nonetheless, an overall increase in spectral level of 0.31 dB/mm h^{-1} at the deep and 0.48 dB/mm h^{-1} at the shallow location can be observed. The linear regression lines in general match well to the average spectral levels in each rain rate category. Only for rain rates above 30 mm/h the model seems to overestimate the observed spectral levels. A possible explanation for this phenomenon is that the impact of small raindrops, which are the main cause of the high frequency peak, on the underwater sound field does not continue to increase with increasing rain rate. Instead the rain drop size distribution might shift to larger rain drops, which have a higher impact on the spectrum below 10 kHz [38, 46]. This suggests that a two rain rate regime model may be necessary to model the spectral level versus rain rate relation over a wide range of rain rates. However, to draw more definite conclusions more data for high rain rates, as well as estimates of the drop size distribution, are necessary.

Figure 6.10 shows that the spectral level at 13 kHz is almost independent of the wind speed, as predicted by the curves in Figure 6.8. Only a slight increase of 0.22 dB/m s^{-1} for the deep and 0.07 dB/m s^{-1} for the shallow location can be observed. Overall, average spectral levels within each wind speed category (triangles) show good agreement with the regression lines. It is interesting to note that the average spectral levels particularly at the deep location show some weak oscillations with increasing wind speed. It is unclear what phenomenon causes this behavior.

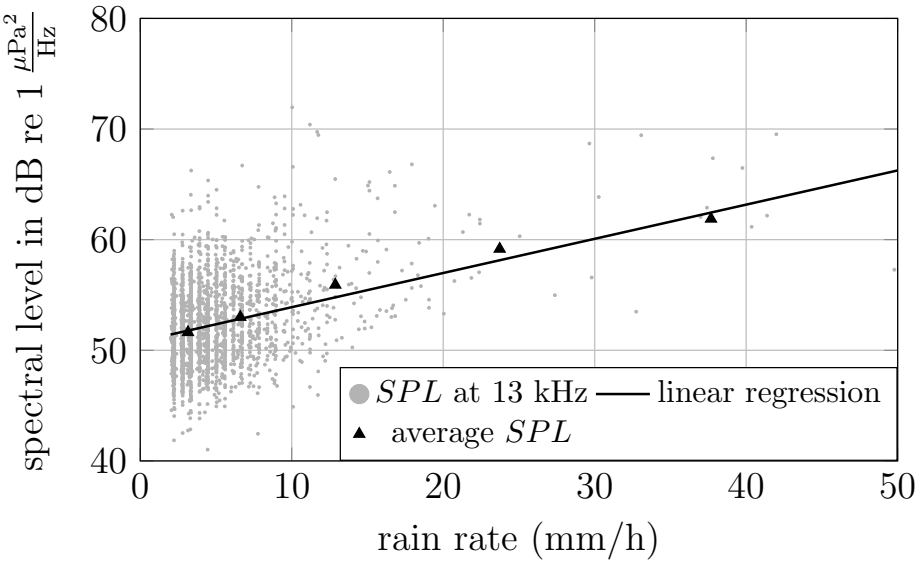

(a) Deep location

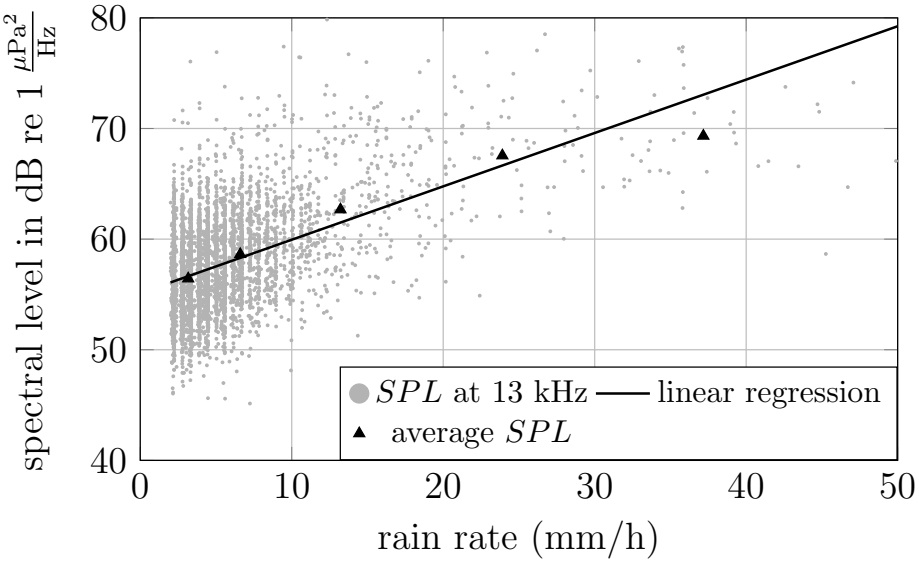

(b) Shallow location

Figure 6.9: Spectral levels (SPL) at 13 kHz versus rain rate for (a) deep and (b) shallow location. The solid lines are obtained by performing linear regression on all data points. The triangles represent average spectral levels and average rain rates in their respective rain rate category. Spectral levels are increasing with an average rate of 0.31 dB/mm h^{-1} for the deep and 0.48 dB/mm h^{-1} for the shallow location.

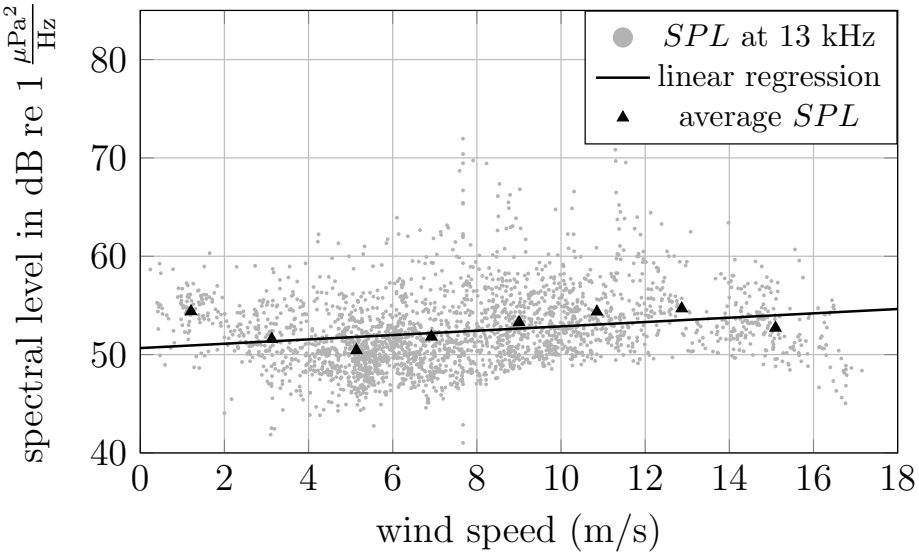

(a) Deep location

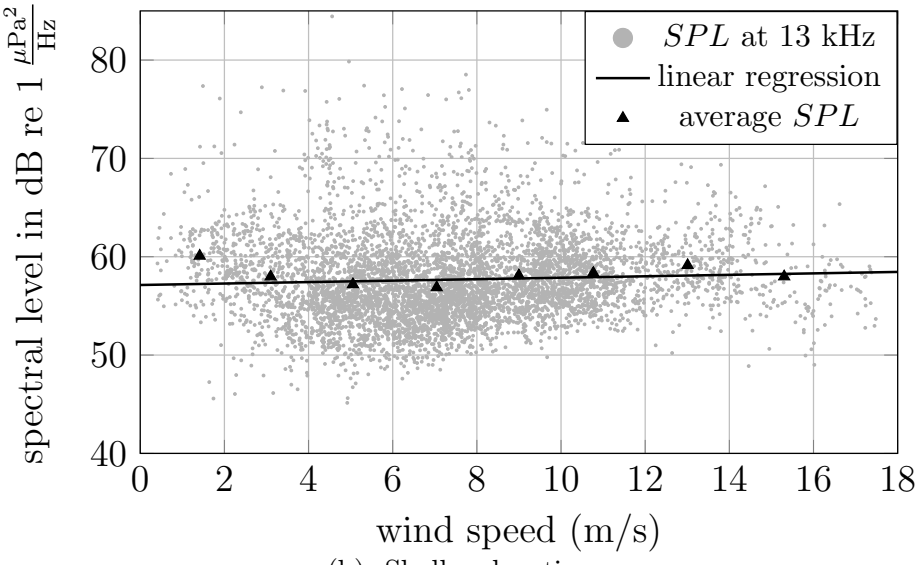

(b) Shallow location

Figure 6.10: Spectral levels (SPL) at 13 kHz versus wind speed for (a) deep and (b) shallow location. The solid line is obtained by performing linear regression on all data points. The triangles represent average spectral levels and average wind speeds in their respective wind speed category. As predicted by Figure 6.8, spectral levels are not significantly increasing with wind speed at this frequency.

Chapter 7

CONCLUSION AND FUTURE WORK

7.1 Conclusion

In this work, acoustic and meteorological data recorded at two locations off the coast of Oregon between December 2015 and June 2019 were evaluated to analyze noise spectral levels from wind and rain at the northeast Pacific continental margin. This data set is of great value as it covers multiple years of broadband acoustic recordings allowing for a detailed statistical analysis of noise spectral levels for various wind speeds and rain rates. To efficiently and accurately estimate the spectral levels, a spectral estimator using sample percentiles was presented and its statistical properties were derived and verified. The main contributions of this work and conclusions drawn from the results are summarized in the following.

Welch percentile estimator:

A spectral estimator that inherits the computational efficiency of the standard Welch estimator, but is more robust against spectral outliers due to short-duration interfering signals was presented in Chapter 4. The spectral estimator is based on a frequency-wise sample percentile estimation over a set of periodograms, hence it is called Welch percentile (WP) estimator. Simple expressions for the statistical properties of the WP estimator were derived from order statistics and verified using simulations with a white Gaussian noise sequence. It was also shown that the 80^{th} percentile estimator has the lowest variance among all WP estimators and therefore also outperforms the popular 50^{th} percentile (median) estimator. The WP estimator is by no means restricted to acoustic signals, but can rather be applied to any stationary random process that is compromised by short-duration interfering signals.

Noise during wind:

Noise spectral levels associated with various wind speeds were analyzed in Chapter 5. It was found that the spectral level above 200 Hz decreases with increasing frequency, however, in contrast to studies conducted in the past (notably [29] and [34]), a single linear model seems not sufficient to model the spectral level versus frequency relation. Instead, two separate linear models, one for frequencies between 0.2 - 3 kHz and one for frequencies between 3 - 25 kHz, were used to model this relation. Using the two linear models, the following key observations about the spectral trajectory were made:

- Spectral levels between 0.2 - 3 kHz decrease on average more gradual then spectral levels above 3 kHz.
- The slopes of the linear model in the 0.2 - 3 kHz range increase with increasing wind speed.
- Above 3 kHz the slopes of the linear model decrease with increasing wind speed at the deep location. This is in contrast to results from previous studies [10, 18, 29, 32, 34, 66, 67, 72], which all report wind-independent slopes. For the shallow location on the other hand, slopes are approximately constant around -13.6 dB/dec for wind speeds up to 10 m/s before decreasing as the wind speed further increases.
- Comparisons with data from the literature show that spectral levels cannot be easily generalized across locations, but rather in-situ long-term measurements are required to accurately characterize wind noise in different oceanic environments.

Furthermore, the dependence of the spectral level on the wind speed was analyzed for various acoustic frequencies. It was found that the highest correlation between spectral level and wind speed is obtained for frequencies between 1 - 10 kHz. The relationship was further modeled by a two wind speed regime linear model in a logarithmic wind speed scale as proposed in the past. The dependence of the model parameters on the acoustic frequency was analyzed in detail. The key observations are as follows:

- The critical wind speed v_c that separates the low wind speed regime from the high

wind speed regime decreases with increasing frequency.

- The spectral level in the low wind speed regime is almost independent of the wind speed, whereas the spectral level in the high wind speed regime increases with a rate of 20 - 32 dB/dec.
- A single wind speed regime as used in many previous studies is not sufficient to accurately model the spectral level versus wind speed relation for the presented data set.

Noise during rain:

Noise spectral levels associated with various rain rates and wind speeds were analyzed in Chapter 6. The spectral trajectory was modeled over different frequency ranges using linear (0.1 - 1 kHz and 1 - 10 kHz range) and non-linear (10 - 25 kHz range) models. The results can be summarized as follows:

- In contrast to previous measurements in [34] (tropical Pacific Ocean), rain noise spectral levels at the northeast Pacific continental margin show a strong wind speed dependency over a broad frequency range.
- Between 0.2 - 1 kHz, the slope of the linear model increases with increasing wind speed or increasing rain rate for both locations. Slopes range from -2.4 to -0.6 dB/oct for the deep and -1.5 to 1.1 dB/oct for the shallow location, respectively.
- Steeper slopes, typically between -2 to -3.5 dB/oct, can be observed in the 1 - 10 kHz range for both locations. Here, slopes become steeper with increasing wind speed and decreasing rain rate.
- The 10 - 25 kHz range can be modeled using a five-coefficient non linear model that captures the spectral peak around 15 kHz caused by light rain and drizzle.

Furthermore, the relation between spectral level and rain rate, as well as spectral level and wind speed was analyzed. The main findings are as follows:

- The highest correlation between spectral level and rain rate occurs at approximately 13 kHz. That is, it coincides with the high frequency peak due to light rain and drizzle.

At the same frequency, the spectral level is approximately independent of the wind speed if rain is present.

- For frequencies below 10 kHz, spectral levels are only weakly dependent on the rain rate but strongly dependent on the wind speed. This is in contrast to the results in [34], which show a strong rain rate and weak wind speed dependence for frequencies between 1 - 10 kHz for data collected in the tropical Pacific Ocean.
- The relation between spectral level and rain rate, as well as spectral level and wind speed were describes by linear models. The maximum slope of the spectral level versus rain rate model is 0.3 dB/mm h^{-1} at the deep location (12 kHz) and 0.5 dB/mm h^{-1} at the shallow location (10 kHz). In contrast to that, the slopes of the spectral level versus wind speed model are largest for frequencies between 2 - 5 kHz with maxima of 1.33 and 1.16 dB/m s^{-1} for the deep and shallow location, respectively.
- The spectral level versus rain rate model fits well to the data for rain rates below 20 mm/h. However, the data indicate that spectral levels do not continue to increase linearly for higher rain rates.

7.2 Suggestions for Future Work

While this work gives a very detailed description of the acoustic environment at the northeast Pacific continental margin during wind and rain, as well as presents a method for efficiently estimating spectral levels of noise signals corrupted by outliers, some open questions and challenges for future work remain:

- The presented WP estimator has to be extended to cases where the percentage of outliers in the data is large but unknown. In those cases, the proposed method can return significantly biased spectral estimates.
- Long-term acoustic and meteorological measurements should be performed in other oceanic environments in order to obtain a better picture on how the spectral behavior of noise during wind and rain varies for different locations.
- Spatially distributed meteorological measurements, as well as acoustic recordings at

various depths should be conducted in order to analyze the effect of the acoustic surface listening area on wind and rain noise measurements.

- The ambient noise analysis during rain should be extended to higher rain rates by collecting more data during heavy rainfall.
- The findings in this study can be used to develop novel algorithms for estimating wind speeds and rain rates from acoustic data. Modern methods from machine learning leveraging the entire spectral structure of the noise instead of performing a simple formulaic conversion at a single frequency bin are promising approaches for that.

BIBLIOGRAPHY

[1] M. Abramowitz and I. Stegun. Psi (digamma) function. In *Handbook of mathematical functions with formulas, graphs, and mathematical tables*, Applied mathematics series (Washington, D.C.); 55, page 258. U.S. Dept. of Commerce : U.S. G.P.O., Washington, D.C., USA, 10th print., with corrections. edition, 1972.

[2] B. Allen, W. G. Anderson, P. R. Brady, D. A. Brown, and J. D. E. Creighton. Findchirp: An algorithm for detection of gravitational waves from inspiraling compact binaries. *Physical Review D*, 85(12), Jun 2012.

[3] M. N. Anagnostou, J. A. Nystuen, E. N. Anagnostou, E. I. Nikolopoulos, and E. Amitai. Evaluation of underwater rainfall measurements during the ionian sea rainfall experiment. *IEEE Transactions on Geoscience and Remote Sensing*, 46(10):2936–2946, 2008.

[4] V. C. Anderson. Variation of the vertical directionality of noise with depth in the north pacific. *The Journal of the Acoustical Society of America*, 66(5):1446–1452, 1979.

[5] R. W. Bannister. Deep sound channel noise from high-latitude winds. *The Journal of the Acoustical Society of America*, 79(1):41–48, 1986.

[6] D. R. Barclay and M. J. Buckingham. The depth-dependence of rain noise in the philippine sea. *The Journal of the Acoustical Society of America*, 133(5):2576–2585, 2013.

[7] J. Berger, J.-R. Bidlot, M. A. Dzieciuch, W. E. Farrell, P. F. Worcester, and R. A. Stephen. A deep ocean acoustic noise floor, 1–800 hz. *The Journal of the Acoustical Society of America*, 143(2):1223–1233, 2018.

[8] P. G. Black, J. R. Proni, J. C. Wilkerson, and C. E. Samsury. Oceanic rainfall detection and classification in tropical and subtropical mesoscale convective systems using underwater acoustic methods. *Monthly Weather Review*, 125(9):2014 – 2042, 1997.

[9] N. Bom. Effect of rain on underwater noise level. *The Journal of the Acoustical Society of America*, 45(1):150–156, 1969.

[10] S. L. Bourassa. Measurement of oceanic wind speed using acoustic ambient sea noise. Master's thesis, University of Rhode Island, 1984.

[11] A. S. Burgess and D. J. Kewley. Wind-generated surface noise source levels in deep water east of australia. *The Journal of the Acoustical Society of America*, 73(1):201–210, 1983.

[12] P. Cauchy, K. J. Heywood, N. D. Merchant, B. Y. Queste, and P. Testor. Wind speed measured from underwater gliders using passive acoustics. *Journal of Atmospheric and Oceanic Technology*, 35(12):2305 – 2321, 2018.

[13] N. R. Chapman and J. W. Cornish. Wind dependence of deep ocean ambient noise at low frequencies. *The Journal of the Acoustical Society of America*, 93(2):782–789, 1993.

[14] C. Chen and F. J. Millero. Speed of sound in seawater at high pressures. *The Journal of the Acoustical Society of America*, 62(5):1129–1135, 1977.

[15] W. W. Crouch and P. J. Burt. The logarithmic dependence of surface-generated ambient-sea-noise spectrum level on wind speed. *The Journal of the Acoustical Society of America*, 51(3B):1066–1072, 1972.

[16] K. R. Curtis, B. M. Howe, and J. A. Mercer. Low-frequency ambient sound in the north pacific: Long time series observations. *The Journal of the Acoustical Society of America*, 106(6):3189–3200, 1999.

[17] H. A. David and H. N. Nagaraja. Distribution of a single order statistic. In *Order Statistics*, pages 9–11. Wiley, 3rd edition, 2004.

[18] D. L. Evans, D. R. Watts, D. Halpern, and S. Bourassa. Oceanic winds measured from the seafloor. *Journal of Geophysical Research: Oceans*, 89(C3):3457–3461, 1984.

[19] D. M. Farmer and D. D. Lemon. The influence of bubbles on ambient noise in the ocean at high wind speeds. *Journal of Physical Oceanography*, 14(11):1762–1778, 1984.

[20] M. Farrokhrooz, K. E. Wage, M. A. Dzieciuch, and P. F. Worcester. Vertical line array measurements of ambient noise in the north pacific. *The Journal of the Acoustical Society of America*, 141(3):1571–1581, 2017.

[21] G. J. Franz. Splashes as sources of sound in liquids. *The Journal of the Acoustical Society of America*, 31(8):1080–1096, 1959.

[22] J. Gareth, D. Witten, T. Hastie, and R. Tibshirani. *An Introduction to Statistical Learning*. Springer, New York, NY, 2013.

[23] E. L. Hamilton. Compressional-wave attenuation in marine sediments. *GEOPHYSICS*, 37(4):620–646, 1972.

[24] E. L. Hamilton. Geoacoustic modeling of the sea floor. *The Journal of the Acoustical Society of America*, 68(5):1313–1340, 1980.

[25] J. T. Kees, J. M. Ernst, W. C. Headley, and A. A. Louis Beex. Robust blind spectral estimation in the presence of non-gaussian noise. In *MILCOM 2017 - 2017 IEEE Military Communications Conference (MILCOM)*, pages 629–634, Baltimore, MD, USA, 2017.

[26] M. G. Kendall, A. Stuart, J. K. Ord, S. F. Arnold, and A. O'Hagan. Standard errors of quantiles. In *Kendall's advanced theory of statistics*, Kendall's library of statistics, pages 356–358. Edward Arnold, London, UK, 6th edition, 1994.

[27] B. R. Kerman. Underwater sound generation by breaking wind waves. *The Journal of the Acoustical Society of America*, 75(1):149–165, 1984.

[28] D. J. Kewley, D. G. Browning, and W. M. Carey. Low-frequency wind-generated ambient noise source levels. *The Journal of the Acoustical Society of America*, 88(4):1894–1902, 1990.

[29] V. O. Knudsen, R. S. Alford, and J. W. Emling. Underwater ambient noise. *Journal of Marine Research*, 7(3):410–429, 1948.

[30] W. A. Kuperman. Propagation effects associated with ambient noise. In B. R. Kerman, editor, *Sea Surface Sound: Natural Mechanisms of Sourface Generated Noise in the Ocean*, volume 238 of *NATO ASI Series (Series C: Mathematical and Physical Sciences)*, pages 403–415. Kluwer Academic Publishers, Boston, MA, USA, 1988.

[31] F. Laville, G. D. Abbott, and M. J. Miller. Underwater sound generation by rainfall. *The Journal of the Acoustical Society of America*, 89(2):715–721, 1991.

[32] D. D. Lemon, D. M. Farmer, and D. R. Watts. Acoustic measurements of wind speed and precipitation over a continental shelf. *Journal of Geophysical Research: Oceans*, 89(C3):3462–3472, 1984.

[33] B. B. Ma and J. A. Nystuen. Passive acoustic detection and measurement of rainfall at sea. *Journal of Atmospheric and Oceanic Technology*, 22(8):1225–1248, 2005.

[34] B. B. Ma, J. A. Nystuen, and R.-C. Lien. Prediction of underwater sound levels from rain and wind. *The Journal of the Acoustical Society of America*, 117(6):3555–3565, 2005.

[35] R. A. Maronna, R. Martin, V. J. Yohai, and M. Salibián-Barrera. *Robust Statistics, 2nd Edition*. Wiley, 2nd edition, 2019.

[36] M. F. McKenna, D. Ross, S. M. Wiggins, and J. A. Hildebrand. Underwater radiated noise from modern commercial ships. *The Journal of the Acoustical Society of America*, 131(1):92–103, 2012.

[37] H. Medwin, A. Kurgan, and J. A. Nystuen. Impact and bubble sound from raindrops at normal and oblique incidence. *The Journal of the Acoustical Society of America*, 88(1):413–418, 1990.

[38] H. Medwin, J. A. Nystuen, P. W. Jacobus, L. H. Ostwald, and D. E. Snyder. The anatomy of underwater rain noise. *The Journal of the Acoustical Society of America*, 92(3):1613–1623, 1992.

[39] N. D. Merchant, P. Blondel, D. T. Dakin, and J. Dorocicz. Averaging underwater noise levels for environmental assessment of shipping. *The Journal of the Acoustical Society of America*, 132(4):EL343–EL349, 2012.

[40] E. C. Monahan. Oceanic Whitecaps. *Journal of Physical Oceanography*, 1(2):139–144, 04 1971.

[41] E. C. Monahan and M. Lu. Acoustically relevant bubble assemblages and their dependence on meteorological parameters. *IEEE Journal of Oceanic Engineering*, 15(4):340–349, 1990.

[42] A. H. Nuttail. Spectral estimation by means of overlapped fast fourier transform processing of windowed data. Technical Report 4169, NUSC, New London, CT, USA, 1971.

[43] J. A. Nystuen. Rainfall measurements using underwater ambient noise. *The Journal of the Acoustical Society of America*, 79(4):972–982, 1986.

[44] J. A. Nystuen. Acoustical rainfall analysis: Rainfall drop size distribution using the underwater sound field. *Journal of Atmospheric and Oceanic Technology*, 13(1):74–84, 1996.

[45] J. A. Nystuen. Relative performance of automatic rain gauges under different rainfall conditions. *Journal of Atmospheric and Oceanic Technology*, 16(8):1025–1043, 1999.

[46] J. A. Nystuen. Listening to raindrops from underwater: An acoustic disdrometer. *Journal of Atmospheric and Oceanic Technology*, 18(10):1640–1657, 2001.

[47] J. A. Nystuen, C. C. McGlothin, and M. S. Cook. The underwater sound generated by heavy rainfall. *The Journal of the Acoustical Society of America*, 93(6):3169–3177, 1993.

[48] J. A. Nystuen and H. Medwin. Underwater sound produced by rainfall: Secondary splashes of aerosols. *The Journal of the Acoustical Society of America*, 97(3):1606–1613, 1995.

[49] J. A. Nystuen, J. R. Proni, P. G. Black, and J. C. Wilkerson. A comparison of automatic rain gauges. *Journal of Atmospheric and Oceanic Technology*, 13(1):62–73, 1996.

[50] S. E. Parks, I. Urazghildiiev, and C. W. Clark. Variability in ambient noise levels and call parameters of north atlantic right whales in three habitat areas. *The Journal of the Acoustical Society of America*, 125(2):1230–1239, 2009.

[51] E. Parzen. Nonparametric statistical data modeling. *Journal of the American Statistical Association*, 74(365):105–121, 1979.

[52] D. B. Percival and A. T. Walden. *Spectral Analysis for Univariate Time Series*. Cambridge Series in Statistical and Probabilistic Mathematics. Cambridge University Press, Cambridge, UK, 2020.

[53] C. L. Piggott. Ambient sea noise at low frequencies in shallow water of the scotian shelf. *The Journal of the Acoustical Society of America*, 36(11):2152–2163, 1964.

[54] M. B. Porter. Bellhop3d user guide. Technical report, San Diego, CA, USA, 2016.

[55] H. C. Pumphrey, L. A. Crum, and L. Bjo/rno/. Underwater sound produced by individual drop impacts and rainfall. *The Journal of the Acoustical Society of America*, 85(4):1518–1526, 1989.

[56] S. C. Riser, J. Nystuen, and A. Rogers. Monsoon effects in the bay of bengal inferred from profiling float-based measurements of wind speed and rainfall. *Limnology and Oceanography*, 53(5part2):2080–2093, 2008.

[57] W. B. F. Ryan, S. M. Carbotte, J. O. Coplan, S. O'Hara, A. Melkonian, R. Arko, R. A. Weissel, V. Ferrini, A. Goodwillie, F. Nitsche, J. Bonczkowski, and R. Zemsky. Global multi-resolution topography (gmrt) synthesis data set. *Geochemistry, Geophysics, Geosystems*, 10(3), 2009. data doi: 10.1594/IEDA.0001000.

[58] F. Schwock and S. Abadi. Statistical properties of a modified welch method that uses sample percentiles. 2020. arXiv:2010.11444.

[59] F. Schwock, J. Ragland, M. Munson, and S. Abadi. OOIPy: A Python toolbox designed to aid in the scientific analysis of Ocean Observatories Initiative (OOI) data, 11 2020.

[60] J. A. Scrimger, D. J. Evans, G. A. McBean, D. M. Farmer, and B. R. Kerman. Underwater noise due to rain, hail, and snow. *The Journal of the Acoustical Society of America*, 81(1):79–86, 1987.

[61] J. A. Scrimger, D. J. Evans, and W. Yee. Underwater noise due to rain—open ocean measurements. *The Journal of the Acoustical Society of America*, 85(2):726–731, 1989.

[62] P. Shaw, D. Watts, and H. Rossby. On the estimation of oceanic wind speed and stress from ambient noise measurements. *Deep Sea Research*, 25(12):1225 – 1233, 1978.

[63] J. A. Shooter and M. L. Gentry. Wind generated noise in the parece vela basin. *The Journal of the Acoustical Society of America*, 70(6):1757–1761, 1981.

[64] R. J. Urick. *Principles of underwater sound*. McGraw-Hill, New York, NY, USA, 3rd ed. edition, 1983.

[65] R. J. Urick. Ambient noise in the sea. Technical report, Washington, D.C., USA, 1984.

[66] S. Vagle, W. G. Large, and D. M. Farmer. An evaluation of the wotan technique of inferring oceanic winds from underwater ambient sound. *Journal of Atmospheric and Oceanic Technology*, 7(4):576–595, 1990.

[67] R. Vakkayil, H. C. Graber, and W. G. Large. Oceanic winds estimated from underwater ambient noise observations in swade. In *OCEANS 96 MTS/IEEE Conference Proceedings. The Coastal Ocean - Prospects for the 21st Century*, volume 1, pages 45–51 vol.1, 1996.

[68] P. Virtanen, R. Gommers, T. E. Oliphant, M. Haberland, T. Reddy, D. Cournapeau, E. Burovski, P. Peterson, W. Weckesser, J. Bright, S. J. van der Walt, M. Brett, J. Wilson, K. J. Millman, N. Mayorov, A. R. J. Nelson, E. Jones, R. Kern, E. Larson, C. J. Carey, İ. Polat, Y. Feng, E. W. Moore, J. VanderPlas, D. Laxalde, J. Perktold, R. Cimrman, I. Henriksen, E. A. Quintero, C. R. Harris, A. M. Archibald, A. H. Ribeiro, F. Pedregosa, P. van Mulbregt, and SciPy 1.0 Contributors. SciPy 1.0: Fundamental Algorithms for Scientific Computing in Python. *Nature Methods*, 17:261–272, 2020.

[69] R. A. Wagstaff. Low-frequency ambient noise in the deep sound channel—the missing component. *The Journal of the Acoustical Society of America*, 69(4):1009–1014, 1981.

[70] R. Wanninkhof. Relationship between wind speed and gas exchange over the ocean revisited. *Limnology and Oceanography: Methods*, 12(6):351–362, 2014.

[71] P. Welch. The use of fast fourier transform for the estimation of power spectra: A method based on time averaging over short, modified periodograms. *IEEE Transactions on Audio and Electroacoustics*, 15(2):70–73, 1967.

[72] G. M. Wenz. Acoustic ambient noise in the ocean: Spectra and sources. *The Journal of the Acoustical Society of America*, 34(12):1936–1956, 1962.

Appendix A

DERIVATION OF STATISTICAL PROPERTIES OF WELCH PERCENTILE ESTIMATOR

A.1 Distribution

The statistical properties of the WP estimator can be derived from the order statistics $\{\hat{P}_{(1)}, \ldots, \hat{P}_{(K)}\}$ of the modified periodograms. Here, it is assumed that the $\hat{P}_i$'s are independent and identically distributed[1]. It is well known (for example, see [52, p. 224-225]) that for a proper window and large enough N_s the distribution of $\hat{P}_i$ is given by

$$\hat{P}_i \overset{\mathrm{d}}{=} \frac{P}{2}\chi_2^2 \quad \text{for} \quad 0 < f_j < \frac{f_s}{2} \tag{A.1}$$

where χ_2^2 is the chi-square distribution with two degrees of freedom and probability density function (PDF)

$$f(u) = \begin{cases} \frac{1}{2}\mathrm{e}^{-u/2}, & u \geq 0 \\ 0, & u < 0 \end{cases}. \tag{A.2}$$

According to [17], the PDF $f_{(i)}(x)$ of the i^{th} order statistic $\hat{P}_{(i)}$ is given by

$$f_{(i)}(x) = \frac{1}{\mathrm{B}(i, K-i+1)} F^{i-1}(x)\,(1-F(x))^{K-i}\,f(x), \tag{A.3}$$

where $F(x)$ is the cumulative distribution function of $\hat{P}_i$ and can be obtained by integrating Equation (A.2) from 0 to x. $\mathrm{B}(\alpha, \beta)$ is the beta function defined by

$$\mathrm{B}(\alpha, \beta) = \int_0^1 t^{\alpha-1}\,(1-t)^{\beta-1}\,\mathrm{d}t. \tag{A.4}$$

---

[1]The independence condition holds if adjacent data segments do not overlap, or a moderate overlap along with a proper data taper is used.

Equation (A.3) can now be used to derive expressions for bias and variance of the WP estimator.

A.2 Bias

Following the procedure in [2], bias expressions for an arbitrary quantile and sample size can be derived. To do so, $\alpha = K - i$, $\beta = i - 1$, and $t = 1 - F(x)$ are first substituted in Equation (A.3) and the expected value of $\hat{Q}(q)$ is computed. It is also assumed that $\hat{Q}(q) \approx \hat{P}_{(i)}$ for some $i = 1, \ldots, K$. While this, in general, does not reflect the WP estimator defined in Equation (4.1) and (4.2), it was found that this approximation provides good results for the estimator's statistical properties. The resulting $\mathbb{E}\{\hat{Q}(q)\}$ is given in Equation (A.5).

$$\mathbb{E}\{\hat{Q}(q)\} \approx -\frac{P}{\mathrm{B}(\alpha+1,\beta+1)} \int_0^1 t^\alpha (1-t)^\beta \ln(t) \mathrm{d}t. \tag{A.5}$$

Here, I have used the fact that $\mathrm{d}t = -f(x)\mathrm{d}x$ and $x = -P\ln(1-F(x)) = -P\ln(t)$ for the chi-square distribution with 2 degrees of freedom. By noting that

$$\frac{\partial t^\alpha (1-t)^\beta}{\partial \alpha} = t^\alpha (1-t)^\beta \ln(t), \tag{A.6}$$

Equation A.5 can be written as

$$\mathbb{E}\{\hat{Q}(q)\} = -\frac{P}{\mathrm{B}(\alpha+1,\beta+1)} \frac{\partial}{\partial \alpha} \mathrm{B}(\alpha+1,\beta+1). \tag{A.7}$$

Using the digamma function ψ to express the partial derivative of the beta function[2], Equation (A.7) can be simplified to

$$\mathbb{E}\{\hat{Q}(q)\} = P\left[\psi(\alpha+\beta+2) - \psi(\alpha+1)\right]. \tag{A.8}$$

This shows that the bias between the WP estimator and the true PSD P is given by

$$b = \psi(\alpha+\beta+2) - \psi(\alpha+1). \tag{A.9}$$

---

[2] $\frac{\partial \mathrm{B}(\alpha,\beta)}{\partial \alpha} = \mathrm{B}(\alpha,\beta)\left[\psi(\alpha) - \psi(\alpha+\beta)\right]$

Using the fact that ψ can be expressed as

$$\psi(n) = -\gamma + \sum_{k=1}^{n-1} \frac{1}{k}, \quad \text{for} \quad n \geq 2 \tag{A.10}$$

where γ is the Euler-Mascheroni constant [1], the bias takes the form of a truncated harmonic series:

$$b = \sum_{k=\alpha+1}^{\alpha+\beta+1} \frac{1}{k}, \quad \text{for} \quad \alpha, \beta \in \mathbb{N}. \tag{A.11}$$

To express the bias by means of K and q, it is helpful to interpret α and β as the number of samples with values greater and smaller than the desired percentile $\hat{P}_{(i)}$. Therfore, we have to distinguish between two cases: (1) the sample percentile $\hat{Q}(q)$ matches exactly with one of the periodograms $\hat{P}_{(i)}$ (e.g., if $q = 0.5$ and K is odd), or (2) the sample percentile falls in between two periodograms $\hat{P}_{(i-1)}$ and $\hat{P}_{(i)}$ (e.g., if $q = 0.5$ and K is even). In the former case, α and β can be expressed by $\alpha = (K-1)(1-q)$ and $\beta = (K-1)q$, respectively. For the latter case, $\alpha = K(1-q)$ and $\beta = Kq$ are natural choices. Using this parameterization, Equation (A.11) can be rewritten as

$$b = \begin{cases} \sum\limits_{k=(K-1)(1-q)+1}^{K} \frac{1}{k}, & \hat{Q}(q) = \hat{P}_{(i)} \\ \\ \sum\limits_{k=K(1-q)+1}^{K+1} \frac{1}{k}, & \hat{P}_{(i-1)} < \hat{Q}(q) < \hat{P}_{(i)} \end{cases} \tag{A.12}$$

In the limit, that is, for $K \longrightarrow \infty$ both cases converge to $-\ln(1-q)$. Furthermore, the products $(K-1)(1-q)$ and $K(1-q)$ have to be integers, or, otherwise, rounded to the next nearest integer to compute the bias. If the constellation of K and q does not result in an integer value, the polynomial approximation for the digamma function [1]

$$\psi(n) \approx \ln(n) - \frac{1}{2n} - \frac{1}{12n^2} + \frac{1}{120n^4} - \frac{1}{252n^6} \tag{A.13}$$

can be used to to avoid rounding. In this case, the bias should be computed by

$$b = \psi(K+2) - \psi(K(1-q)+1). \tag{A.14}$$

A.3 Variance

In analogy to Equation (A.5), the second order moment of the sample quantile is given by

$$\mathbb{E}\{\hat{Q}^2_{(q)}\} = \frac{P^2}{\mathrm{B}(\alpha+1,\beta+1)} \int_0^1 t^\alpha (1-t)^\beta \left[\ln(t)\right]^2 \mathrm{d}t. \tag{A.15}$$

By using the relation

$$\frac{\partial^2 t^\alpha (1-t)^\beta}{\partial \alpha^2} = t^\alpha (1-t)^\beta \left[\ln(t)\right]^2 \tag{A.16}$$

and taking the second derivative of the beta function with respect to α, the second order moment yields

$$\mathbb{E}\{\hat{Q}^2_{(q)}\} \quad = \quad P^2 \left(\left[\psi(\alpha+1) - \psi(\alpha+\beta+2)\right]^2 + \left[\psi_1(\alpha+1) - \psi_1(\alpha+\beta+2)\right] \right). \tag{A.17}$$

Therein, $\psi_1(n)$ is the derivative of the digamma function – also referred to as trigamma function – and can be approximated by means of Equation (A.13) as

$$\psi_1(n) = \frac{\mathrm{d}\psi(n)}{\mathrm{d}n} \approx \frac{1}{n} + \frac{1}{2n^2} + \frac{1}{6n^3} - \frac{1}{30n^5} + \frac{1}{42n^7}. \tag{A.18}$$

From the first and second order moments of the sample quantile, the variance of the WP estimator can be determined:

$$\mathrm{var}\{\hat{P}^{(\mathrm{WP})}_q\} = \frac{P^2}{b^2} \left[\psi_1(\alpha+1) - \psi_1(\alpha+\beta+2)\right]. \tag{A.19}$$

For the general case, i.e., if $\hat{P}_{(i)} \neq \hat{Q}(p)$, the WP estimator's variance can be computed by

$$\mathrm{var}\{\hat{P}^{(\mathrm{WP})}_q\} = \frac{P^2}{b^2} \left[\psi_1(K(1-q)+1) - \psi_1(K+2)\right]. \tag{A.20}$$

A.4 Limiting Distribution

For $K \to \infty$, the order statistic of the modified periodograms is normally distributed around $-P\ln(1-q)$ with variance

$$\mathrm{var}\{\hat{Q}(q)\} = \left(\frac{P}{2}\right)^2 \cdot \frac{q(1-q)}{Kf^2(-2\ln(1-q))}, \tag{A.21}$$

where f is the PDF given in Equation (A.2) [26]. Simplifying this expression and taking the bias correction into account, the limiting variance of the WP estimator can be computed by

$$\mathrm{var}\{P_q^{(\mathrm{WP})}\} = \left(\frac{P}{b}\right)^2 \cdot \frac{q}{K(1-q)}, \tag{A.22}$$

Appendix B

MODEL COEFFICIENTS OF HIGH FREQUENCY NON-LINEAR REGRESSION FOR NOISE DURING RAIN

Table B.1 shows the coefficients of the high frequency (10 - 25 kHz) non-linear regression according to Equation (6.4) for noise during various rain rates and wind speeds.

Table B.1: Coefficients of high frequency non-linear regression according to Equation (6.4). A, $f_{c,h}$, $f_{c,l}$, s_h, and s_l are the amplitude, high cutoff frequency, low cutoff frequency, high frequency slope, and low frequency slope, respectively.

		Rain rate (mm/h)					
	Wind speed (m/s)	<2	2-5	5-10	10-20	20-30	30-50
		Deep location					
A	0 - 2	56.62	58.71	58.91	59.16	59.78	-
	2 - 4	51.83	54.23	55.22	56.82	-	-
	4 - 6	51.15	52.38	53.70	55.31	58.62	58.06
	6 - 8	52.28	53.68	55.31	58.77	63.33	61.68
	8 - 10	55.19	56.78	57.73	62.12	-	71.40
	10 - 12	57.47	58.28	60.32	64.21	67.10	74.68
	12 - 14	69.50	60.81	61.57	64.07	-	-
	>14	59.97	60.89	61.90	62.40	69.63	-
$f_{c,l}$	0 - 2	7.57	7.30	7.08	4.35	6.72	-
	2 - 4	6.33	6.42	6.11	5.23	-	-
	4 - 6	3.46	3.39	1.26	3.04	0	5.55
	6 - 8	0	0	0	0	0	0

	8 - 10	0	0	0	0	-	0
	10 - 12	2.88	1.56	2.93	0.87	0	0.68
	12 - 14	1.56	1.80	1.56	0.80	-	-
	>14	0.85	0.97	2.15	1.09	2.96	-
s_{l}	0 - 2	4.84	4.54	4.54	2.84	4.64	-
	2 - 4	4.17	4.03	4.06	3.60	-	-
	4 - 6	2.42	2.35	1.41	2.26	0.35	3.19
	6 - 8	0.14	0.14	0.14	0.15	0.16	0.15
	8 - 10	0.15	0.15	0.14	0.16	-	0.19
	10 - 12	24.31	14.69	23.96	18.46	0.16	26.24
	12 - 14	14.16	14.46	18.06	25.12	-	-
	>14	19.31	18.81	18.13	18.34	25.67	-
$f_{\mathrm{c,h}}$	0 - 2	33.28	33.18	33.32	33.56	36.83	-
	2 - 4	32.09	31.67	32.32	33.37	-	-
	4 - 6	30.90	30.72	30.71	31.45	30.59	30.77
	6 - 8	34.20	33.13	32.89	33.33	36.05	33.34
	8 - 10	44.05	43.16	41.25	40.89	-	37.88
	10 - 12	45.62	45.79	42.96	39.30	37.91	35.44
	12 - 14	36.24	35.18	34.67	38.03	-	-
	>14	30.34	29.94	29.86	28.95	27.24	-
s_{h}	0 - 2	5.73	5.92	6.21	6.62	5.96	-
	2 - 4	7.86	8.17	7.90	7.42	-	-
	4 - 6	9.62	9.92	10.42	9.68	10.57	9.79
	6 - 8	6.54	7.40	7.63	7.09	4.91	6.66
	8 - 10	3.07	3.18	3.50	3.05	-	3.01
	10 - 12	2.01	2.04	2.16	2.32	3.24	2.46

	12 - 14	2.22	2.26	2.31	2.24	-	-
	>14	2.27	2.32	2.35	2.39	2.73	-
		Shallow location					
A	0 - 2	61.51	62.62	64.08	66.40	-	79.85
	2 - 4	57.37	59.12	61.30	64.64	70.39	73.84
	4 - 6	56.14	57.36	59.41	64.62	68.17	71.85
	6 - 8	56.43	56.95	59.37	64.56	68.43	69.67
	8 - 10	58.64	59.59	61.39	63.97	73.41	72.53
	10 - 12	60.13	60.52	62.70	65.42	73.26	72.28
	12 - 14	60.94	61.78	63.81	66.10	70.08	69.63
	>14	63.68	64.09	66.33	67.57	67.21	-
$f_{\mathrm{c,l}}$	0 - 2	7.72	7.62	7.41	6.52	-	0
	2 - 4	6.93	6.92	6.56	6.35	3.89	0
	4 - 6	4.46	4.41	3.99	0.49	0	0.32
	6 - 8	0	0	0	0	0	0
	8 - 10	0	0	0	0	0.95	0.75
	10 - 12	1.43	0.79	1.76	0.21	3.09	0.55
	12 - 14	0	0.34	1.13	0.50	3.64	2.72
	>14	0.14	1.49	1.67	1.16	3.18	-
s_{l}	0 - 2	5.67	5.53	5.33	4.67	-	0.20
	2 - 4	5.18	5.24	5.10	5.05	3.24	0.20
	4 - 6	3.56	3.45	3.44	1.38	0.39	0.20
	6 - 8	0.17	0.18	0.18	0.19	0.21	0.22
	8 - 10	0.24	0.21	0.20	0.22	26.24	24.84
	10 - 12	26.75	24.47	28.73	28.48	23.13	27.23
	12 - 14	30	24.72	24.94	25.29	28.04	27.53
	>14	26.55	15.21	18.85	27.15	25.65	-

$f_{c,h}$	0 - 2	37.59	37.20	36.46	37.63	-	48.75
	2 - 4	34.71	34.14	33.91	33.06	37.77	44.21
	4 - 6	32.42	32.01	32.64	38.22	38.77	51.05
	6 - 8	40.93	34.69	36.21	44.92	44.15	44.53
	8 - 10	80.01	68.02	55.55	50.78	43.98	40.76
	10 - 12	60.76	58.54	51.77	48.13	37.16	40.69
	12 - 14	41.12	38.98	37.80	36.58	30.67	31.62
	>14	33.11	33.62	32.89	33.02	34.71	-
s_h	0 - 2	5.53	5.82	6.54	6.49	-	3.64
	2 - 4	8.04	8.73	9.02	10.07	6.43	4.43
	4 - 6	11	11.73	10.69	6.48	6.18	3.44
	6 - 8	5.85	8.98	7.62	4.24	3.92	3.49
	8 - 10	1.91	2.30	2.76	2.84	2.56	2.84
	10 - 12	1.91	2.04	2.20	2.40	2.66	2.57
	12 - 14	2.29	2.44	2.52	2.63	3.04	2.99
	>14	2.28	2.34	2.44	2.64	2.84	-